

**University of Miami  
Scholarly Repository**

---

Open Access Dissertations

Electronic Theses and Dissertations

---

2015-04-24

# On the Processes Controlling Antarctic Dense Shelf Water Outflows

Gustavo M. Marques  
*University of Miami*, [mastrorocco@gmail.com](mailto:mastrorocco@gmail.com)

Follow this and additional works at: [http://scholarlyrepository.miami.edu/oa\\_dissertations](http://scholarlyrepository.miami.edu/oa_dissertations)

---

## Recommended Citation

Marques, Gustavo M., "On the Processes Controlling Antarctic Dense Shelf Water Outflows" (2015). *Open Access Dissertations*. Paper 1399.

This Embargoed is brought to you for free and open access by the Electronic Theses and Dissertations at Scholarly Repository. It has been accepted for inclusion in Open Access Dissertations by an authorized administrator of Scholarly Repository. For more information, please contact [repository.library@miami.edu](mailto:repository.library@miami.edu).

UNIVERSITY OF MIAMI

ON THE PROCESSES CONTROLLING ANTARCTIC DENSE SHELF WATER  
OUTFLOWS

By

Gustavo Mastrorocco Marques

A DISSERTATION

Submitted to the Faculty  
of the University of Miami  
in partial fulfillment of the requirements for  
the degree of Doctor of Philosophy

Coral Gables, Florida  
May 2015

©2015  
Gustavo Mastrorocco Marques  
All Rights Reserved

UNIVERSITY OF MIAMI

A dissertation submitted in partial fulfillment of  
the requirements for the degree of  
Doctor of Philosophy

ON THE PROCESSES CONTROLLING ANTARCTIC DENSE SHELF WATER  
OUTFLOWS

Gustavo Mastrorocco Marques

Approved:

---

Tamay M. Özgökmen, Ph.D.  
Professor of Meteorology and Physical  
Oceanography

---

William Johns, Ph.D.  
Professor of Meteorology and Physical  
Oceanography

---

Igor Kamenkovich, Ph.D.  
Professor of Meteorology and Physical  
Oceanography

---

M. Brian Blake, Ph.D.  
Dean of the Graduate School

---

Laurie Padman, Ph.D.  
Senior Scientist  
Earth & Space Research  
Corvallis, Oregon

MARQUES, GUSTAVO MASTROROCCHI      (Ph.D., Meteorology and Physical  
Oceanography)

On the Processes Controlling Antarctic  
Dense Shelf Water Outflows      (May 2015)

Abstract of a dissertation at the University of Miami.

Dissertation supervised by Professor Tamay M. Özgökmen  
No. of pages in text. (137)

Formation of intermediate and abyssal water masses as dense water flows off continental shelves contributes to the lower limb of the meridional overturning circulation. The main goal of this dissertation is to advance the understanding of processes that determine volume flux and physical properties of oceanic outflows, focusing on outflows of dense shelf water (DSW) in Antarctica.

First, the effects of grid resolution, numerical schemes, Reynolds numbers and turbulence models on mixing and stirring driven by buoyancy-driven flows are quantified. Using the lock-exchange problem, we found that mixing in an ocean general circulation model is more sensitive to the choice of grid resolution than to the other parameters tested here; however, the results do not monotonically converge towards the optimum solution as resolution is refined. We then considered the stirring of a passive tracer field by submesoscale eddies generated by surface density fronts. We found that using a second-order turbulence closure provides an accurate representation of restratification in the mixed layer.

Second, idealized and realistic numerical simulations are used to investigate the excitation of topographic vorticity waves (TVWs) along the Antarctic continental slope by outflows of DSW through troughs. The modeled TVWs are sufficiently energetic to play an important role in cross-slope water mass exchanges and Antarctic Bottom Water (AABW) production. Idealized simulations show that wave frequency

depends on the amount of stretching in the ambient fluid over the outflow and on the background along-slope mean flow. Frequency is higher for steeper bottom slope, larger outflow density anomaly, and stronger westward mean flow. For weak stratification and weak westward along-slope flows typical of the Antarctic slope, wave energy propagates eastward, in the opposite direction from phase velocity. In a realistic simulation of the Ross Sea, TVW properties are modulated on seasonal and shorter time scales as background ocean state varies, consistent with our idealized results. Our results are also consistent with observations of TVWs in the southern Weddell Sea.

Lastly, high resolution numerical simulations are used to study the generation of a double plume pattern in oceanic outflows. Double plumes, previously observed in a laboratory study, carry water properties from the shelf into the deep ocean at two distinct depths. Our numerical model is configured to solve the nonhydrostatic Boussinesq equations in a two-dimensional configuration without rotation. A set of nine experiments were conducted by varying the ambient stratification frequency ( $N$ ) and the bottom slope ( $\alpha$ ). We present the first evidence that the double plume pattern may occur in oceanic environments, such as the Antarctic outflows. The parameters needed to identify the flow regimes are  $\alpha$  and the buoyancy number  $B = QN^3/g\ell^2$ , where  $Q$  is the volume flux of the dense water flow per unit width and  $g\ell$  is the reduced gravity. The double plume regime occurred when  $B \sim 0.02$ , regardless of the bottom slopes tested here. When  $B$  was about one order of magnitude smaller ( $\sim 0.002$ ), a single plume was always observed. For intermediate  $B$  values ( $B \sim 0.007$ ), a double plume regime occurred for steeper slopes ( $\alpha=0.1$  and  $\alpha=0.05$ ) and a single plume occurred for the shallower slope ( $\alpha=0.01$ ). An important characteristic of the double plume regime is the flow transition from a supercritical condition, where the Froude number ( $Fr$ ) is greater than one, to a slower and more uniform subcritical condition

( $Fr < 1$ ). This transition was associated with an internal hydraulic jump and consequent mixing enhancement. We hypothesize that double plumes around Antarctica could simultaneously transport DSW offshore as AABW and as intermediate-depth water masses that cool the Circumpolar Deep Water that is the primary heat source to the Antarctic continental margins.

To my parents, Lucia and Francisco, my sisters, Carla and Isabela and  
my girlfriend, Blakely, with love.

## Acknowledgments

The funding for this research was provided by the National Science Foundation.

First, I would like to thank my advisor, Tamay M. Özgökmen, for all the guidance, encouragement and support throughout the development of this dissertation. I also would like to express my gratitude to my committee, Laurie Padman, Bill Johns and Igor Kamenkovich for their assistance and help at all levels of my Ph.D. In particular, I want to thank Laurie for being a wonderful science mentor. During the development of this dissertation, Laurie and I had multiples conference calls and exchanged hundreds of emails. I truly appreciate and value everything I learned from him!

I want to thank my fellow labmates: Jean, Peng, Angelique, Ed, Guillaume and Sharon. I have learned immensely during our Friday meetings. I am particularly thankful to Jean for our philosophical debates, fun adventures and exchanges of knowledge, skills and frustrations. I also thank my good friends Matt Archer and Frank “Chico” Smith for giving me feedback on some parts of the dissertation.

Thanks to my colleagues from RSMAS for all the fun during my time in Miami: Kieran, Honghai, Teddy, Milan, Jian, Elizabeth, Claire, Dian, Cedric, Matthieu, Rolo, Conor, Stephane, Cris Cris, Maerlene, Tara, Kim.

A special thanks to the “Brazilian Mafia”: Ricardo, Luana, Marlos, Lisa, Chloe, Maguilinha, Tomas, Rafael, Fernando, Lucas, Vini, Mari, Ana Carolina, Fabricio and Tales. Voces foram como uma familia, muito obrigado por tudo!

Last but not least I would like to thank my parents, Lucia and Francisco, my sisters, Carla and Isabela, and my girlfriend, Blakely, for their encouragement, love and support.

# Contents

<b>List of Figures</b>	<b>ix</b>
<b>List of Tables</b>	<b>xvii</b>
<b>1 Introduction</b>	<b>1</b>
1.1 Review of main oceanic outflows . . . . .	2
1.2 Antarctic outflows and AABW formation . . . . .	5
1.3 Small scale processes in Antarctic outflows . . . . .	7
1.4 Research goals . . . . .	9
1.5 Outline . . . . .	11
<b>2 On modeling turbulent exchange in buoyancy-driven fronts</b>	<b>12</b>
2.1 Background . . . . .	12
2.2 The numerical models . . . . .	17
2.2.1 LES model - Nek5000 . . . . .	17
2.2.2 OGCM - ROMS . . . . .	19
2.3 Lock exchange problem for stratified mixing . . . . .	21
2.3.1 Model configurations and parameters . . . . .	21
2.3.2 List of experiments and quantification of mixing . . . . .	23
2.3.3 Description of the flow . . . . .	30
2.3.4 Comparison of mixing from LES and ROMS . . . . .	32

2.4	Upper ocean frontal instability for lateral stirring . . . . .	40
2.4.1	Model configuration and parameters . . . . .	40
2.4.2	Experimental description and tracer metrics . . . . .	43
2.4.3	Description of the flow . . . . .	47
2.4.4	Comparison of lateral stirring from LES and ROMS . . . . .	50
2.4.5	Restratification and vertical diffusivity . . . . .	54
2.5	Summary and conclusions . . . . .	56
<b>3</b>	<b>Topographic vorticity waves forced by Antarctic dense shelf water outflows</b>	<b>62</b>
3.1	Numerical simulations . . . . .	63
3.1.1	Idealized model of TVW generation by outflows . . . . .	63
3.1.2	Realistic model of the Ross Sea . . . . .	72
3.2	Results . . . . .	72
3.2.1	Idealized simulations . . . . .	72
3.2.2	Realistic model of Ross Sea outflows . . . . .	77
3.3	Summary . . . . .	78
<b>4</b>	<b>Double plume formation in numerical simulations of oceanic outflows</b>	<b>81</b>
4.1	Background . . . . .	81
4.2	Numerical setup . . . . .	85
4.3	Results . . . . .	92
4.3.1	Flow description . . . . .	92
4.3.2	Dense water thickness, Froude number and energy dissipation	95
4.3.3	Water mass formation . . . . .	97
4.3.4	Slope angle . . . . .	102

4.4	Flow regimes and application to oceanic outflows . . . . .	103
4.5	Summary . . . . .	109
<b>5</b>	<b>Conclusions</b>	<b>112</b>
	<b>References</b>	<b>122</b>

# List of Figures

2.1	Time evolutions of the normalized background potential energy $BPE^*$ from ROMS experiments with 10 m resolution and different explicit horizontal Reynolds number ( $Re_H$ ) values. . . . .	25
2.2	Contours of the normalized density perturbation $\rho'/\Delta\rho'$ values for the (left panels) Nek5000 simulation LES ( $Re=10^4$ ) and (right panels) ROMS experiment le-1.25-k $\varepsilon$ -10 $^4$ (see Table 4.1) during two non-dimensional times $t^* = 4.1$ (a and b) and $t^* = 47.6$ (c and d). The contours values are 0.1 (blue) and 0.9 (yellow). . . . .	31
2.3	Time evolutions of the normalized background potential energy $BPE^*$ from experiments with $\Delta x=10, 5, 2.5$ and $1.25$ m and $Re_H=10^3$ . The curve from the reference LES ( $Re=10^3$ ) experiment is also shown for comparison. Note the overlap between curves from experiments le-1.25-k $\varepsilon$ -10 $^3$ and le-1.25-ctrl-10 $^3$ ; and le-1.25-kpp-10 $^3$ and le-1.25-novmix-10 $^3$ . The lower panel on the right shows an expanded plot of the initial evolution of $BPE^*$ . . . . .	32

2.4	Time evolutions of the normalized background potential energy $BPE^*$ from experiments with $\Delta x=1.25$ m and $Re_H=10^3$ and $10^4$ . The curves from the reference LES ( $Re=10^3$ ) and LES ( $Re=10^4$ ) experiments are also shown for comparison. Note the overlap between curves from experiments le-1.25-k $\varepsilon$ -10 $^3$ and le-1.25-ctrl-10 $^3$ ; and le-1.25-k $\varepsilon$ -10 $^4$ , le-1.25-kpp-10 $^4$ and le-1.25-ctrl-10 $^4$ . . . . .	33
2.5	Probability density function (pdf, in %) of temperature ( $^{\circ}$ C) at a) $t^*=0.7$ , b) $t^*=30.0$ , c) $t^*=45.0$ and d) $t^*=50.0$ for the different tracer advection schemes evaluated here, namely MPDATA and U3H/C4V (experiments le-2.5-k $\varepsilon$ -10 $^3$ and le-2.5-u3h-10 $^3$ , respectively). The initial temperature values are highlighted by the solid black lines. . . . .	36
2.6	$BPE^*$ normalized root-mean-square errors ( $\Gamma$ , defined by (2.13) see text for details) as a function of the inverse grid resolution ( $\Delta x^{-1}$ , m $^{-1}$ ) for all ROMS experiments presented in Table 4.1. Note the overlap between points from experiments le-1.25-k $\varepsilon$ -10 $^3$ and le-1.25-ctrl-10 $^3$ ; le-1.25-k $\varepsilon$ -10 $^4$ , le-1.25-kpp-10 $^4$ and le-1.25-ctrl-10 $^4$ ; and le-1.25-novmix-10 $^3$ and le-1.25-kpp-10 $^3$ . . . . .	38
2.7	Initial condition for the MLI density perturbation field $\rho'(\mathbf{x}, t = 0)$ (kg m $^{-3}$ ), (top) surface horizontal section and (bottom) vertical cross section. . . . .	41
2.8	Layer thickness ( $\Delta z$ , m) as a function of vertical level for a) $N_{\sigma}=16$ , b) $N_{\sigma}=32$ and c) $N_{\sigma}=64$ . The blue and red lines represent the surface and bottom layers, respectively. . . . .	43
2.9	Three-dimensional view for the initial tracer concentration field $C_0(\mathbf{x})$ . The color bar shows concentration in kg m $^{-3}$ . Tick marks are placed every 1 km in the horizontal and 100 m in the vertical directions. . .	46

2.10 Density perturbation field $\rho'$ ( $\text{kg m}^{-3}$ ) for experiment mli-res100-32A at a) $t=4$ days, b) $t=10$ days, c) $t=15$ days and d) $t=30$ days. The thick marks are placed every 1 km in the horizontal and 100 m in the vertical. . . . .	48
2.11 Tracer wave-number power spectral densities for experiments listed in Table 4.2 at (top) time = 18 days and (bottom) time = 21 days. The LES ( $\text{Fr}=0.1$ ) results by Özgökmen et al. (2009b) at corresponding times are also superimposed for comparison. Note the similarity between the spectra from experiments mli-100-32- $k\varepsilon$ , mli-100-16- $k\varepsilon$ and mli-100-64- $k\varepsilon$ ; and experiments mli-100-32-kpp and mli-100-32-novmix. Typical wave-number slopes are shown in the background. . .	49
2.12 Second moment of the tracer distribution as a function of time for the MLI experiments listed in Table 4.2. The curves from experiments mli-100-32-kpp and mli-100-32-novmix are very similar. The LES ( $\text{Fr}=0.1$ ) curve presented in Özgökmen et al. (2011) is also superimposed for comparison. . . . .	51
2.13 Normalized root-mean-square errors computed from the $y$ -direction horizontal diffusivities $\langle K_y \rangle / (\Gamma)$ , defined by Eq. 2.13; see text for details) as a function of the inverse grid resolution ( $\Delta x^{-1}$ , $\text{m}^{-1}$ ) for all MLI experiments presented in Table 4.2. Note the overlap between points from experiments mli-100-32- $k\varepsilon$ and mli-100-64- $k\varepsilon$ ; and mli-100-32-kpp and mli-100-32-novmix . . . . .	52
2.14 Time series of (a) near surface tracer second moment ( $\sigma_y^2$ , $\text{km}^2$ ) and (b) maximum horizontal velocity ( $\vec{u}$ , $\text{m s}^{-1}$ ) in the mixed layer. Results from experiments mli-100-32- $k\varepsilon$ , mli-100-32-kpp and mli-100-32-novmix are shown. . . . .	54

2.15 Eddy streamfunction ( $\psi_e$ , $m^2 s^{-1}$ ) at day 7 for experiments (a) mli-100-32-k $\varepsilon$ , (b) mli-100-32-kpp and (c) mli-100-32-novmix. White lines show buoyancy contours. . . . .	57
2.16 Snapshots of vertical diffusivities ( $K_{CV}$ , $m^2 s^{-1}$ ) at $\sim 40$ m depth after 7 days of simulations from runs using a) the second order turbulence closure k- $\varepsilon$ /CA (experiment mli-100-32-k $\varepsilon$ ) and b) the algebraic Richardson number based KPP (experiment mli-100-32-kpp). . . . .	58
3.1 a) 3D view of the domain for the idealized model. Green point shows the location where $\Gamma$ values are computed. Thick marks are placed every 100 km in the horizontal and 500 m in the vertical directions. b) Partial view of the idealized domain for the control experiment (Exp.#01, see Table 3.2) at model time $t=78$ days, showing wave-like velocity structures east of the trough. The phase and energy directions, and two contours of tracer concentration (0.5 and 0.05) are also shown.	64
3.2 Layer thickness ( $\Delta z$ , m) as a function of vertical level (from bottom to surface) taken from Exp.#01 along $x = 0$ km. Conditions at four different water depths are shown: 700 m (shelf break), 1000 m (mid-slope), 1500 m (lower slope) and 2000 m (deep ocean). . . . .	66
3.3 (top) Time series of layer thickness ( $D$ , m), density difference ( $\Delta\rho$ , kg m $^{-3}$ ) and (bottom) cross-slope depth-averaged velocity ( $V$ , m s $^{-1}$ ) at the northern end of the trough (green dot in Figure 1); $D$ and $\Delta\rho$ were used to compute the mean and spread of $\Gamma$ values in Exp. #01. The total water depth $H$ at this point is 700 m. Digitization of $D$ represents steps in the vertical s-coordinate grid. . . . .	70
3.4 Domain setup and along-slope velocity (m s $^{-1}$ ) used to compute the dispersion curve for Exp.#12. . . . .	71

3.5 Dispersion curves from the <i>Brink</i> [2006] code (solid lines) using $H_0 = 500$ m, $ f  = 13.87 \times 10^{-5}$ s $^{-1}$ ( $72^{\circ}$ S), for different ambient stratification ( $N^2$ , s $^{-2}$ ), slope ( $\alpha$ ) and westward along-slope flow ( $U_{max}$ ). Also shown are the frequency and wavenumber pairs calculated from time series of sea surface elevation extracted along the upper slope for selected model experiments. Color of each symbol matches color of the corresponding dispersion curve. . . . .	74
3.6 Wave period ( $T$ ) normalized by the domain-averaged inertial period ( $T_{inertial}$ ) as a function of the stretching parameter ( $\Gamma$ ) for all experiments listed in Table 3.2. The horizontal bars (red lines) are the 80% range of $\Gamma(t)$ values for model time $t=70\text{--}100$ days (see also Table 3.2). The curves from Lane-Serff and Baines (1998) are plotted for comparison (solid line is the mean and dashed lines show upper and lower limits). Also shown are representative values for the Filchner, Drygalski and Glomar Challenger overflow plumes (see Table 3.3). . .	75
3.7 Map of Ross Sea. Shaded areas are water depths shallower than 530 m; black contours show 750 and 1500 m isobaths. Red line shows 1000 m isobath. Open circles are every 200 km along the isobath. . . . .	77

3.8 (a) Hovmöller diagram for band-passed (0.3-1 cycle per day (cpd)) cross-slope, depth-averaged velocity as a function of time in days of 2004 (y-axis) and distance (x-axis) along the 1000-m isobath (red contour in Fig. 3.7), representing the upper continental slope in the Ross Sea, Antarctica. Black vertical lines indicate western edges of the Drygalski Trough (DT) and Glomar Challenger Trough (GCT); see Fig. 3.7 for locations. Red line is location of a point $\sim$ 100 km east of GCT; see red circle on 1000-m isobath in Fig. 3.7. Typical values of group velocity ( $c_g$ ) and phase velocity ( $c_p$ ) are indicated. (b) Band-passed (0.3-1 cpd) across-slope (gray) and low-passed (<0.3 cpd) along-slope (red) velocity components at the 1000-m isobath, at the point $\sim$ 100 km west of GCT. (c) Mean potential density averaged along a transect across the northern GCT, for all model coordinate depths below 300 m; see green line in Fig. 3.7 for location. Vertical line at $\sigma_\theta = 27.91$ is the approximate value below which TVWs are not found. . . . .	80
4.1 An example of a double plume regime observed in the laboratory on a slope of $30^\circ$ (from Baines, 2008). The fluid has been dyed with fluorescense and is illuminated by a thin laser beam that scans a central vertical section. . . . .	82
4.2 Schematic of the model domain. . . . .	86
4.3 The three different background density ( $\rho - 1000, \text{ kg m}^{-3}$ ) profiles used in the numerical experiments. . . . .	89

4.4 Snapshots of passive tracer distribution ( $\text{kg m}^{-3}$ , color) and density contours ( $\text{kg m}^{-3}$ , black lines plotted every $0.02 \text{ kg m}^{-3}$ ) for three different experiments: (top) EXP1, $N = 10^{-3} \text{ s}^{-1}$ ; (middle) EXP4, $N = 5 \times 10^{-4} \text{ s}^{-1}$ and (bottom) EXP7, $N = 7.5 \times 10^{-4} \text{ s}^{-1}$ . Each simulation is shown at three instants (left) $t = 4$ hours; (center) $t = 8$ hours and (right) $t = 12$ hours. The blue boxes in the left and middle panels denote the boundaries for the closeups shown on the plots. Note that only the nearshore portion of the computational domain is illustrated here. . . . .	91
4.5 Snapshots of passive tracer distribution ( $\text{kg m}^{-3}$ , color) and density contours ( $\text{kg m}^{-3}$ , black lines plotted every $0.02 \text{ kg m}^{-3}$ ) at the end of the simulation for three different experiments: a) EXP1 at $t = 150$ hours; b) EXP4 at $t = 110$ hours and c) EXP7 at $t = 36$ hours. . . . .	94
4.6 Time-averaged plume thickness, $h_0$ (top) and Froude number, $\langle Fr \rangle$ (bottom) as a function of cross-slope distance for experiments EXP1, EXP4 and EXP7. . . . .	96
4.7 Snapshots of turbulent kinetic energy dissipation $\log_{10}(\varepsilon)$ ( $\text{m}^2 \text{ s}^{-3}$ ) and density contours ( $\text{kg m}^{-3}$ , black lines plotted every $0.02 \text{ kg m}^{-3}$ ) for EXP1 taken at (a) $t=110$ hours; (b) $t=111$ hours; and c) $t=112$ hours. Note that just a subset of the total domain is shown. . . . .	98
4.8 Same as Fig. 4.7, but for EXP4 at (a) $t=87$ hours; (b) $t=88$ hours; and c) $t=89$ hours. . . . .	99
4.9 Same as Fig. 4.7, but for EXP7 at (a) $t=34$ hours; (b) $t=35$ hours; and c) $t=36$ hours. . . . .	100

4.10 Time-averaged histograms of total tracer distribution (in %) as a function of downstream distance from the shelf and density anomaly $\delta\rho$ . The averages were taken over the last 25 hours of simulation and $\delta\rho$ was computed with respect to the initial density field. (a) EXP1, $N = 10^{-3} \text{ s}^{-1}$ ; (b) EXP4, $N = 5 \times 10^{-4} \text{ s}^{-1}$ and (c) EXP7, $N = 7.5 \times 10^{-4} \text{ s}^{-1}$ . . . . . .	101
4.11 Similar to Fig. 4.5, but for experiments where the shelf slope is $s = 0.05$ . (a) EXP2 at $t = 180$ hours; (b) EXP5 at $t = 180$ hours and (c) EXP8 at $t = 50$ hours. . . . .	105
4.12 Similar to Fig. 4.5, but for experiments where the shelf slope is $\alpha = 0.01$ . (a) EXP3 at $t = 268$ hours; (b) EXP6 at $t = 115$ hours and (c) EXP9 at $t = 100$ hours . . . . .	106
4.13 Buoyancy number $B$ versus shelf slope $\alpha = \tan(\theta)$ for all numerical experiments conducted here. Experiments that generated a double plume pattern are shown by the red squares while experiments that result in a single plume are shown by the blue squares (see Table 4.2 for the parameter values). Also shown are the values for various oceanic outflows inferred from available observations (circles, see Table 4.2 for additional information) and the results from the numerical simulations of Özgökmen et al. (2006) (black stars). The red stars show the values for the laboratory experiments discussed by Baines (2008) that resulted in double plume. . . . .	108
4.14 Schematic depiction of the processes occurring in the double plume regime. . . . .	110

# List of Tables

2.1	List of LE experiments conducted with ROMS. The number of grid points in the $x$ , $y$ and $z$ directions are: $20 \times 10 \times 10 = 2,000$ for $\Delta x=\Delta y=\Delta z=10$ m, $40 \times 20 \times 20 = 16,000$ for $\Delta x=\Delta y=\Delta z=5$ m, $80 \times 40 \times 40 = 128,000$ for $\Delta x=\Delta y=\Delta z=2.5$ m, and $160 \times 80 \times 80 = 1,024,000$ for $\Delta x=\Delta y=\Delta z=1.25$ m. CA = Canuto-A stability function, and $K_{MV}$ ( $K_{MV}^0$ ) and $K_{CV}$ ( $K_{CV}^0$ ) are the vertical (background) viscosity and diffusivity, respectively. The symbol * indicates that a combination of third-order upstream-biased horizontal scheme and fourth-order centered vertical scheme is used. . . . .	24
2.2	Wall clock time and the number of nodes used in the LE and MLI experiments. . . . .	29
2.3	List of MLI experiments conducted, where $N_\sigma$ is the number of sigma levels, $\Delta x=\Delta y$ is the horizontal grid spacing and CA = Canuto-A stability function. The minimum and maximum vertical grid spacing ( $\Delta z$ ) values are also shown. . . . .	45
3.1	Vertical s-coordinate parameters and diagnostics (maximum rx0 and rx1) for the different experiments conducted in this study. . . . .	65

3.2	List of numerical experiments conducted. Values of $c_p < 0$ and $c_g < 0$ indicate westward along-slope phase and energy propagation, respectively. . . . .	68
3.3	Estimated stretching parameter $\Gamma$ and shelf waves oscillation period $T$ for the following overflow plumes: Filchner (Foldvik et al., 2004; Wang et al., 2009; Jensen et al., 2013), Drygalski (Padman et al., 2009; Muench et al., 2009a) and Glomar Challenger (Section 3.2.2). . . . .	76
4.1	Summary of numerical experiments conducted. . . . .	90
4.2	Parameter values for the numerical experiments and for various oceanic outflows as described in Section 4.4. The values for oceanic outflows were taken from the field campaigns described in the following publications: Ross Sea: Gordon et al. (2004); Muench et al. (2009a); Mediterranean Sea: Price et al. (1993); Baringer and Price (1997); Red Sea: Peters et al. (2005); Matt and Johns (2007); Weddell Sea: Foldvik et al. (2004); Denmark Straits: Girton and Sanford (2003). . . . .	104

# Chapter 1

## Introduction

Antarctic Bottom Water (AABW) is the largest component, by volume, of bottom water in the world ocean, and plays a critical role in the meridional overturning circulation (MOC) as well as in transporting heat and carbon dioxide ( $\text{CO}_2$ ) (Schmitz, 1995; Broecker et al., 1998; Lumpkin and Speer, 2007; Johnson, 2008). AABW is formed along the Antarctic continental slope, where most of the cold and salty Dense Shelf Water (DSW) outflows towards the abyssal ocean through troughs. There is observational evidence that, over the past three decades, AABW has been warming, freshening and declining in volume (Johnson and Doney, 2006; Johnson et al., 2007; Purkey and Johnson, 2010; de Lavergne et al., 2014). Such changes imply a reduction in the amount of  $\text{CO}_2$  captured by this water mass and, therefore, might accelerate climate change.

The main goal of this dissertation is to gain insights into the physical mechanisms that influence the properties and volume flux of DSW and AABW outflows around Antarctica. Future observational and modeling efforts will benefit from the results of this dissertation. This introduction provides background on the main oceanic outflows around the world (1.1), then focuses on the Antarctic outflows (1.2) and the small-scale processes associated with them (1.3). The research questions are presented in

Section 1.4. Finally, Section 1.5 provides an outline of how Chapters 2-4 contribute to our understanding of the processes controlling Antarctic DSW outflows.

## 1.1 Review of main oceanic outflows

Oceanic outflows are density-driven currents that are generated either at high latitudes, where water density increases due to cooling and brine rejection of growing sea ice, or in subtropical marginal seas where water density increases due to evaporation. In the oceanographic literature this type of flow is also referred as overflow, but the term outflow is used throughout this dissertation. Oceanic outflows have been studied in some detail around the world (Price and Baringer, 1994; Legg et al., 2009), since they form most of the intermediate and deep water masses of the world ocean including AABW (Orsi, 1999) and, therefore, are likely to influence the MOC.

Numerical predictions of the Earth's future climate must rely on the accuracy of the MOC as represented in the ocean component of Global Climate Models (GCM). Heuzé et al. (2013) compared the results from 15 CMIP5 (Coupled Model Intercomparison Project Phase 5) climate models with an observed climatology, focusing on the southern ocean deep water properties, and found that none of the models analyzed reproduced the process of AABW formation accurately. Despite recent advances in numerical techniques and computing power, even the smallest horizontal grid size employed in the current generation of ocean general circulation models (OGCMs) and coupled GCMs ( $\sim 0.2^\circ$ ; Taylor et al., 2012) is not sufficient to explicitly represent important small processes occurring in oceanic outflows, such as those described in Section 1.3. Therefore, efforts should be put toward understanding the physics behind major oceanic outflows to a level where parameterizations can then be developed and incorporated into large scale models.

The relatively well observed outflows of dense water from the Nordic Seas through the Greenland-Scotland ridge are essential to deep water formation since they form the North Atlantic Deep Water (NADW) (Lee and Ellett, 1965; Orsi et al., 2001). The Greenland-Scotland ridge is a submarine mountain range separating the subpolar North Atlantic from the deep basins of the Nordic Seas, where dense water is formed. The dense flow has to cross this ridge before reaching the North Atlantic, where it forms NADW. The Nordic outflows can be divided into four branches based on relatively shallow ( $\leq 750$  m) topographic constraints: Denmark Strait (DS), Iceland-Faroe Ridge (IFR), Faroe-Bank Channel (FBC) and Wyville Thomson Ridge (WTR) (Hansen and Osterhus, 2000; Olsen et al., 2008). Nearly half of the dense water formed in the Nordic seas flows through the DS; one third flows through the FBC and the remainder is divided between flows over the IFR and the WTR (Hansen and Osterhus, 2000, 2007; Chang et al., 2009).

The DS and FBC outflows are very different in terms of their topography and outflow characteristics. In the wide ( $\sim 100$  km) and shallow ( $\sim 600$  m) DS, the dense water reaches geostrophic balance as it flows southward along the continental slope, while it gains volume by entrainment due to mesoscale eddies; this process forms the densest NADW component (Spall and Price, 1998; Macrander et al., 2007; Voet and Quadfasel, 2010). The outflow in the narrow ( $\sim 20$  km) and deep ( $\sim 800$  m) FBC is characterized by high mesoscale variability and energetic oscillations consistent with those from topographic Rossby waves (Darelius et al., 2011). The fate of the FBC outflow is not fully known, despite many observational studies, due to the complicated topography downstream of these regions (Saunders, 1996; Mauritzen et al., 2005; Sherwin and Turrell, 2005; Geyer et al., 2006). This uncertainty also applies to the IFR and WTR outflows.

In contrast to the North Atlantic outflows, the outflow of dense water from the Red Sea and the Mediterranean Seas do not lead to deep water formation. These outflows, therefore, are not as important to the MOC as are the outflows that lead to deep water formation. The Mediterranean source water, which is the densest outflow source water (Price and Baringer, 1994), is dense enough to sink to the bottom of the Atlantic Ocean; however, instead, it ends up forming an intermediate water mass. As the observations by Baringer and Price (1997) revealed, the Mediterranean outflow undergoes very strong entrainment, and rapid dilution, when it begins to descend the continental slope west of the Strait of Gibraltar. It then takes a geostrophically adjusted path over the continental slope until it flows through the Gulf of Cadiz, where further entrainment of fresh North Atlantic Central Water occurs. It finally equilibrates as an intermediate water mass after forming mesoscale eddies near Cape St. Vincent.

The Red Sea outflow also equilibrates as an intermediate water mass in the Indian Ocean (Bower et al., 2005; Peters et al., 2005). Before doing so, it enters the Gulf of Aden through the Bab el Mandab Strait where it entrains significantly less-dense near-surface water as it gets divided into two channels (Murray and Johns, 1997; Bower et al., 2005; Matt and Johns, 2007). It then interacts with a sequence of nearly barotropic mesoscale eddies originating in the Indian Ocean (Ilcak et al., 2011). The Red Sea outflow is strongly seasonal, with its transport being more pronounced during winter time (Bower et al., 2005; Peters et al., 2005; Matt and Johns, 2007).

Antarctic outflows, the primary interest of my dissertation, are not as well studied as the outflows discussed above, largely because of the difficulty of making measurements in Antarctic environments. Unlike in the previous outflows, the density-driven currents in Antarctica do not originate at narrow straits, but rather they begin in wide

areas of the continental shelf. A detailed review of Antarctic outflows and consequent AABW production is presented in the following Section.

## 1.2 Antarctic outflows and AABW formation

Formation of AABW is initiated on the continental shelves around Antarctica when DSW forms due to buoyancy loss from ocean surface cooling and brine rejection of growing sea ice. As this water flows down the continental slope, subsequent entrainment of ambient water results in the formation of many water types including those associated with AABW (Gill, 1973; Orsi, 1999; Gordon, 2001). The signature of Antarctic DSW is seen in both bottom water (including AABW) and intermediate-depth intrusions (e.g., Carmack and Killworth, 1978). The existence of these two modes is usually attributed to regional differences, seasonality, or strong short-term variability (e.g., differences between spring and neap tides). However, based on laboratory experiments reported by Baines (2005, 2008), the hypothesis that a single outflow could create a double outflow that simultaneously delivers water to both the deep benthic ocean and intermediate layers of the Southern Ocean should also be considered.

The conditions necessary for persistent formation of shelf water dense enough to drive bottom water formation exist in a few locations around Antarctica. Most AABW production takes place in the southwestern and western Weddell Sea (Foster and Carmack, 1976; Gordon et al., 1993; Foldvik et al., 2004; Darelius et al., 2009), along the Adélie Coast (Rintoul, 1998; Williams et al., 2010), and in the Ross Sea (Jacobs et al., 1970; Whitworth and Orsi, 2006; Gordon et al., 2009). Most of the offshore transport of DSW occurs through topographic features such as the Filchner Sill in the Weddell Sea (Foldvik et al., 2004; Darelius et al., 2009) and the Drygalski

and Glomar Challenger troughs in the Ross Sea (Orsi and Wiederwohl, 2009; Gordon et al., 2009; Budillon et al., 2011).

More recently, the formation of DSW in the Cape Darnley and Vincennes Bay polynyas, East Antarctica, has been revealed using data from moorings and instrumented elephant seals (Ohshima et al., 2013; Kitade et al., 2014). Other studies confirm that East Antarctica provides a significant source of dense water and plays an important role in ventilating the deep Southern Ocean (Wong and Riser, 2013). There is also observational evidence that AABW was formed by deep-water convection that occurred during the austral 1974-1976 winters, where a large open-water polynya was observed in the Weddell Sea (Gordon, 1982). This has been viewed as a rare event considering that deep-water convection in the Southern Ocean has not been observed since then. However, given the lack of observations, especially during winter time, it is possible that additional important AABW production sites and/or events have not yet been discovered.

It is very difficult to conduct observations near the Antarctic continent due to the frequent presence of sea-ice and icebergs, severe weather conditions and its remoteness from ports. In addition, Antarctic outflows are very energetic and measuring the water properties within these dense bottom currents represents a real challenge for oceanographers. For example, it is difficult to keep the instruments in fixed positions in the water column, while the time taken to conduct a traditional ship survey across an outflow results in aliasing of time variability into the spatial maps that are produced. Previous studies have shown that oceanic outflows can affect the upper-ocean circulation (Høyer and Quadfasel, 2001; Özgökmen et al., 2001; Kida et al., 2008). For example, changes in sea surface height associated with mesoscale eddies generated by the DS and FBC outflows have been inferred from satellite altimeters (Høyer and Quadfasel, 2001). Therefore, any evidence that Antarctic outflows may result

in upper-ocean responses that are relatively easier to observe would be extremely valuable to the detection and monitoring of Antarctic outflows.

Antarctic outflows are distinct from other outflows which either experience sufficient entrainment to form intermediate water masses (e.g., the Red Sea and Mediterranean outflows) or remain attached to topographic slopes over large distances (e.g., the Denmark Strait outflow). Instead, most Antarctic outflows quickly move downslope to the abyssal plains at the base of the continental slope. One characteristic of Antarctic environments that might explain this behavior is the relatively weak ambient stratification compared to other major outflow locations (Price and Baringer, 1994). Since ambient rotation is strong at high latitudes, the flow field is expected to be topographically controlled, with mean flows primarily oriented along  $f/H$  contours, where  $f$  is the Coriolis parameter and  $H$  is the total water depth. However, the observation that Antarctic outflows routinely deliver dense shelf water to the deep ocean suggests that this constraint must be somehow broken. In the following section I discuss some of the small-scale processes that can overcome this constraint.

### 1.3 Small scale processes in Antarctic outflows

Evidence from observations and numerical model studies in the NW Ross Sea (Bergamasco et al., 2003; Gordon et al., 2004, 2009; Muench et al., 2009b; Padman et al., 2009; Muench et al., 2009a; Visbeck and Thurnherr, 2009; Wang et al., 2010; Budillon et al., 2011) as well as in the southern Weddell Sea (Foldvik et al., 2004; Darelius et al., 2009; Wang et al., 2009; Wilchinsky and Feltham, 2009; Matsumura and Hasumi, 2010; Jensen et al., 2013) have pointed to the importance of processes with small temporal and spatial scales such as topographic features, time-dependency (tides) and waves in breaking the geostrophic constraint in these Antarctic regions.

Numerical simulations (Özgökmen and Fischer, 2008; Muench et al., 2009b; Ilicak et al., 2011), laboratory experiments (Wahlin et al., 2008) and analytical models (Wahlin, 2002, 2004) show that small-scale ( $L <$  first baroclinic radius of deformation  $R_d$ , which is  $\sim 5$  km for this region) features on the shelf slope can enhance the down-slope transport of dense water. Bathymetric features with typical trough-to-crest heights of 10-100 m and along-slope trough-to-trough wavelengths of order 1 km have been identified over the continental shelf and upper slope around the NW Ross Sea, Antarctica (Noormets et al., 2009).

As part of the Antarctic Slope (AnSlope) project, field and modeling studies conducted on the NW Ross Sea revealed the importance of tides in terms of mixing and cross-slope advection of water masses (Whitworth and Orsi, 2006; Muench et al., 2009a; Padman et al., 2009). This region has tidal currents that can exceed  $1 \text{ m s}^{-1}$  during spring tides over the outer shelf and upper slope (Whitworth and Orsi, 2006). Numerical simulations confirmed previous hypotheses that the tidal currents make a significant contribution to the formation of AABW in this region (Padman et al., 2009; Wang et al., 2010). Due to steep continental slopes near the Drygalski Trough ( $s = dh/dx \sim 0.1$ ), the large tidal advection length scale ( $\sim 20$  km) can quickly move DSW from a depth of 500 m to the abyssal ocean. The thermobaric effect (Gill, 1973) may be particularly critical in accelerating the downslope propagation of the dense water during this process.

For the southern Weddell Sea, numerical simulations (Wang et al., 2009) and observations (Darelius et al., 2009; Jensen et al., 2013) show barotropic, sub-inertial, quasi-periodic oscillations in water properties along the upper continental slope. Recently, Jensen et al. (2013) have shown that the properties of these oscillations are consistent with mode-1 coastal trapped waves. In this dissertation, I refer to these waves as topographic vorticity waves (TVWs) (Platzman et al., 1981), since they

depend on the large bathymetry gradient across the continental slope rather than distance from the coast. Jensen et al. (2013) hypothesized that the TVWs they observed in the southern Weddell Sea were generated by the release of DSW from the Filchner Trough. However, this hypothesis has not yet been confirmed. Periodicity in dense outflows has previously been observed in laboratory studies (e.g., Lane-Serff and Baines, 1998), providing an oscillatory forcing for TVWs that can subsequently propagate along the continental slope. If such waves can indeed be triggered by the outflow of dense water, this would be an important characteristic of Antarctic outflows that could potentially be used to discover new AABW formation sites and design new observational programs.

## 1.4 Research goals

The aim of this dissertation is to improve the understanding of the processes occurring in oceanic outflows, focusing on those around Antarctica that contribute to the global inventory of AABW. I am particularly interested in processes that act over time and length scales that are small compared with resolution in current OGCMs, and so require parameterization in models used to predict AABW production in future climate states. To do so, I will address a number specific science questions.

- What numerical parameters are important when modeling buoyancy driven flows, such as oceanic outflows, and how do they affect mixing and stirring?

Modeling oceanic outflows using Ocean General Circulation Models (OGCMs) is not a trivial task. To determine the tradeoff between computational speed and solution accuracy, the modeler needs to understand how grid resolutions, numerical schemes and turbulence models affect the results. Therefore, before modeling Antarctic outflows, I quantified how mixing and stirring in a OGCM was affected by common modeling

choices, namely the spatial resolution, tracer advection schemes, Reynolds number and turbulence closures. Although this study is not directly related to oceanic outflows, it provides useful guidance on the setup of the numerical experiments presented Chapters 3 and 4.

- Can Antarctic outflows trigger TVWs? If so, what are they main parameters controlling the properties of these waves and how do they affect their dispersion relation?

At the typical periods of the TVWs observed in the Weddell Sea, 1-2 days (Jensen et al., 2013), dispersion curves for weak stratification typical of Antarctic seas have two solutions, with potential for energy propagation in both directions from the source. Propagation of TVWs to the west of the source, i.e., in the same direction as the dense water outflow, will affect mixing of the outflow and the volume flux and hydrographic properties of the resulting AABW. Eastward propagation of TVWs will provide an energy source for mixing of water that is approaching the trough in the westward-flowing Antarctic Slope Current (ASC), and so modifies the properties of the water masses with which the DSW interacts as it exits the trough. Hence, these waves will affect the exchange of water mass properties between the deep Southern Ocean and Antarctica's shelf seas and should therefore be represented in climate models.

- Can a single outflow deliver water to both the deep benthic ocean and intermediate layers simultaneously? If so, under which parameter range might this occur?

Temperature and salinity sections taken off the Wilkes Land, Antarctica, show the presence of an interleaving layer, located above abyssal water masses, that seems to be associated with the outflow of DSW (Carmack and Killworth, 1978). A similar flow pattern, referred to as double outflow regime, has been observed in laboratory

experiments of dense water flowing down slopes and into stratified environments (see top panel of Fig 4.1 in Chapter 4; Baines, 2008). This type of flow is not fully understood, and it has not been modeled yet. I seek to investigate whether the double outflow regime can be generated in numerical simulations under realistic geophysical parameters and scales.

## 1.5 Outline

This dissertation is organized as follows. In Chapter 2, a series of numerical simulations for two idealized cases, namely the lock-exchange and the mixed-layer instability problems is presented. The main goal of this chapter is to compare the mixing and stirring derived from two modeling approaches: an OGCM (ROMS) that solves the hydrostatic primitive equations, and a spectral element model (Nek5000) that integrates the nonhydrostatic Boussinesq equations. In Chapter 3, idealized and realistic numerical simulations are used to show that Antarctic outflows can trigger TVWs; the dependence of the dispersion properties of these waves on bottom slope, outflow density anomaly, and background is also presented in this chapter. Chapter 4 explored the generation of a double outflow pattern in two-dimensional non-hydrostatic numerical simulations of oceanic outflows. Finally, the main conclusions of this dissertation are presented in Chapter 5.

# Chapter 2

## On modeling turbulent exchange in buoyancy-driven fronts

In this chapter, we quantify the uncertainty in the solution space associated with mixing and stirring in ocean general circulation models due to common modeling choices, namely the spatial resolution, tracer advection schemes, Reynolds number and turbulence closures. The outcomes from this study inform the model configurations presented in the following chapters.

### 2.1 Background

Ocean general circulation models (OGCMs) are the primary tools for predicting ocean currents and changes in the ocean’s stratification. Many OGCMs integrate the hydrostatic primitive equations (PE) set using a variety of horizontal and vertical coordinates, mixing parameterizations and advection schemes (e.g., Griffies et al., 2000; Griffies, 2004). OGCMs have experienced significant development over the past two decades (Chassignet et al., 2006; Capet et al., 2008; Martin et al., 2009; Fox-Kemper and Menemenlis, 2008; Lemarié et al., 2012). These models can be configured at the global and regional scale, or can have a nested structure to represent multi-scale interactions (Debreu et al., 2012). Modern OGCMs contain realistic forcing, domain

geometry, and assimilate ocean data available from a wide range of instruments, including (but not limited to) satellite altimeter, sea surface temperature, current meters, drifters and other *in situ* data for temperature and salinity.

The progress in OGCM development has been facilitated by the operational needs of the Navy as well as those of the basic research community (Shchepetkin and McWilliams, 1998; Hurlburt et al., 2009). Ocean observing and assimilation techniques have matured to a level where one can claim that the dynamics, phase and strength of the ocean's mesoscale features are adequately represented in OGCMs. For instance, Thoppil et al. (2011) show that the energetics of the mesoscale field observed by drifters and satellite can be reproduced by both data-assimilative and non-assimilative models using a horizontal resolution of  $1/12^\circ$ - $1/25^\circ$ . Operational OGCMs can also exhibit a good predictive skill for the turn over time scales of mesoscale eddies (Hurlburt et al., 2008).

Nevertheless, OGCMs may encounter significant obstacles for reproducing accurate results for scales smaller and faster than the mesoscale (scales smaller than  $O(10)$  km and shorter than a few days) due primarily to three reasons. First, data at such scales may not be available from observing systems, or contain technical challenges within the context of present assimilation methods. For instance, sea-surface height data is usually converted to velocity under the assumption of geostrophy, while submesoscale flows are distinctly ageostrophic (Mahadevan and Tandon, 2006; Thomas et al., 2008).

Second, OGCMs may not resolve submesoscale features fully and must rely on subgrid-scale (SGS) parameterizations (Fox-Kemper et al., 2008; Fox-Kemper and Ferrari, 2008). Recent numerical studies showed that the SGS parameterization can have important consequences in the temporal and spatial evolution of submesoscale instabilities even when the grid spacing resolves the submesoscale (Ramachandran

et al., 2013). OGCMs were originally designed to model large scales processes (i.e., on the order of the radius of deformation), where the flow is anisotropic with lateral processes being far more energetic than vertical processes. Therefore, these models sub-divide the SGS parameterizations for the transport of momentum and tracers to whether they occur in the horizontal or vertical directions. In both cases, the unresolved processes are represented through an eddy viscosity or diffusivity. The vertical SGS models commonly used in OGCMs were originally designed for situations where turbulent processes are not even partially resolved and, therefore, the model resolution does not appear explicitly. These models fall into two basic categories: algebraic models, like KPP (K-Profile Parameterization, Large et al. (1994)) and second order turbulence closures (Large, 1998; Canuto et al., 2001). While there have been criticisms of KPP for needing tuning of dimensional parameters for different flows (Chang et al., 2005), the KPP algorithm has appeal not only because of its simplicity, but also because it has been shown to work reasonably well in challenging flows involving fully 3D stratified mixing affected by the details of bottom topography (Chang et al., 2008) within the limitations of the observational data sets. Second order turbulence closures have a long history of development (Mellor and Yamada, 1982; Kantha and Clayson, 1994; Burchard and Baumert, 1995a; Burchard and Bolding, 2001; Canuto et al., 2001; Baumert and Peters, 2004; Baumert et al., 2005; Warner et al., 2005b; Umlauf and Burchard, 2005; Canuto et al., 2007), and they have also been shown to work reasonably well in complex problems involving shear-driven stratified mixing (e.g., the correct representation of mixing between overflows and ambient water masses; Ilicak et al., 2008). These models have a higher computational cost than algebraic models, since they require integration of two additional prognostic equations (typically turbulent kinetic energy and dissipation rate), as well as include significant assumptions on the form of these equations (Wilcox et al., 1998). Both classes of

SGS models are aimed to estimate a diffusivity coefficient, parameterizing only the downward energy cascade processes. Parameterizations that potentially address upward energy cascade, or dispersion (as opposed to dissipation) potentially exist (San et al., 2011; Berselli et al., 2011), but have not been extensively investigated yet.

Third, even if the OGCMs contain the spatial resolution to extend into the submesoscales and below, the PE start losing validity, being subject to the hydrostatic approximation (Kantha and Clayson, 2000). The hydrostatic approximation affects both dissipative and dispersive properties of fluid motion. Neither the overturning of density surfaces by Kelvin-Helmholtz (KH) instability, which is one of the primary mechanisms responsible for mixing in the ocean (McWilliams, 2008; Taylor and Ferrari, 2009), nor the correct dispersion relation for non-linear internal waves can be explicitly captured with hydrostatic models. Since the inclusion of a non-hydrostatic pressure solver in OGCMs requires a substantial change in these codes, recent efforts have focussed on the development of suitable solvers (Scotti and Mitran, 2008) and hybrid hydrostatic and non-hydrostatic models (Botelho et al., 2009; Duan et al., 2010; Campin et al., 2010). As both of these avenues will not only require significant code development, but also will generate substantially larger model output for post-analysis, there is still need for further investigations within the formalism of the existing OGCMs.

To conclude, there is a need for carefully evaluating the accuracy of the OGCMs (and their SGS models) below the mesoscale regime. The scales of interest include submesoscales, as well as fully 3D stratified mixing.

The submesoscale phenomena were first recognized by McWilliams (1985b) and received considerable attention in recent years, with the identification of mixed-layer instability (Boccaletti et al., 2007; Fox-Kemper et al., 2008) and the importance of submesoscale motions in biogeochemical transport in the ocean (Lévy et al., 2001;

Klein and Lapeyre, 2009; Calil and Richards, 2010). In addition, submesoscale motions are thought to form the bridge between long-lived quasi-geostrophic motions and rapidly-dissipating small scale turbulence (Müller et al., 2005; McWilliams, 2008; Capet et al., 2008). Stratified mixing is of interest in coastal phenomena (Warner et al., 2005a; MacCready et al., 2009), as well as during deep water formation (Legg et al., 2009). Therefore, it is critical that OGCMs represent stratified mixing accurately, or alternatively, the errors associated with their parametric representation are quantified.

In this chapter, we present a direct comparison of results from two types of problems that are challenging for OGCMs:

- (1) So-called lock-exchange (LE) problem, which is a simple computational setting to quantify the temporal evolution of mixing in a stratified fluid. This problem is discussed in some detail by Özgökmen et al. (2009a,b).
- (2) Mixed-layer instability (MLI) for submesoscale motions. MLI is very similar to the LE problem in terms of the computational setting, but differs dynamically due to the presence of ambient rotation and a high-aspect domain ratio. MLI was studied using LES by Özgökmen et al. (2011); Özgökmen and Fischer (2012); Özgökmen et al. (2012). The metric of interest here is the lateral stirring carried out by the submesoscale MLI eddies. This is of relevance to the lateral dispersion of pollutants and biogeochemical tracers in the ocean.

While computations for both problems are carried out in idealized settings, they have the advantage that LES (large eddy simulation, Sagaut (2000)) solutions are feasible and serve as ground truth. LES refers to numerical solutions of the non-hydrostatic equations in which the large eddies, carrying most of the Reynolds stresses, are resolved through computation, while the effect of the smaller eddies on the flow is represented by SGS models that depend explicitly on the resolution of the model.

The goal of these SGS models is to anticipate higher resolution results at any given resolution (hence simulations performed using LES will converge as resolution is increased). The LES approach lies in between the extremes of direct numerical simulation (DNS), where all turbulence is resolved, and Reynolds-averaged Navier-Stokes (RANS), in which only the mean flow is computed while the entire effect of turbulence is represented by SGS models (such as the second order turbulence closures). Since LES greatly reduces the SGS parameterization problem, many studies on ocean turbulence have relied on this approach to establish a ground truth for particular problems (Wang et al., 1998; Large, 1998; Chang et al., 2005; Xu et al., 2006). In addition, recent studies (Fox-Kemper and Menemenlis, 2008; Ramachandran et al., 2013) have shown that LES techniques can replace the traditional RANS methods and are a promising avenue for SGS parameterizations in high-resolution ocean models.

## 2.2 The numerical models

### 2.2.1 LES model - Nek5000

Our reference model is Nek5000, which integrates the Boussinesq equations (BE) based on the spectral element method, a high order finite element method for partial differential equations (Patera, 1984; Fischer, 1997). Nek5000 has been previously used for oceanic applications relevant to mixing and stirring, such as LES of LE problem (Özgökmen et al., 2007; Özgökmen et al., 2009a,b) as well LES of MLI (Özgökmen et al., 2011; Özgökmen and Fischer, 2012; Özgökmen et al., 2012). High-order spectral element methods have significantly better convergence characteristics than finite difference methods, leading to negligible numerical dissipation and errors (Patera, 1984; Fischer et al., 1988; Boyd, 2001).

Nek5000 is configured to integrate the non-dimensionalized Boussinesq equations:

$$\left\{ \begin{array}{l} \frac{D\bar{\mathbf{u}}}{Dt} = Ro_H^{-1} \hat{\mathbf{z}} \times \bar{\mathbf{u}} - \nabla \bar{p} - Fr^{-2} \bar{\rho}' \hat{\mathbf{z}} + Re^{-1} \nabla^2 \bar{\mathbf{u}} - \nabla \cdot \boldsymbol{\tau}, \\ \nabla \cdot \bar{\mathbf{u}} = 0, \\ \frac{D\bar{\rho}'}{Dt} = Pe^{-1} \nabla^2 \bar{\rho}', \\ \frac{D\bar{C}}{Dt} = Pe^{-1} \nabla^2 \bar{C}, \end{array} \right. \quad (2.1)$$

where the flow variables are the velocity vector  $\mathbf{u}$ , pressure  $p$ , density perturbation  $\rho'$  and passive tracer concentration  $C$ . The non-dimensional parameters are the Reynolds number  $Re = U_0 H_0 / \nu$ , the Froude number  $Fr = U_0 / (N H_0)$ , the vertical Rossby number  $Ro_H = U_0 / (f H_0) = a Ro$ , where  $Ro = U_0 / (f L)$  is the Rossby number,  $a = L/H_0$  the ratio of horizontal and vertical domain sizes and the Peclet number  $Pe = U_0 H_0 / \kappa$ . The latter can also be written as  $Pe = Re Pr$ , where  $Pr = \nu/\kappa$  is the Prandtl number.  $U_0$  is the flow speed scale,  $H_0$  the total fluid depth,  $\nu$  is the kinematic viscosity,  $\kappa$  is the molecular diffusivity,  $g$  is the gravitational acceleration,  $\rho_0$  is the fluid density,  $N$  is the buoyancy frequency,  $f$  is the Coriolis frequency and  $\hat{\mathbf{z}}$  is the unit vector in the vertical direction.

In (2.1),  $\frac{D}{Dt} := \frac{\partial}{\partial t} + \bar{\mathbf{u}} \cdot \nabla$  is the material derivative and overbars indicate resolved fields by constraining the spatial filtering to the computational mesh. In all Nek5000 simulations presented here, the subgrid scale tensor  $\boldsymbol{\tau} = \bar{\mathbf{u}}\bar{\mathbf{u}} - \bar{\mathbf{u}}\bar{\mathbf{u}}$  is computed using a dynamic Smagorinsky model. No explicit subgrid models are used for the density perturbation and tracer concentration fields, relying instead on de-aliasing and high-order filtering operations. For brevity here, the reader is referred to Özgökmen et al. (2009a,b) for further details on the dynamic Smagorinsky model.

### 2.2.2 OGCM - ROMS

The Regional Ocean Modeling System (ROMS<sup>1</sup>) is a three-dimensional, free-surface, hydrostatic, primitive equation ocean model formulated in a terrain-following vertical coordinate (Song and Haidvogel, 1994; Shchepetkin and McWilliams, 2005; Haidvogel et al., 2008). We emphasize that this is a widely used community model and, therefore, a fair choice to represent commonly used OGCMs. The horizontal discretization is by an orthogonal curvilinear Arakawa-C grid. In Cartesian coordinates, the horizontal momentum equations solved by ROMS in this particular study are:

$$\frac{\partial u}{\partial t} + \mathbf{u} \cdot \nabla u - fv = -\frac{1}{\rho_0} \frac{\partial \phi}{\partial x} + F_u + K_{MH} \nabla^2 u + \frac{\partial}{\partial z} (K_{MV} \frac{\partial u}{\partial z} + \nu \frac{\partial u}{\partial z}), \quad (2.2)$$

and

$$\frac{\partial v}{\partial t} + \mathbf{u} \cdot \nabla v + fu = -\frac{1}{\rho_0} \frac{\partial \phi}{\partial y} + F_v + K_{MH} \nabla^2 v + \frac{\partial}{\partial z} (K_{MV} \frac{\partial v}{\partial z} + \nu \frac{\partial v}{\partial z}), \quad (2.3)$$

while the vertical momentum equation is replaced by the hydrostatic approximation:

$$\frac{\partial \phi}{\partial z} = -\frac{\rho' g}{\rho_0}. \quad (2.4)$$

The continuity and scalar transport equations follow

$$\frac{\partial u}{\partial x} + \frac{\partial v}{\partial y} + \frac{\partial w}{\partial z} = 0 \quad (2.5)$$

and

$$\frac{\partial T}{\partial t} + \mathbf{u} \cdot \nabla T = F_T + K_{CH} \nabla^2 T + \frac{\partial}{\partial z} (K_{CV} \frac{\partial T}{\partial z} + \nu_\theta \frac{\partial T}{\partial z}). \quad (2.6)$$

---

<sup>1</sup><http://www.myroms.org/>

A linear equation of state is used to be consistent with (2.1)

$$\rho = \rho_0(1 - T_{coef}(T - T_0)). \quad (2.7)$$

In (2.2)-(2.7)  $F_u$ ,  $F_v$ ,  $F_C$  represent the forcing terms,  $\phi$  is the dynamic pressure,  $\nu$  and  $\nu_\theta$  are the background molecular viscosity and diffusivity, respectively,  $\rho_0=1025$  kg m<sup>-3</sup> is the background density,  $T_{coef}=2.06 \times 10^{-4} 1/^{\circ}C$  is the thermal expansion coefficient,  $T_0=5^{\circ}C$  is the background potential temperature,  $K_{MV}$  and  $K_{CV}$  are vertical eddy viscosity and diffusivity, while  $K_{MH}$ ,  $K_{CH}$  are horizontal eddy viscosity and diffusivity, respectively.

For both idealized cases studied here, the horizontal momentum is discretized with a third-order, upstream-biased advection scheme with velocity dependent hyper-viscosity (Shchepetkin and McWilliams, 1998). This scheme allows the generation of steep gradients in the solution, enhancing the effective resolution of the solution for a given grid size when the explicit viscosity is small. The implicit numerical diffusion, which acts as implicit viscosity, is such that the effective horizontal Reynolds number at that grid resolution takes the largest value possible while still ensuring adequate dissipation for stability. The latter is particularly useful in reducing spurious mixing (Ilicak et al., 2012). For the vertical momentum, a fourth-order centered differences scheme is used. Horizontal mixing of momentum and tracers is computed using a Laplacian formulation. Further details on the model configuration for each idealized application are described next.

## 2.3 Lock exchange problem for stratified mixing

### 2.3.1 Model configurations and parameters

For this problem we ignore the rotational terms in equations (2.1) to (2.3). Since both models integrate a different set of equations of motion, it is not a trivial matter to set them up in an identical fashion. We focus on some of the issues that require care in setting up these models. While Nek5000 configuration is based on the non-dimensional numbers  $a$ ,  $Fr$ ,  $Pr$  and  $Re$  (defined in Section 2.2.1), ROMS is configured in terms of dimensional variables. Another important difference between these models within the context of the present set of comparisons is that ROMS splits viscosity/diffusion in horizontal and vertical, and these coefficients parameterize most of the mixing, while in the LES model Nek5000 mixing is mostly represented by resolved turbulence and subgrid-scale parameterizations are of marginal influence.

For the LE, Nek5000 is configured exactly as described in Özgökmen et al. (2009b), but here the model is run approximately four times longer to include later stages when the collapse of turbulence to internal waves become important. Although the mixing rate is significantly reduced after this transition, turbulence is not totally shut off and small amounts of mixing taking place over a long period can also be important. We summarize the selection of the non-dimensional parameters in (2.1) as:  $a = L/H_0 = 2$ ,  $W/H_0 = 1$  (where  $W$  is the horizontal width in the domain),  $Fr = 2^{-\frac{1}{2}}$  and  $Pr = 7$ . The only remaining physical parameter of the problem is  $Re$  and we conduct LES simulations at two Reynolds numbers, namely  $Re = 10^3$  and  $Re = 10^4$ . These LES simulations are used as our ground truth. The reader is referred to experiments low-res2 ( $Re = 10^3$ ) and high-res2 ( $Re = 10^4$ ) described in Özgökmen et al. (2009b) for additional details on these simulations.

In ROMS, the horizontal and vertical length scales are set to  $L = 200$  and  $H = 100$  m, respectively, given an aspect ratio of  $a = 2$ . The width of the domain is set to  $W = 100$  m. The Froude number  $Fr$  is the ratio between the characteristic advection speed, defined as  $U_0 = \frac{1}{2}\sqrt{g\Delta\rho'H/\rho_0}$  (Özgökmen et al., 2009b), and the internal wave speed, defined as  $\sqrt{g\Delta\rho'l/\rho_0}$ , where  $l = H/2 = 50$  m. Thus, for this configuration  $Fr = 2^{-\frac{1}{2}}$  regardless of the choice for the density perturbation ( $\rho'$ ). As shown in Section 2.2.2, ROMS separates viscosity/diffusivity in vertical and horizontal. Therefore, we introduce  $Pr_V$  ( $Re_V$ ) and  $Pr_H$  ( $Re_H$ ) as the vertical and horizontal Prandtl (Reynolds) numbers, respectively. The values of the explicit  $Re_H$  used in this study are listed in Table 4.1. Although we set  $Pr_H = 7$  (i.e., momentum diffuses seven times faster than heat in the horizontal), we cannot guarantee that  $K_{CH}$  is always larger than the numerical diffusion from the tracer advection scheme (hence, it is more appropriate to say that  $Pr_H \leq 7$ ). Additional inconsistency between Nek5000 and ROMS is the fact that both  $Pr_V$  and  $Re_V$  are controlled by the turbulent closure. The reason is that  $K_{MV}$  and  $K_{CV}$  are set according to the schemes of each closure. Nevertheless, we conduct three control experiments where  $K_{MV}$  and  $K_{CV}$  are set analytically to constant values (more details in Section 2.3.2).

At the northern and southern sides, periodic boundary conditions are applied, while at the eastern and western walls no-flow and free-slip boundary conditions are used. The effects of bottom friction are ignored (i.e.,  $C_D = 0$ ).

The LE problem is initialized with dense fluid on the left separated from light fluid on the right:

$$\frac{\rho'(x, y, z, 0)}{\Delta\rho'} = \begin{cases} 1 & \text{for } 0 \leq x < (L/2 + \eta), \\ 0 & \text{for } (L/2 + \eta) \leq x \leq L, \end{cases} \quad (2.8)$$

where  $\eta$  is a function that defines the perturbation to be superimposed on the density interface to generate 3D flows. For the LE experiments presented in the following section a perturbation of the form  $\eta = 10 \times \sin(\pi y/W)$  is used. A similar perturbation is employed in Özgökmen et al. (2009b). The system starts from a state of rest,  $\mathbf{u} = 0$ , and it is integrated until the rate of stratified mixing becomes negligible with respect to the initial vigorous activity. One important time scale for the system is the time it takes for the internal gravity currents to cross the domain  $T_p = L/U_0$ . The total integration period ( $T$ ) needs to be much larger than  $T_p$  for the effects of stratification to fully develop. Both ROMS and Nek5000 simulations are integrated until non-dimensional time of  $t^* = 4 \times T/T_p \approx 60$ .

### 2.3.2 List of experiments and quantification of mixing

Table 4.1 presents the set of sixteen LE experiments conducted with different configurations in terms of: (i) grid resolution, (ii) choice of turbulence closures (with the values of vertical background viscosity  $K_{MV}^0$  and diffusivity  $K_{CV}^0$  used when using KPP-Ri, see more details below), (iii) tracer advection scheme and (iv) explicit horizontal Reynolds number ( $Re_H$ ). The following rationale is used when specifying the simulation names (e.g., le-10-k $\varepsilon$ -10 $^3$ ): type of problem - grid resolution ( $\Delta x = \Delta y = \Delta z$ ) - turbulence closure, or tracer advection scheme, or absence of vertical mixing (novmix), or fixed  $K_{MV}$  and  $K_{CV}$  values (ctrl) -  $Re_H$  value.

The main purpose of changing spatial resolution is to examine the sensitivity of the results on grid resolution. Ideally, resolution-independent results would be desirable. Four values are tested here: 10, 5, 2.5 and 1.25 m. We assure that in all experiments run at  $Re_H = 10^3$  the implicit numerical diffusion (which acts as implicit viscosity), in the advection operator, is smaller than the explicit horizontal eddy viscosity ( $K_{MH}$ ). We use an asymptotic analysis, similar to that employed in Dong et al. (2007), to

**Table 2.1:** List of LE experiments conducted with ROMS. The number of grid points in the  $x$ ,  $y$  and  $z$  directions are:  $20 \times 10 \times 10 = 2,000$  for  $\Delta x = \Delta y = \Delta z = 10$  m,  $40 \times 20 \times 20 = 16,000$  for  $\Delta x = \Delta y = \Delta z = 5$  m,  $80 \times 40 \times 40 = 128,000$  for  $\Delta x = \Delta y = \Delta z = 2.5$  m, and  $160 \times 80 \times 80 = 1,024,000$  for  $\Delta x = \Delta y = \Delta z = 1.25$  m. CA = Canuto-A stability function, and  $K_{MV}$  ( $K_{MV}^0$ ) and  $K_{CV}$  ( $K_{CV}^0$ ) are the vertical (background) viscosity and diffusivity, respectively. The symbol \* indicates that a combination of third-order upstream-biased horizontal scheme and fourth-order centered vertical scheme is used.

Experiment	$\Delta x$ (m)	$Re_H$	Turb. closure	$K_{CV}^0$ ( $m^2 s^{-1}$ )	$K_{MV}^0$ ( $m^2 s^{-1}$ )
le-10-k $\varepsilon$ -10 $^3$	10	10 $^3$	k- $\varepsilon$ /CA		
le-10-kpp-10 $^3$	10	10 $^3$	KPP-Ri	$1.60 \times 10^{-3}$	$1.12 \times 10^{-2}$
le-5-k $\varepsilon$ -10 $^3$	5	10 $^3$	k- $\varepsilon$ /CA		
le-5-kpp-10 $^3$	5	10 $^3$	KPP-Ri	$1.60 \times 10^{-3}$	$1.12 \times 10^{-2}$
le-2.5-k $\varepsilon$ -10 $^3$	2.5	10 $^3$	k- $\varepsilon$ /CA		
le-2.5-kpp-10 $^3$	2.5	10 $^3$	KPP-Ri	$1.60 \times 10^{-3}$	$1.12 \times 10^{-2}$
le-2.5-u3h-10 $^{3*}$	2.5	10 $^3$	k- $\varepsilon$ /CA		
le-1.25-k $\varepsilon$ -10 $^3$	1.25	10 $^3$	k- $\varepsilon$ /CA		
le-1.25-kpp-10 $^3$	1.25	10 $^3$	KPP-Ri	$1.60 \times 10^{-3}$	$1.12 \times 10^{-2}$
le-1.25-k $\varepsilon$ -10 $^4$	1.25	10 $^4$	k- $\varepsilon$ /CA		
le-1.25-kpp-10 $^4$	1.25	10 $^4$	KPP-Ri	$1.60 \times 10^{-4}$	$1.12 \times 10^{-3}$
				$K_{CV}$ ( $m^2 s^{-1}$ )	$K_{MV}$ ( $m^2 s^{-1}$ )
le-1.25-ctrl-10 $^3$	1.25	10 $^3$	none	$1.60 \times 10^{-3}$	$1.12 \times 10^{-2}$
le-1.25-ctrl-10 $^4$	1.25	10 $^4$	none	$1.60 \times 10^{-4}$	$1.12 \times 10^{-3}$
le-1.25-novmix-10 $^3$	1.25	10 $^3$	none	0	0

assure that the implicit numerical diffusion associated with the advection operator is smaller than the prescribed explicit horizontal eddy viscosity ( $K_{MH}$ ). Fig. 2.1 shows the time evolution of BPE\* using a set of values for  $K_{MH}$ , while keeping all the other parameters consistent with experiment le-10-k $\varepsilon$ -10 $^3$ . The  $K_{MH}$  values were set to  $1.12 \times 10^{-1}$ ,  $1.60 \times 10^{-2}$ ,  $1.12 \times 10^{-2}$  and 0  $m^2 s^{-1}$  corresponding to  $Re_H$

values of 100, 700, 1000 and implicit (i.e., entirely controlled by the implicit numerical diffusion), respectively. Initially (until  $t^*=2$ ) all the cases display similar results, but then an increase in  $BPE^*$  (or mixing) is achieved by decreasing  $K_{MH}$  (or by increasing  $Re_H$ ). Note that although  $Re_H$  is taken to infinity (by setting  $K_{MH} = 0 \text{ m}^2/\text{s}$ ) the effective  $Re$  remains finite because of the implicit numerical diffusion. We should point out that in the experiments run at  $Re_H = 10^4$  the implicit horizontal numerical diffusion approaches the explicit  $K_{MH}$  and, therefore, we have no control over  $Re_H$  (even though we state that  $Re_H = 10^4$  in those experiments). Nevertheless, we use these simulations to show that the results become completely independent to the choice of turbulence closure when the effective  $Re_H$  is large and entirely controlled by numerical diffusion.

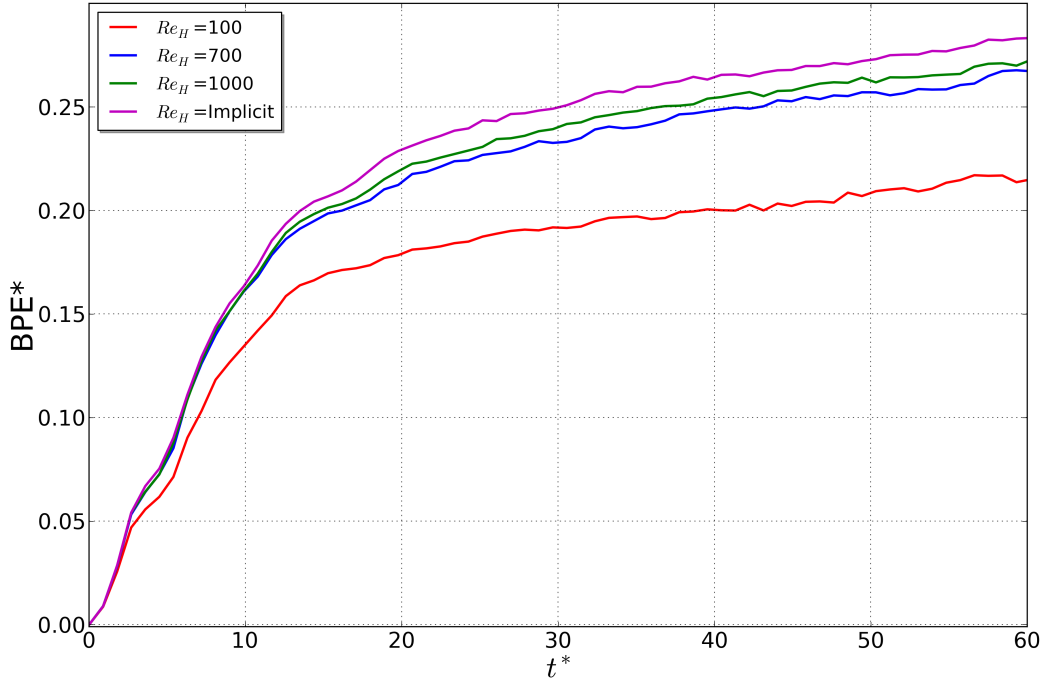


**Figure 2.1:** Time evolutions of the normalized background potential energy  $BPE^*$  from ROMS experiments with 10 m resolution and different explicit horizontal Reynolds number ( $Re_H$ ) values.

To investigate the effects of tracer advection schemes on mixing, we run experiment le-2.5-u3h- $10^3$ , where a combination of third-order upstream-biased horizontal scheme (U3H) and fourth-order centered vertical scheme (C4V) is used. All the other experiments are carried using the multidimensional positive definite advection transport algorithm (MPDATA). The MPDATA algorithm conserves mass and it preserves the positive-definite characteristics of the tracers, which avoids under- and overshooting of the initial tracer values. The sensitivity of mixing on the explicit horizontal Reynolds number ( $Re_H$ ) is assessed by running experiments at two  $Re_H$  values ( $10^3$  and  $10^4$ ). Finally, the effects of turbulence closures on mixing are investigated by selecting two popular models:

1. The algebraic K-Profile Parameterization model (KPP) (Large et al., 1994).

Here, only the component due to resolved vertical shear is considered. Shear-driven mixing is expressed in terms of the local gradient Richardson number,

$$Ri_g = N^2 \left[ \left( \frac{\partial u}{\partial z} \right)^2 + \left( \frac{\partial v}{\partial z} \right)^2 \right]^{-1} \quad (2.9)$$

which is the ratio between the buoyancy frequency and the vertical shear. Vertical eddy viscosity is then estimated as:

$$K_{MV} = \begin{cases} K_{MV}^0 & \text{for } Ri_g < 0, \\ K_{MV}^0 [1 - (Ri_g/Ri_0)^2]^3 & \text{for } 0 < Ri_g < Ri_0, \\ 0 & \text{for } Ri_g > Ri_0, \end{cases} \quad (2.10)$$

where  $Ri_0 = 0.7$ . Equation (2.10) is also used to compute  $K_{CV}$ , but a background diffusivity coefficient ( $K_{CV}^0$ ) is used instead of that for viscosity ( $K_{MV}^0$ ).

These coefficients are prescribed by the user and the values used in our LE runs are listed in Table 4.1.

2. The two-equation standard  $k-\varepsilon$  closure (Burchard and Baumert, 1995a) for stratified flow with Canuto-A stability function (Canuto et al., 2001). We choose  $k-\varepsilon/CA$  based on a recent evaluation of turbulence closures in three-dimensional simulations of the Red Sea overflow (Ilicak et al., 2008). The  $k-\varepsilon$  model uses transport equations for turbulent kinetic energy (TKE) and the dissipation rate  $\varepsilon$  of the TKE, while the Canuto-A stability function includes the effects of shear and stratification. Unlike the shear-driven mixing in KPP, the user does not need to prescribe the value of any coefficient in this closure. The reader is referred to Warner et al. (2005b) (and references therein) for a complete description of  $k-\varepsilon/CA$  and their implementation in ROMS.

Additionally, three control experiments where both  $K_{MV}$  and  $K_{CV}$  are set to fixed values (no turbulence closure is used) are conducted. In experiment le-1.25-ctrl- $10^3$  we set  $K_{MV} = 1.12 \times 10^{-2} \text{ m}^2 \text{ s}^{-1}$  and  $K_{CV} = 1.60 \times 10^{-3} \text{ m}^2 \text{ s}^{-1}$ , while in experiment le-1.25-ctrl- $10^4$  these parameters are set to  $1.12 \times 10^{-3} \text{ m}^2 \text{ s}^{-1}$  and  $1.60 \times 10^{-4} \text{ m}^2 \text{ s}^{-1}$ , respectively (see Table 4.1). Experiment le-1.25-novmix- $10^3$  is intended to explore the absence of vertical mixing ( $K_{MV} = K_{CV} = 0$ ) on the system while keeping  $Re_H = 10^3$ .

In ROMS, the baroclinic time step is set to  $\Delta x/500$  seconds and the number of barotropic time steps between each baroclinic time step is set to 20. This yields a maximum lateral CFL number of  $8.8 \times 10^{-2}$  for all simulations. ROMS experiments are conducted on University of Miami's Linux cluster (IBM iDataPlex dx360M4) based on 16 Intel Sandy Bridge 2.6 GHz cores, 32 GB of RAM and infiniBand clustering network, while Nek5000 experiments have been carried out on a Cray XE6m

machine at the City University of New York High-Performance Computer Center<sup>1</sup>. ROMS and Nek5000 scale at approximately  $1\text{-}5 \times 10^4$  and  $5\text{-}10 \times 10^3$  grid points per node, respectively. The number of nodes for each experiment as well as the wall clock time for an integration  $t^* \approx 60$  are listed in Table 2.2.

For this application, the metric used is the background (or reference) potential energy (BPE), which quantifies mixing in a enclosed system (Winters et al., 1995), such as the lock-exchange domain employed here. BPE is defined as the minimum potential energy that can be obtained through an adiabatic redistribution of the water masses. Mixing increases the BPE, since it provides a direct measure of the potential energy changes due to irreversible diapycnal mixing. This metric has been widely used to compute mixing in numerical simulations of turbulent flows (Winters et al., 1995; Tseng and Ferziger, 2001; Özgökmen et al., 2007; Özgökmen et al., 2009a,b; Ilicak et al., 2009, 2012) and the reader is referred to Özgökmen et al. (2007, Fig.5 and associated text) for a detailed discussion on how changes in BPE relate to diapycnal mixing in the LE problem.

We follow the technique introduced by Tseng and Ferziger (2001) to compute BPE using the probability density function. In our analysis the density perturbation is split into 51 bins at each time step, and integrated:

$$BPE = gLW \int_0^H \rho'(z_r) z_r dz_r, \quad (2.11)$$

where  $z_r(\rho')$  is the height of fluid of density  $\rho'$  in the minimum potential energy state. The  $\rho'$  bins are fixed in time and vary between the minimum and maximum values at  $t^* = 0$  ( $0$  and  $1 \text{ kg m}^{-3}$ , respectively). Therefore, the under- and over-shootings discussed in Section 2.3.4 are not included in the calculation of BPE. We present the results in terms of the non-dimensional background potential energy, defined as:

---

<sup>1</sup><http://www.csi.cuny.edu/cunyhpc/>

**Table 2.2:** Wall clock time and the number of nodes used in the LE and MLI experiments.

Experiment	# of nodes	Wall clock time (hours)
le-10-k $\varepsilon$ -10 $^3$	1	0.1
le-10-kpp-10 $^3$	1	0.1
le-5-k $\varepsilon$ -10 $^3$	1	0.9
le-5-kpp-10 $^3$	1	0.7
le-2.5-k $\varepsilon$ -10 $^3$	8	2.2
le-2.5-kpp-10 $^3$	8	1.5
le-2.5-u3h-10 $^{3*}$	8	1.2
le-1.25-k $\varepsilon$ -10 $^3$	32	16.5
le-1.25-kpp-10 $^3$	32	10.4
le-1.25-k $\varepsilon$ -10 $^4$	32	20.2
le-1.25-kpp-10 $^4$	32	14.1
le-1.25-ctrl-10 $^3$	32	13.1
le-1.25-ctrl-10 $^4$	32	13.2
le-1.25-novmix-10 $^3$	32	13.2
le-LES (10 $^3$ )	16	308
le-LES (10 $^4$ )	384	48,000
mli-100-32-k $\varepsilon$	16	2.3
mli-200-32-k $\varepsilon$	4	0.7
mli-50-32-k $\varepsilon$	64	4.7
mli-100-16-k $\varepsilon$	4	2.9
mli-100-64-k $\varepsilon$	36	2.0
mli-100-32-kpp	16	1.5
mli-100-32-novmix	16	1.4
mli-LES	256	192

$$BPE^* = \frac{BPE(t^*) - BPE(t^* = 0)}{BPE(t^* = 0)} \quad (2.12)$$

It is convenient to use equation (2.12) to visualize the relative increase of the BPE with respect to the initial state by mixing. We highlight that  $BPE^* \geq 0$  and it increases monotonically for physically realistic solutions.

### 2.3.3 Description of the flow

Since active tracer fields are a convenient way of visualizing stratified turbulent flows, we use the normalized density perturbation field ( $\rho'/\Delta\rho'$ ) to describe the evolution of the LE problem. We choose the results from experiments le-1.25-k $\varepsilon$ -10<sup>4</sup> (see Table 4.1) and the LES ( $Re=10^4$ ) simulation to described the time evolution of  $\rho'/\Delta\rho'$ . At  $t^* = 4.1$  (Figs. 2.2 a and b), mixing is enhanced when the two gravity currents, traveling in opposite directions, collide on the center of the domain. The three-dimensionality of the flow, resulting from the initial sinusoidal perturbation, is evident at this stage in both ROMS and LES simulations. The solution in the ROMS simulation is much less smooth than in the LES. As pointed out by Ilicak et al. (2012), the lock-exchange problem is characterized by noise divergencies in the horizontal velocities near the head of the counter-propagating gravity currents, which are related to large energy in the velocity at or near the horizontal grid scale. Although the momentum advection scheme used in ROMS has viscous dissipation built into it to ensure that the flow field is smooth at the grid scale (Shchepetkin and McWilliams, 1998), our results show that the effectiveness of this mitigation is reduced at small  $\Delta x$  and high  $Re_H$  (see following section for further discussion). Towards the end of the simulation (Figs. 2.2 c and d) the density perturbation becomes smoother as shear decreases, while the density interface becomes thicker as a result of mixing. Due to the difference in the internal wave speed (dispersion) between the hydrostatic (ROMS) and the non-hydrostatic

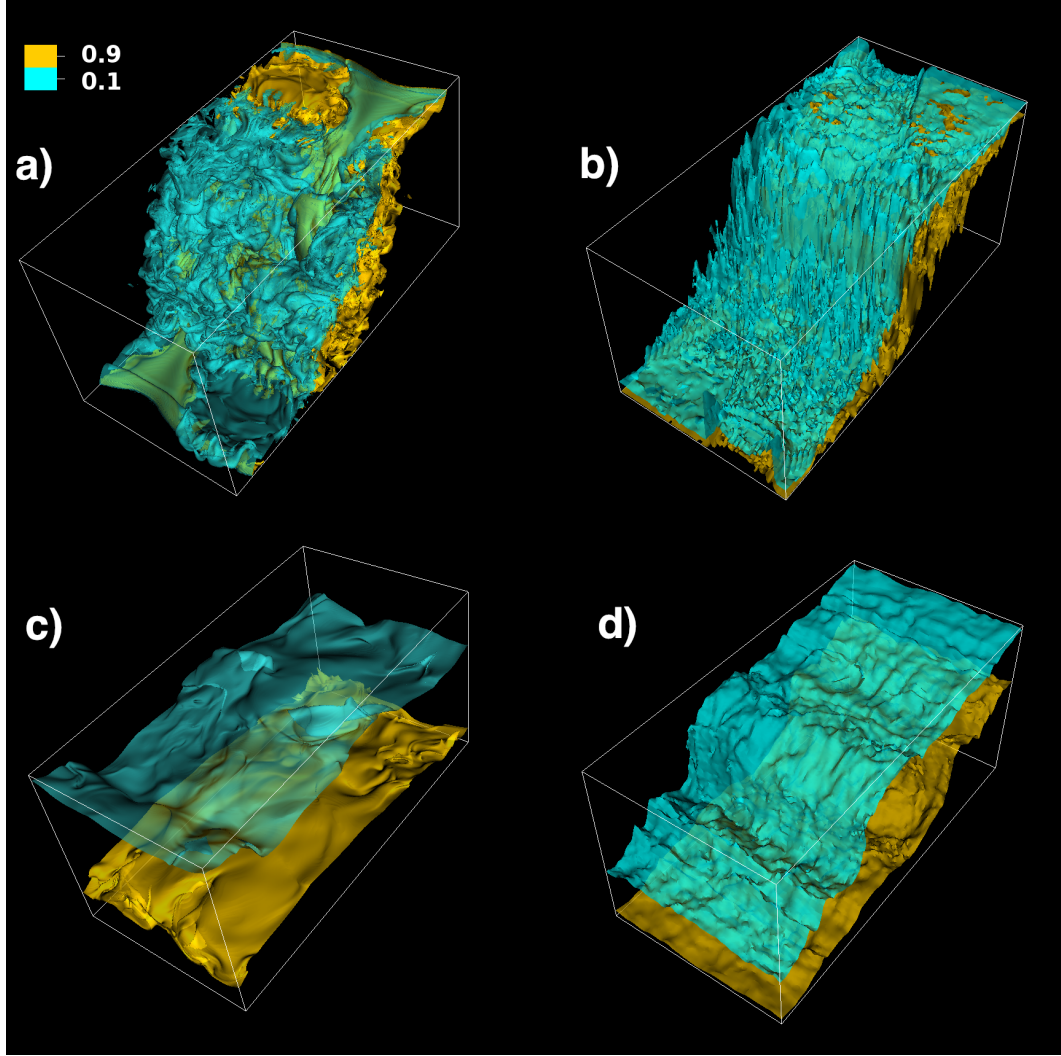


**Figure 2.2:** Contours of the normalized density perturbation  $\rho'/\Delta\rho'$  values for the (left panels) Nek5000 simulation LES ( $Re=10^4$ ) and (right panels) ROMS experiment le-1.25-k $\varepsilon$ -10 $^4$  (see Table 4.1) during two non-dimensional times  $t^* = 4.1$  (a and b) and  $t^* = 47.6$  (c and d). The contours values are 0.1 (blue) and 0.9 (yellow).

(LES) simulations, the flows no longer exhibit similar behavior (e.g., the position of gravity current fronts) as  $t^*$  increases (Figs. 2.2 c and d). Although not explored in the present study, it is known that hydrostatic models cannot produce the correct dispersion for non-linear internal waves (Scotti and Mitran, 2008). In addition, the choice of numerical schemes may also play an important role on the speed of internal

waves (Hedges et al., 2006) and further studies should be done to address these issues. In the following sections we focus in quantifying mixing during the time evolution of the LE problem.

### 2.3.4 Comparison of mixing from LES and ROMS

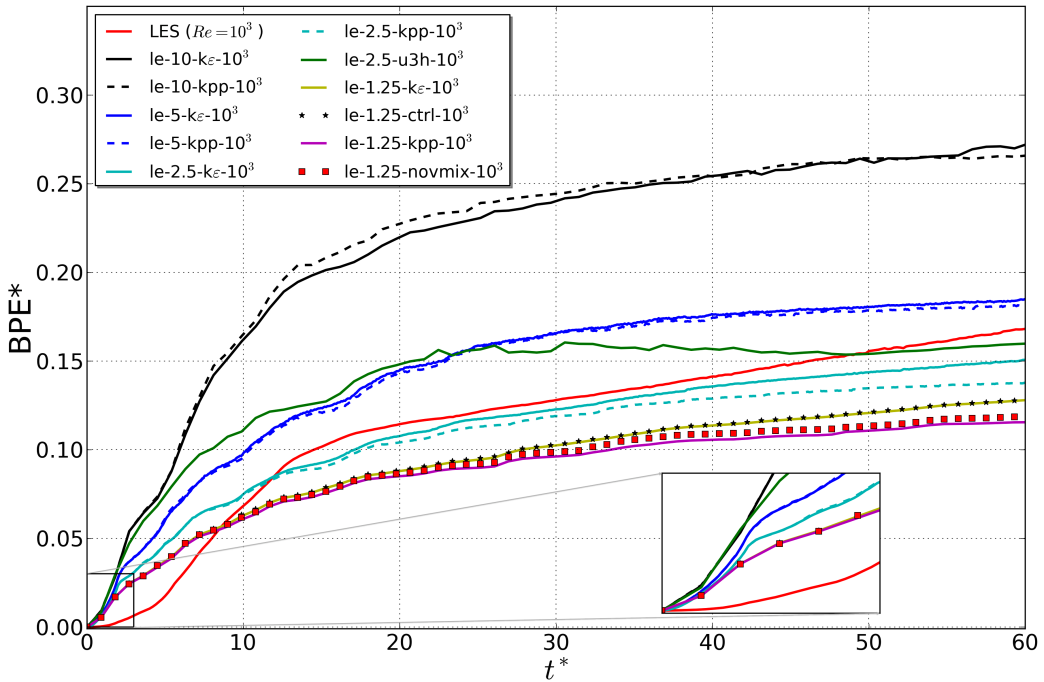


**Figure 2.3:** Time evolutions of the normalized background potential energy  $BPE^*$  from experiments with  $\Delta x = 10, 5, 2.5$  and  $1.25$  m and  $Re_H = 10^3$ . The curve from the reference LES ( $Re = 10^3$ ) experiment is also shown for comparison. Note the overlap between curves from experiments  $le-1.25-k\epsilon-10^3$  and  $le-1.25-ctrl-10^3$ ; and  $le-1.25-kpp-10^3$  and  $le-1.25-novmix-10^3$ . The lower panel on the right shows an expanded plot of the initial evolution of  $BPE^*$ .

In this section, the sensitivity of mixing to the modeling choices presented in Section 2.3.2 are explored.

Figs. 2.3 and 2.4 show the time evolution of the non-dimensional background potential energy  $BPE^*$  for all experiments listed in Table 4.1. Until  $t^* \approx 2$ , when the

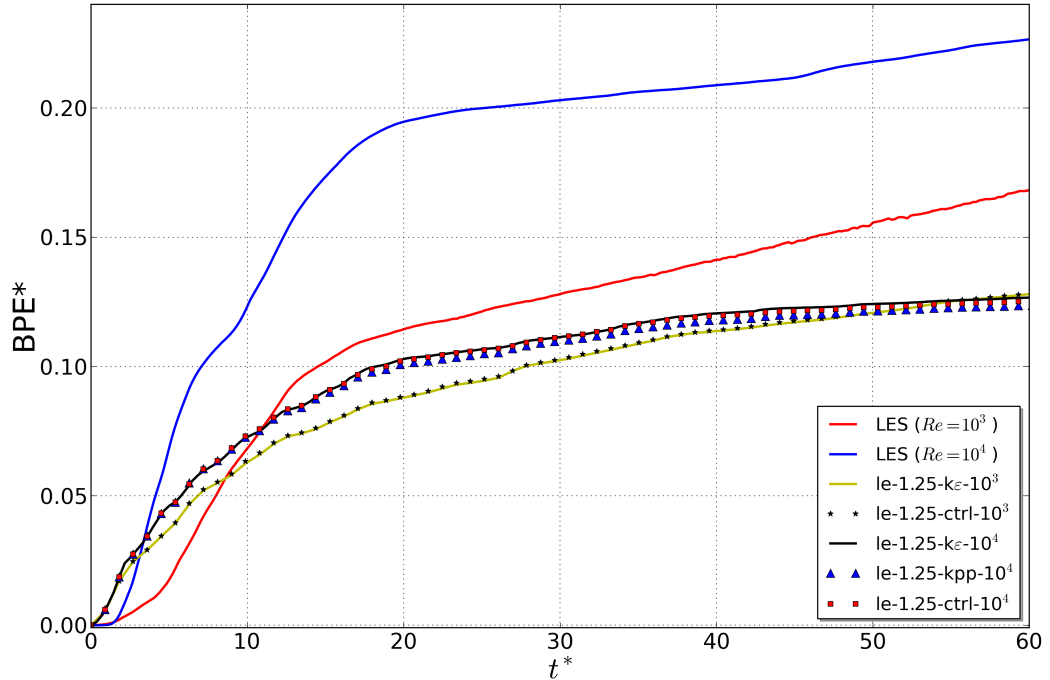


**Figure 2.4:** Time evolutions of the normalized background potential energy  $BPE^*$  from experiments with  $\Delta x=1.25$  m and  $Re_H=10^3$  and  $10^4$ . The curves from the reference LES ( $Re=10^3$ ) and LES ( $Re=10^4$ ) experiments are also shown for comparison. Note the overlap between curves from experiments le-1.25-k $\varepsilon$ -10 $^3$  and le-1.25-ctrl-10 $^3$ ; and le-1.25-k $\varepsilon$ -10 $^4$ , le-1.25-kpp-10 $^4$  and le-1.25-ctrl-10 $^4$

two counter-propagating gravity currents collide on the wall, the  $BPE^*$  curves in the different ROMS simulations are very similar and display larger mixing (and mixing rate) than the LES simulations. However, shortly after, the ROMS simulations display different patterns among themselves and, overall, there is a small decrease in the  $BPE^*$  slope. On the other hand, the mixing rate in the LES experiments is enhanced after the two gravity currents collide on the center of the domain ( $t^* \approx 4.1$ ).

Overall, the flow in both ROMS and LES follows two stages during the evolution of the LE problem. First, shear-driven mixing dominates and the mixing increases rapidly. Second (after  $t^* \approx 15$ ), a fairly abrupt change in the regime occurs when the collapse of turbulence to internal waves takes place. In all runs this occurs approxi-

mately right after the two gravity currents, traveling at opposite direction, collide on the center of the domain for the third time. The initial (shear-driven) mixing rate is reduced in simulations with  $\Delta x = 1.25$  m and, therefore, this collapse becomes less pronounced in these runs. Shear-driven mixing is now sparse (as shown by the smoother contours in Figs. 2.2 c and d, and corresponding animations) and the mixing rate decreases significantly during this last stage (Figs. 2.3 and 2.4).

In cases with  $Re_H=10^3$ , mixing from ROMS as quantified by BPE\* is found to decrease with finer spatial resolution, as follows: the cases with 10 m resolution significantly overestimate mixing and the results are greatly improved when the resolution is increased to 5 m (although mixing is still overestimated); those with 2.5 m resolution give the most accurate results; and those with 1.25 m resolution lead to an underestimation of mixing with respect to the LES curve (Fig. 2.3). Thus, no convergence of results is achieved, as the mixing curves from ROMS keep changing with spatial resolution. Also, during the initial stage (when shear-driven mixing dominates), the results are not sensitive to the choice of turbulence closure. However, as the system approaches the internal wave regime, KPP-Ri tends to give somewhat more mixing than  $k-\varepsilon$  at coarser resolutions (10 and 5 m) and less mixing at finer resolutions (2.5 and 1.25 m). Nevertheless, the difference in mixing obtained with these closures is not significant when compared to the difference in mixing obtained when varying the model resolution.

The experiment with 2.5 m resolution and U3H/C4V tracer advection scheme (le-2.5-u3h- $10^3$ ) shows excessive mixing until about  $t^* \approx 25$  and the BPE\* then decreases for  $25 \leq t^* \leq 50$ , which is an unphysical behavior (Fig. 2.3). Fig. 2.5 shows the probability density function of temperature at four non-dimensional times and for the different tracer advection schemes evaluated here. Initially (at  $t^* = 0$ , not shown), only two temperature values are presented (highlighted by the black lines in

Figs. 2.5a-d) and each correspond to 50% of the total volume. At  $t^* = 0.7$  (Fig. 2.5a), a range of new temperature values have formed as a consequence of mixing and with the U3H/C4V scheme a significant percentage of the total volume falls outside the initial temperature range. There is a large increase in the amount of intermediate temperature values generated during the initial stage, when shear-driven mixing dominates (compare Figs. 2.5a and b), and, therefore, the BPE\* curves increase monotonically regardless of the tracer advection scheme (Fig. 2.3).

Ilicak et al. (2012) used the lock-exchange case to analyze the spurious dianeutral transport in a suite of ocean models. They compared the effect of two tracer advection schemes implemented in the MITgcm model (the non-monotonic second order moment scheme of Prather (1986); and a monotonic 7th-order scheme) and also found that new water masses with densities outside the initial range were generated when using the scheme without a flux limiter (Prather). They also highlighted that the noisy vertical velocity (due to the strong lateral flow divergence) can lead to a nontrivial degree of flux limiting introduced by the monotonic scheme, which would result in large spurious mixing. Here, on the other hand, we found that the monotonic scheme (MPDATA) gives less mixing when compared to U3H/C4V. We present two plausible hypotheses for this behaviour. First, the amount of diffusion introduced by the velocity dependent hyper-viscosity from the tracer advection scheme U3H may overcome the effect of the flux limiting on mixing due to the noisy vertical velocity. Since the solutions become smoother as the collapse of turbulence to internal waves takes place, this could explain the decrease in BPE for U3H/C4V scheme at later times. A second hypothesis takes in consideration the fact that the over- and under-shootings observed at the initial stages (Fig. 2.5 a and b) are not included in the BPE calculation (see Section 2.3.2). The decrease in the BPE for the U3H/CV4 scheme at later times may then, in fact, be due to a reduced impact of the over- and

under-shootings (Fig. 2.5 c and d), rather than some kind of “unmixing” or numerical artifact. Clearly both hypotheses require further investigation, which is beyond the scope of this article.

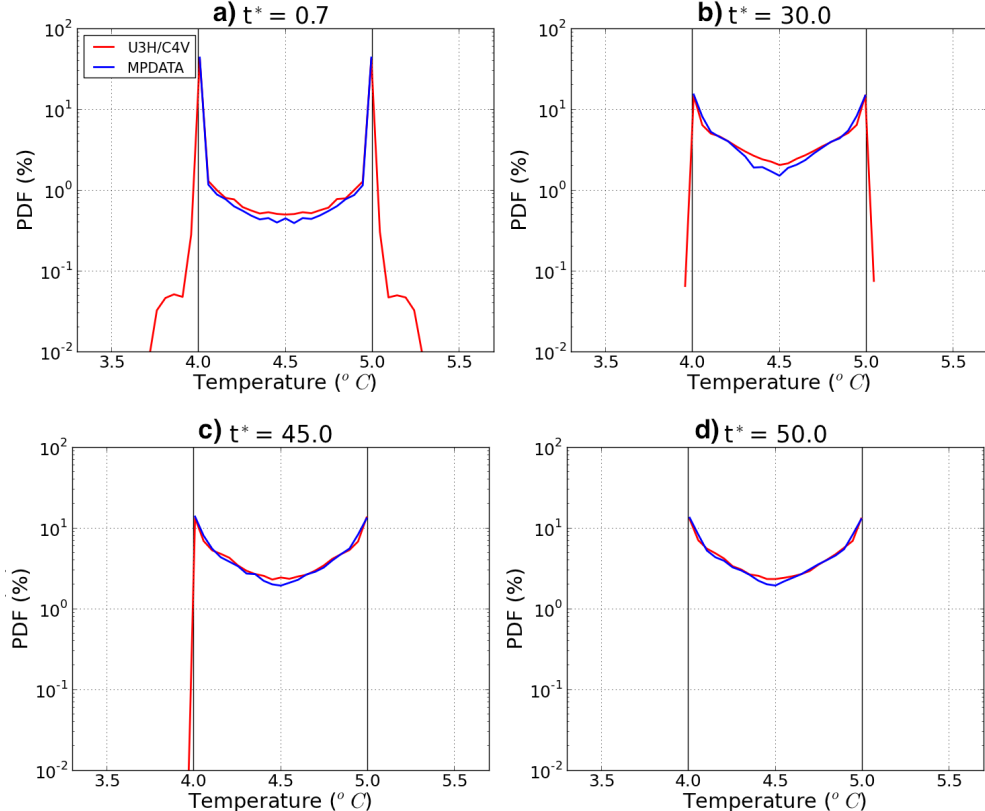


**Figure 2.5:** Probability density function (pdf, in %) of temperature ( $^{\circ}\text{C}$ ) at a)  $t^*=0.7$ , b)  $t^*=30.0$ , c)  $t^*=45.0$  and d)  $t^*=50.0$  for the different tracer advection schemes evaluated here, namely MPDATA and U3H/C4V (experiments le-2.5-k $\varepsilon$ - $10^3$  and le-2.5-u3h- $10^3$ , respectively). The initial temperature values are highlighted by the solid black lines.

In the case with  $Re_H=10^4$ , results from 1.25 m resolution ROMS computations seem to lead to large errors, independently from the closures used (Fig. 2.4). The LES results show a clear increase in mixing as  $Re$  is increased while in ROMS such growth is not very pronounced. The spatial resolution of 1.25 m does not allow us to keep the implicit numerical diffusion smaller than  $K_{MH} = 1.12 \times 10^{-3} \text{ m}^2 \text{ s}^{-1}$ ,

which leads to an unintended increase in the effective  $Re_H$  of the system. Clearly, one may also opt to go with coarser resolution and obtain higher mixing by numerical effects. Nevertheless, this cannot be considered as a systematic and reliable modeling approach to turbulent mixing problems.

To better quantify the difference between the BPE\* curves derived from ROMS and LES, we compute the normalized root-mean-square error ( $\Gamma$ ) defined as

$$\Gamma = \frac{\sqrt{\frac{1}{n} \sum_{i=0}^n (\hat{\theta}_i - \theta_i)^2}}{\hat{\theta}_{max} - \hat{\theta}_{min}}, \quad (2.13)$$

where  $\hat{\theta}$  and  $\theta$  are the BPE\* values for the LES and ROMS, respectively, and  $n$  is the number of points compared. The values of  $\Gamma$  as a function of the inverse grid resolution (wave-number) are presented in Fig. 2.6. Each experiment is compared with the respective LES ( $Re = 10^3$  and  $10^4$ ) based on their  $Re_H$  value.

From Figs. 2.3, 2.4 and 2.6, it is clear that the best results are achieved with experiments le-2.5-k $\varepsilon$ - $10^3$  and le-2.5-kpp- $10^3$  ( $\Gamma = 6.9$  and  $8.7\%$ , respectively). The coarser resolution cases, le-10-k $\varepsilon$ - $10^3$  and le-10-kpp- $10^3$  ( $\Gamma = 60.5$  and  $62.5\%$ , respectively) and le-5-k $\varepsilon$ - $10^3$  and le-5-kpp- $10^3$  ( $\Gamma = 18.4$  and  $19.6\%$ , respectively), overestimate mixing, while the higher resolution cases le-1.25-k $\varepsilon$ - $10^3$  and le-1.25-kpp- $10^3$  ( $\Gamma = 16.0$  and  $18.7\%$ , respectively) underestimate it. Experiments using different turbulence closures and  $Re_H=10^3$  do not show a significant difference in mixing relative to the difference obtained using different modeling choices. Therefore, the choice of turbulence closure plays a minor role in this problem. Experiments carried at higher  $Re_H$  ( $10^4$ ) show that mixing is underestimated with respect to the reference results, with errors increasing by a factor of approximately 2 (le-1.25-k $\varepsilon$ - $10^4$   $\approx$  le-2.5-kpp- $10^4$   $\approx$  le-2.5-ctrl- $10^4$ ,  $\Gamma \approx 37.0\%$ ) compared to cases where  $Re_H = 10^3$ . This is expected since the implicit numerical diffusion associated with the horizontal advection scheme does

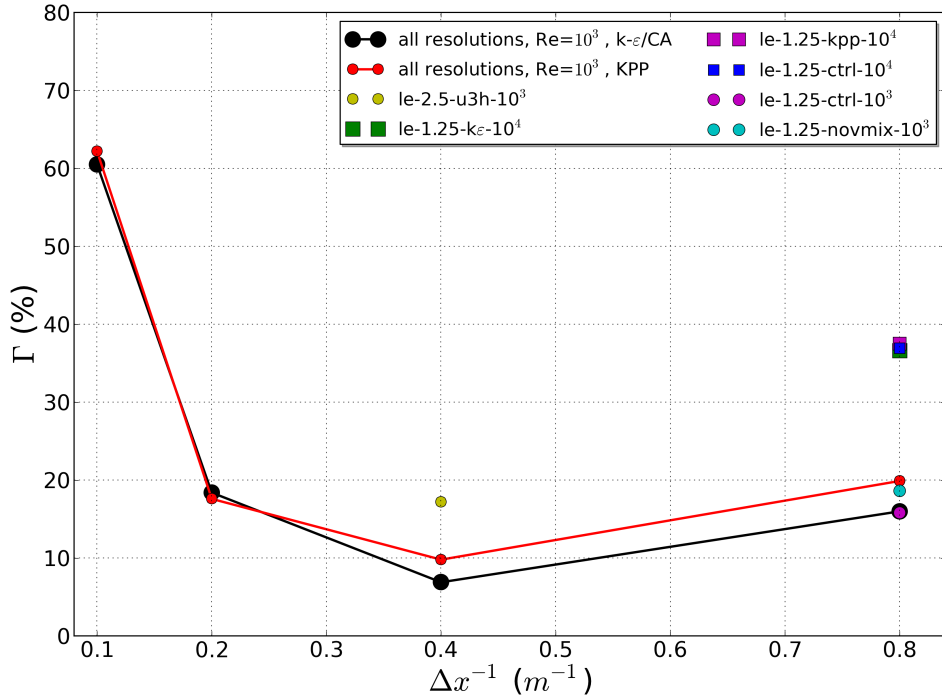


**Figure 2.6:** BPE\* normalized root-mean-square errors ( $\Gamma$ , defined by (2.13) see text for details) as a function of the inverse grid resolution ( $\Delta x^{-1}$ ,  $m^{-1}$ ) for all ROMS experiments presented in Table 4.1. Note the overlap between points from experiments le-1.25-k $\varepsilon$ -10 $^3$  and le-1.25-ctrl-10 $^3$ ; le-1.25-k $\varepsilon$ -10 $^4$ , le-1.25-kpp-10 $^4$  and le-1.25-ctrl-10 $^4$ ; and le-1.25-novmix-10 $^3$  and le-1.25-kpp-10 $^3$ .

not allow the effective  $Re_H$  to be increased to 10 $^4$  at this resolution. We highlight that there are no significant differences between experiments le-1.25-k $\varepsilon$ -10 $^4$ , le-2.5-kpp-10 $^4$ , le-2.5-ctrl-10 $^4$ , suggesting that, when the specified  $Re_H$  is large, the implicit horizontal numerical diffusion is more influential than the choice of turbulence closure used.

Results from experiment le-2.5-u3h-10 $^3$  show that mixing is significantly changed when the tracer advection scheme formed by U3H/C4V is applied ( $\Gamma = 17.2\%$ , compared to 6.9 % achieved using MPDATA). The overall (all resolutions) change in  $\Gamma$  due to different vertical turbulence closures is  $\sim 2\%$ , while the difference in  $\Gamma$  due to different tracer advection schemes is of 10.3 %. The error obtained with

U3H/C4V is equivalent to those achieved with a coarser grid resolution ( $\Delta x = 5$  m) and, therefore, this is considered excessive mixing. It should be noted, however, that the combination formed by U3H/C4V is significantly cheaper in terms of computation time than MPDATA (Table 2.2). Additional combinations (not shown) formed by U3H and a splines vertical scheme (U3H/Splines) also result in excessive mixing ( $\Gamma = 16.2\%$ ). Even larger mixing is achieved when using the ROMS default fourth-order centered for both horizontal and vertical schemes (C4H/C4V,  $\Gamma = 37.6\%$ ); and a fourth-order centered as the horizontal scheme with a splines vertical scheme (C4H/Splines,  $\Gamma = 37.8\%$ ). All these combinations also show over- and under-shootings in the probability density function of temperature during the initial stage and the lack of monotonicity in the BPE curve at latter times.

The convergence achieved with the different grid resolutions and tracer advection schemes should be interpreted with caution. Resolving the small-scale sharp gradients in the density field during the evolution of the LE problem is a challenging task for any OGCM. The hydrostatic approximation breaks down when the condition  $Fr^2a^{-2} \ll 1$  does not hold (McWilliams, 1985a; Vallis, 2006), which is the case during initial stage of the LE problem. This causes an inverse dependence of the vertical velocity on the grid resolution (Fringer et al., 2006; Ilicak et al., 2012). Under such conditions, one cannot expect the solutions to converge following the order of the numerical scheme, as is the case for classical convergence analysis, and the common idea that higher spatial resolution yields better results does not apply. Therefore, it is not possible to find a scaling to predict the optimal resolution *a priori* and the best modeling choices will vary for each particular case.

## 2.4 Upper ocean frontal instability for lateral stirring

### 2.4.1 Model configuration and parameters

In the MLI problem we use the Nek5000 results described in Özgökmen et al. (2011). The non-dimensional parameters in (2.1) were set to  $a = 20$ ,  $Fr = 0.1$ ,  $Ro = 0.02$ ,  $Re = 10^5$  and  $Pr = 7$ , and the reader is referred to Özgökmen et al. (2011) for further details on the Nek5000 configuration.

In ROMS, the model parameters and the physical conditions are set as close as possible to those in Nek5000. We use a simple rectangular box (Fig. 2.7), where the domain length is taken equal to its width ( $L = W = 10,000$  m) and the total water depth set consistent to the depth of a main thermocline ( $H = 500$  m). For this particular MLI study, the choice of tracer advection scheme is not critical. We conducted simulations (not shown) using U3H/C4V, MPDATA and U3H/Splines and no significant differences were observed in the results. Therefore, we chose to use the same scheme for both momentum and tracer and performed all the MLI simulations using U3H/C4V. The boundary conditions are periodic in the  $x$  direction and free-slip, closed wall, in the  $y$  direction.

The initial condition is:

$$\rho'(\mathbf{x}, 0) = [1 - 0.7 \times (1 - \frac{z}{H})^{2.3}] [1 - \exp\{-(\frac{y/L}{\lambda})^4 - (\frac{z}{0.2})^8\}] / 98, \quad (2.14)$$

where

$$\lambda = 0.5 + 0.05 \cos(2\pi \frac{x}{L}) + 0.006 \cos(2\pi \frac{x}{L/5}) + 0.003 \cos(2\pi \frac{x}{L/25}) \quad (2.15)$$

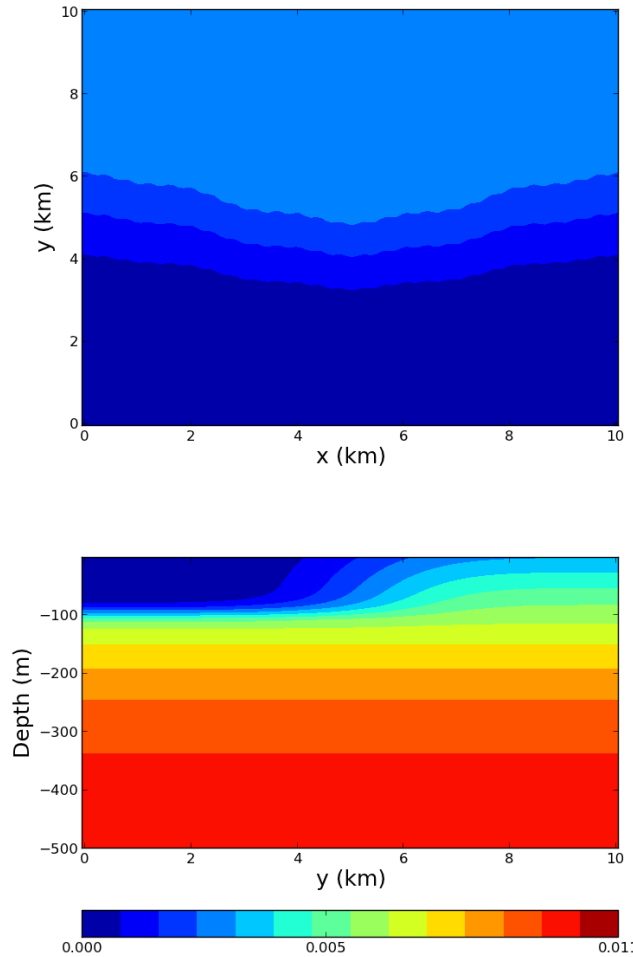


**Figure 2.7:** Initial condition for the MLI density perturbation field  $\rho'(\mathbf{x}, t = 0)$  ( $\text{kg m}^{-3}$ ), (top) surface horizontal section and (bottom) vertical cross section.

This profile represents a  $h_0 \approx 80$  m deep mixed-layer and an approximately 3 km wide front resting on a stably-stratified fluid (Fig. 2.7 bottom). This initial condition is similar to that in Özgökmen et al. (2011), but since ROMS uses dimensional variables, it has been scaled by 98 to keep the parameters described in the following section consistent with those from Nek5000. In addition, two smaller sinusoidal perturbations in (2.15) are included to facilitate the development of the desired instabilities. In the absence of these perturbations, the development of instabilities is

delayed by several days. The initial temperature condition is set by using the linear equation of state defined in (2.7) and the initial density perturbation field  $\rho'(\mathbf{x}, 0)$ , given in (2.14). The integrations start from rest and contain no forcing. Following Özgökmen et al. (2011), wind forcing is neglected for reasons of dynamical simplicity and to limit the parameter space.

From Fig. 2.7, the resultant buoyancy frequency is  $N \approx 4.42 \times 10^{-4} \text{ s}^{-1}$ . One of the challenges here is to estimate the flow speed scale ( $U_0$ ) that arises from the density field. From the numerical model results presented here, the maximum flow speed 4 hours after initialization is  $U_0 \approx 0.02 \text{ m s}^{-1}$ , which gives  $Fr = U_0/(NH) \approx 0.1$ . We set the Coriolis parameter as  $f = 1.21 \times 10^{-4} \text{ s}^{-1}$ , giving  $Ro = U_0/(fL) \approx 0.02$ .

For this MLI problem, the ratio between the fastest growing modes  $R$  and the mixed-layer radius of deformation  $R_d = \sqrt{\frac{g}{\rho_0} \Delta \rho'_m h_o}/f$  (where  $\Delta \rho'_m$  is the density difference across the surface front), over a wide regime of parameters, falls in a narrow range of  $4 \leq R/R_d \leq 6$  (Eldevik and Dysthe, 2002). Following Özgökmen et al. (2011), we assume  $R/R_d \approx 5$ . From Fig. 2.7,  $\Delta \rho'_m \approx 3.1 \times 10^{-3}$ , and we get  $R_d \approx 400 \text{ m}$ . Thus, the size of the horizontal mixing layer eddies is  $R \approx 2 \text{ km}$ . These parameters are consistent with the  $Fr = 0.1$  simulation presented by Özgökmen et al. (2011).

Three numbers of vertical levels ( $N_\sigma = 16, 32$  and  $64$ ) are used and in all cases the vertical S-coordinate is configured using (following the ROMS terminology): Vtransform = 1 (transformation equation); Vstretching = 1 (stretching function); theta\_s = 7 (surface stretching parameter); theta\_b = 0.1 (bottom stretching parameter); and tcline = 100 (critical depth, m). This configuration gives higher vertical resolution near the surface to better resolve the MLI's (Fig. 2.8).

Unlike in the LE case, in which stratified overturning and turbulent interactions play a key role in the overall mixing in the system, here our interest is on the turbulent exchange across the front by resolved MLI eddies.

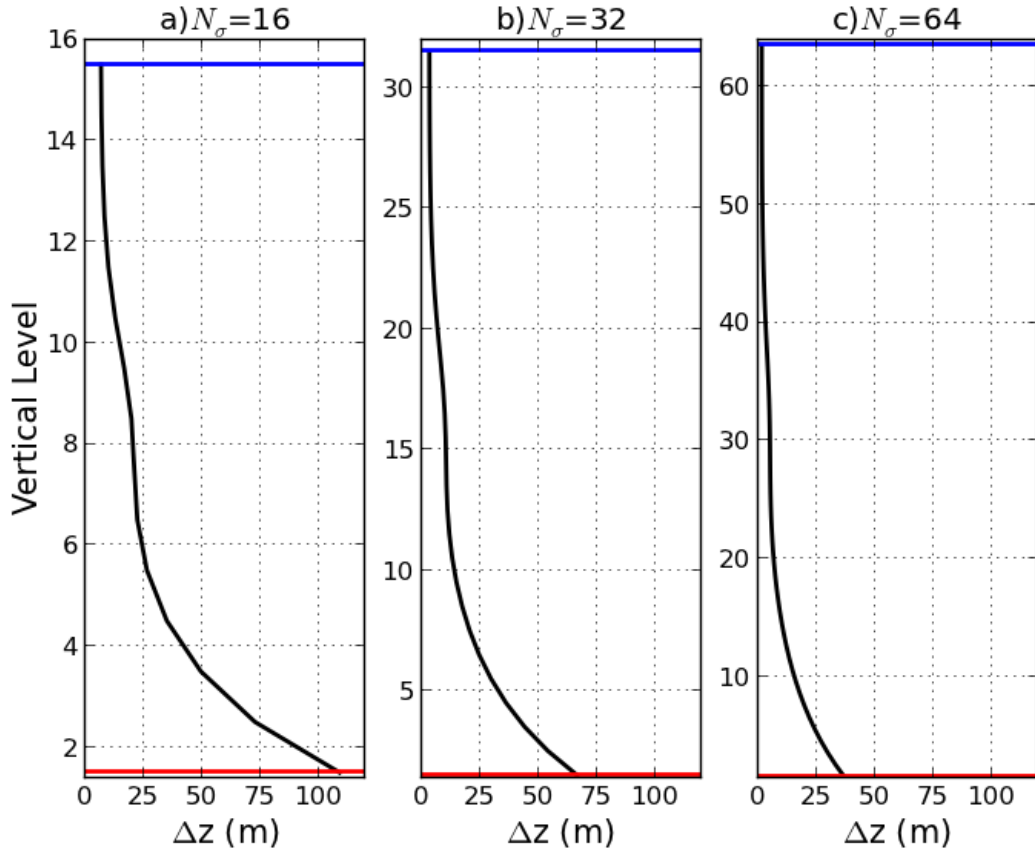


**Figure 2.8:** Layer thickness ( $\Delta z$ , m) as a function of vertical level for a)  $N_\sigma=16$ , b)  $N_\sigma=32$  and c)  $N_\sigma=64$ . The blue and red lines represent the surface and bottom layers, respectively.

## 2.4.2 Experimental description and tracer metrics

Table 4.2 presents the main parameters for the seven numerical experiments conducted in the MLI study. The simulation names are specified using the following logic (e.g., mli-100-32-k $\varepsilon$ ): type of problem - horizontal resolution (m) - number of vertical layers - turbulence closure or absence of vertical mixing (novmix).

In these experiments we vary horizontal and vertical resolutions, as well as apply the same turbulent closures presented in Section 2.3.2 ( $k-\varepsilon$ /CA and KPP-Ri). It should be noticed that the Richardson number-dependent KPP is designed to parameterize ocean mixing below the boundary layer (Large et al., 1994). Since there is no external forcing in our MLI experiments, the purpose of using KPP-Ri is to evaluate how the system evolves during, for example, the spin-down of a mixed-layer front created by the passage of a storm. The vertical background diffusivity ( $K_{CV}^0$ ) is set to the  $5.0 \times 10^{-3} \text{ m}^2 \text{ s}^{-1}$ , which is the value recommended by Large et al. (1994) based on the observed diffusivities reported for the seasonal thermocline (Peters et al., 1988). The vertical background viscosity ( $K_{MV}^0$ ) is set to  $3.5 \times 10^{-2} \text{ m}^2 \text{ s}^{-1}$ . In addition, we carry out a control experiment (mli-100-32-novmix), where both  $K_{CV}$  and  $K_{MV}$  are set to zero. These are some of the modeling choices that are faced during the implementation of an OGCM and, therefore, the outcomes will provide some guidance for applications focusing on the lateral dispersion of pollutants and biogeochemical tracers due to submesoscale MLI eddies.

The baroclinic time step is set to  $\Delta x/5$  seconds and the number of barotropic time steps between each baroclinic time step is set to 20. This yields a maximum lateral CFL number of  $9.9 \times 10^{-1}$  for all simulations. The approximate wall clock time as well as the number of nodes for each MLI experiment for an integration time of 30 days are summarized in Table 2.2.

One of the purposes of this study is to quantify the transport and mixing of a passive tracer field  $C(\mathbf{x})$  during the mixing layer adjustment. In ROMS, such a tracer field evolves in time following (2.6), where the horizontal and vertical diffusion coefficients are the same as those for temperature ( $K_{CH}$  and  $K_{CV}$ , respectively). The initial concentration of  $C(\mathbf{x})$  is specified as:

**Table 2.3:** List of MLI experiments conducted, where  $N_\sigma$  is the number of sigma levels,  $\Delta x = \Delta y$  is the horizontal grid spacing and CA = Canuto-A stability function. The minimum and maximum vertical grid spacing ( $\Delta z$ ) values are also shown.

Exp.	$\Delta x = \Delta y$ (m)	$N_\sigma$	min/max $\Delta z$ (m)	Turb. closure
mli-100-32-k $\varepsilon$	100	32	3.3/73.9	k- $\varepsilon$ /CA
mli-200-32-k $\varepsilon$	200	32	3.3/73.9	k- $\varepsilon$ /CA
mli-50-32-k $\varepsilon$	50	32	3.3/73.9	k- $\varepsilon$ /CA
mli-100-16-k $\varepsilon$	100	16	6.6/133.9	k- $\varepsilon$ /CA
mli-100-64-k $\varepsilon$	100	64	1.6/38.9	k- $\varepsilon$ /CA
mli-100-32-kpp	100	32	3.3/73.9	KPP-Ri
mli-100-32-novmix	100	32	3.3/73.9	none

$$C_0(\mathbf{x}) = \exp\left(-\frac{(y - y_c)^2}{l_y^2}\right) \exp\left(-\frac{z^2}{l_z^2}\right), \quad (2.16)$$

where  $y_c = 10,000$  m is at the center of the domain,  $l_y = 500$  m and  $l_z = 100$  m. A three-dimensional view of the initial concentration field  $C_0(\mathbf{x})$  is shown in Fig. 2.9. Although a release of this size might not be feasible in a field experiment, it ensures the tracer is well resolved in all the horizontal and vertical resolutions used in our numerical experiments. Using a more experimentally practical release could introduce numerical artifacts, since the initial patch of tracer would be near the limits of the model resolution. In all experiments presented here, the tracer is released 15 days after the beginning of the simulation, when the flow is fully non-linear (Fig. 2.10b).

To quantify the net turbulent expansion of the front by ML eddies, we compute the second moment (or tracer variance) of the tracer concentration field across the

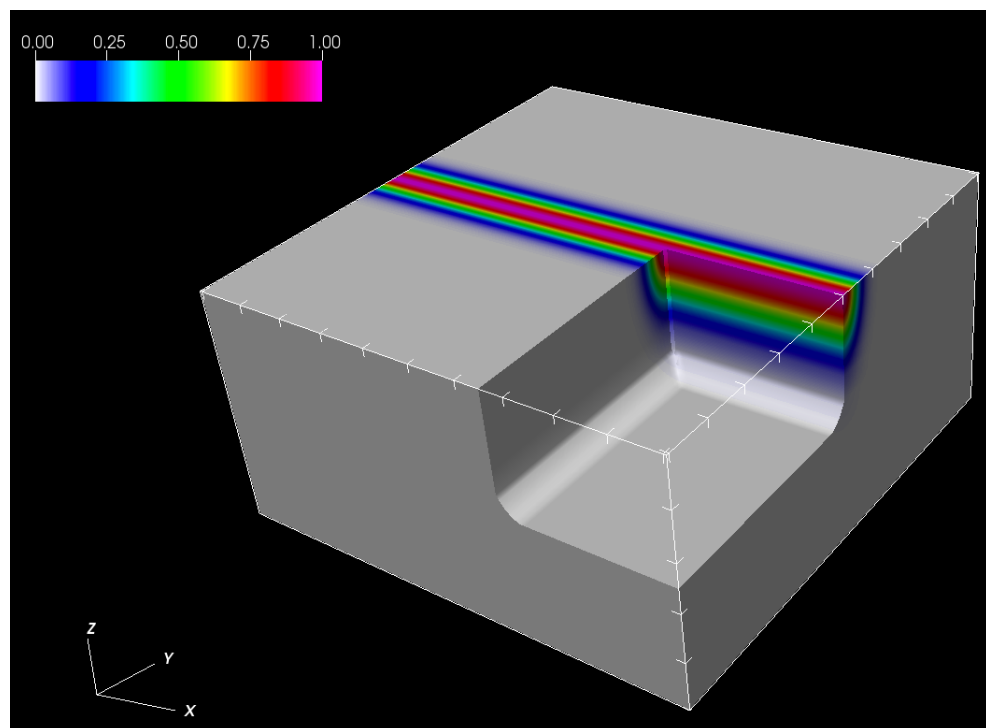


**Figure 2.9:** Three-dimensional view for the initial tracer concentration field  $C_0(\mathbf{x})$ . The color bar shows concentration in  $\text{kg m}^{-3}$ . Tick marks are placed every 1 km in the horizontal and 100 m in the vertical directions.

front and at a fixed level of  $z_0 \approx 5$  m,

$$\sigma_y^2(t, z_0) = \frac{M_{02}(t, z_0) - M_{01}^2(t, z_0)}{M_{00}(t, z_0)} \quad (2.17)$$

where

$$M_{mp}(t, z_0) = \frac{1}{A} \int \int x^m y^p C(x, y, z_0, t) dx dy. \quad (2.18)$$

The tracer variance is frequently employed in the analysis of observational data (Sundermeyer and Ledwell, 2001; Inall et al., 2013).

### 2.4.3 Description of the flow

Fig. 2.10 presents snapshots of the 3D density perturbation field  $\rho'$  for experiment mli-100-32-k $\varepsilon$  (see Table 4.2) at four different times. Initially (right after  $t=0$  days, not shown), inertial oscillations are created, where the vertical isopycnals start to oscillate around the geostrophically adjusted state, consistent with predictions by Tandon and Garrett (1994). As pointed by Boccaletti et al. (2007), there are no significant changes in stratification during this period. After a few days, MLIs are visible and restratification begins (Fig. 2.10a). After ten days (Fig. 2.10b), the presence of coherent vortices with scales consistent with  $R \approx 2$  km are clearly observed. Once the instability becomes fully nonlinear (Fig. 2.10c), the 3D density perturbation field is visually very similar to the LES simulation by Özgökmen et al. (2011) (see their Fig. 2b). At day 30 (Fig. 2.10d), the exchange flow associated with restratification gets close to the domain boundaries. Since the boundary induced shears and flows become important beyond this stage (not shown), we finalize the integration.

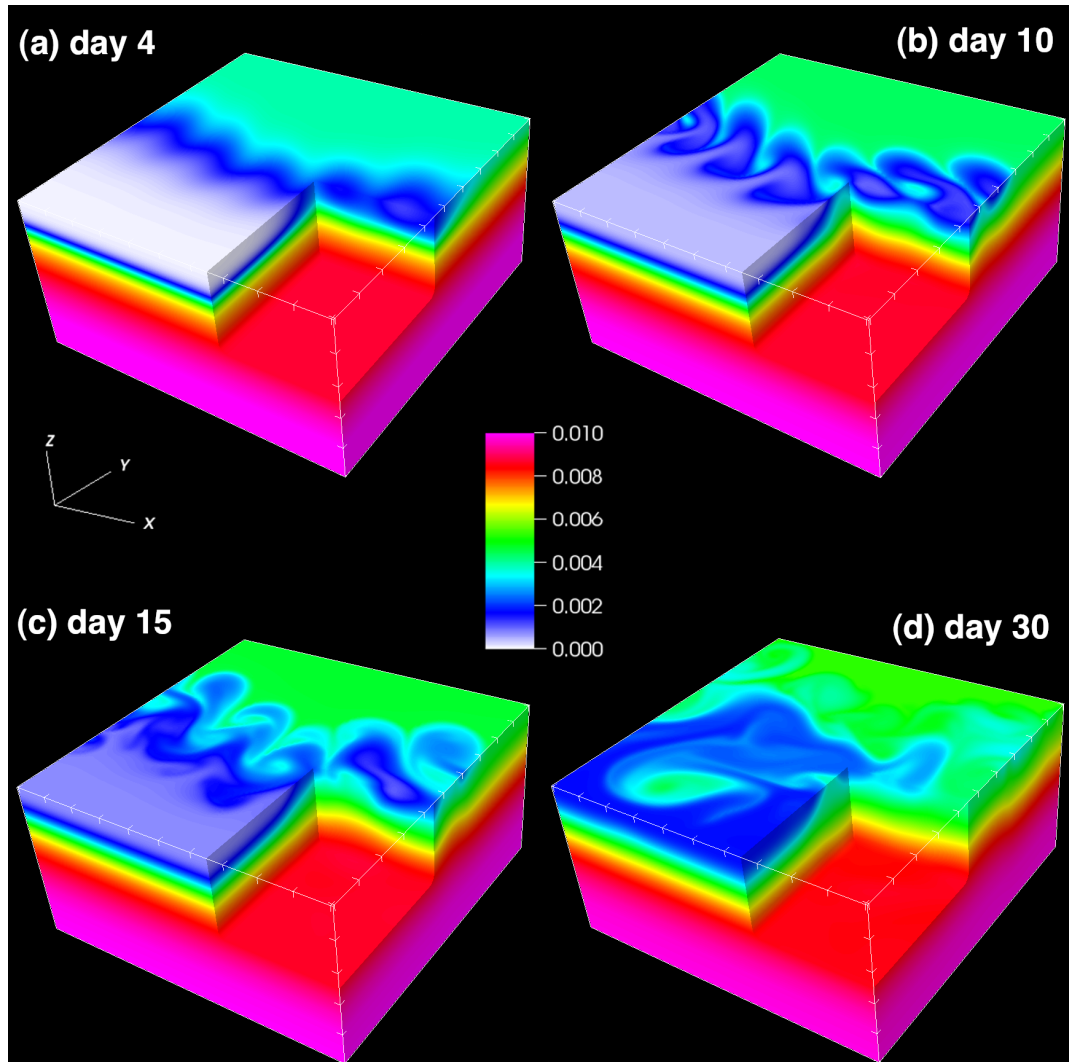


**Figure 2.10:** Density perturbation field  $\rho'$  ( $\text{kg m}^{-3}$ ) for experiment mli-res100-32A at a)  $t=4$  days, b)  $t=10$  days, c)  $t=15$  days and d)  $t=30$  days. The thick marks are placed every 1 km in the horizontal and 100 m in the vertical.

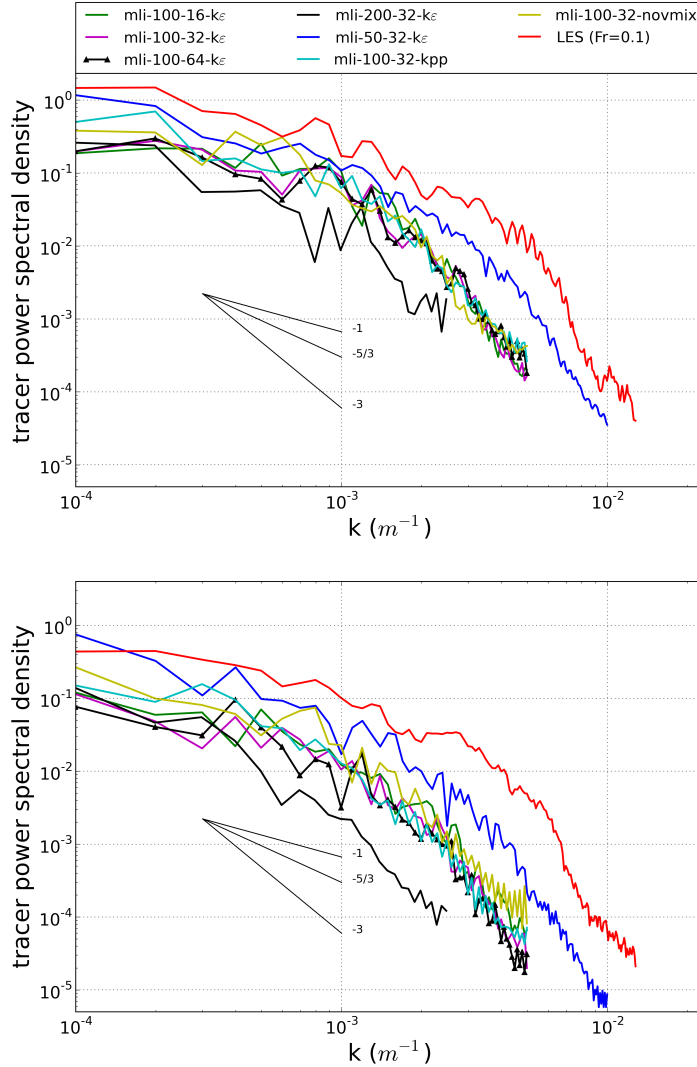


**Figure 2.11:** Tracer wave-number power spectral densities for experiments listed in Table 4.2 at (top) time = 18 days and (bottom) time = 21 days. The LES ( $Fr=0.1$ ) results by Özgökmen et al. (2009b) at corresponding times are also superimposed for comparison. Note the similarity between the spectra from experiments mli-100-32- $k\varepsilon$ , mli-100-16- $k\varepsilon$  and mli-100-64- $k\varepsilon$ ; and experiments mli-100-32-kpp and mli-100-32-novmix. Typical wave-number slopes are shown in the background.

#### 2.4.4 Comparison of lateral stirring from LES and ROMS

We now focus on the transport and stirring of a passive tracer field during the MLI adjustment process. In particular, we compute near surface wave-number spectra and the time evolution of the second moment of the tracer distribution.

To quantify the difference in tracer evolution from the experiments listed in Table 4.2, horizontal wave-number spectra of the near surface ( $\approx 5$  m) tracer fields are shown in Fig 2.11. These are computed by averaging over 20 one-dimensional spectra taken along the periodic direction  $4 \text{ km} \leq y \leq 6 \text{ km}$  at 3 and 6 days after the initial tracer release. At scales comparable to the mixing layer eddies ( $k \approx 5 \times 10^{-4} \text{ m}^{-1}$ ), most of the energy shown in the LES curve is well captured by the experiments with  $\Delta x = 50$  m. The ROMS spectra do not change significantly when either  $N_\sigma$  varies or the turbulence closure is changed (the spectra from experiments mli-100-32-k $\varepsilon$ , mli-100-16-k $\varepsilon$  and mli-100-64-k $\varepsilon$ ; and from experiments mli-100-32-kpp and mli-100-32-novmix are very similar). In tracer stirring carried out by approximately two-dimensional flow features a scaling of  $k^{-1}$  is expected (Vallis, 2006). The ROMS simulations display a more limited range of  $k^{-1}$  scaling, while the LES curves are approximately consistent with this slope down to  $k \approx 5 \times 10^{-2} \text{ m}^{-1}$ . The energy spectrum from the ROMS experiments become more similar to the LES curve as horizontal resolution is increased.

The time evolution of the tracer variances in the near surface are presented in Fig. 2.12. The results are shown until day 21, since in our control experiment (mli-100-32-novmix) boundary induced shears and flows become important beyond this point (not shown). This metric suggests that the ROMS experiments are not significantly affected, compared to other modeling choices tested here, when either  $N_\sigma$  or  $\Delta x$  are varied. Better agreement with the LES results is obtained using the second order closure model (k- $\varepsilon$ /CA) at all resolutions used. The curve from experiment mli-100-

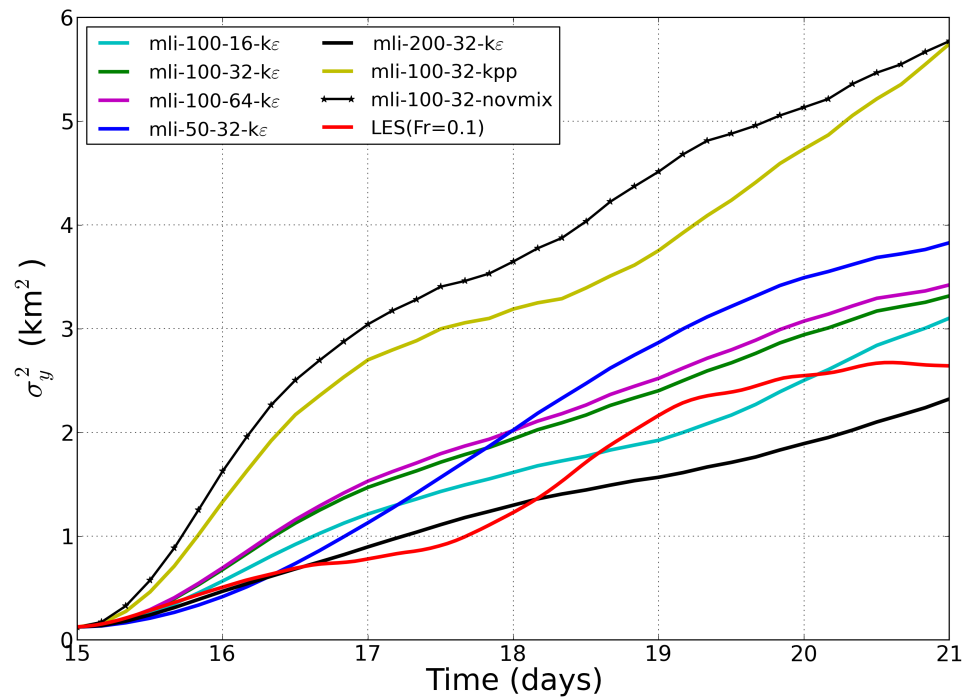


**Figure 2.12:** Second moment of the tracer distribution as a function of time for the MLI experiments listed in Table 4.2. The curves from experiments mli-100-32-kpp and mli-100-32-novmix are very similar. The LES ( $Fr=0.1$ ) curve presented in Özgökmen et al. (2011) is also superimposed for comparison.

32-kpp resembles again our control run and significant deterioration of the solution is found in these experiments (see Section 2.4.5 for more details).

From the curves presented in Fig. 2.12, the  $y$ -component of diffusivity can be obtained following:

$$K_y = \frac{1}{2} \frac{\partial \sigma_y^2}{\partial t}. \quad (2.19)$$

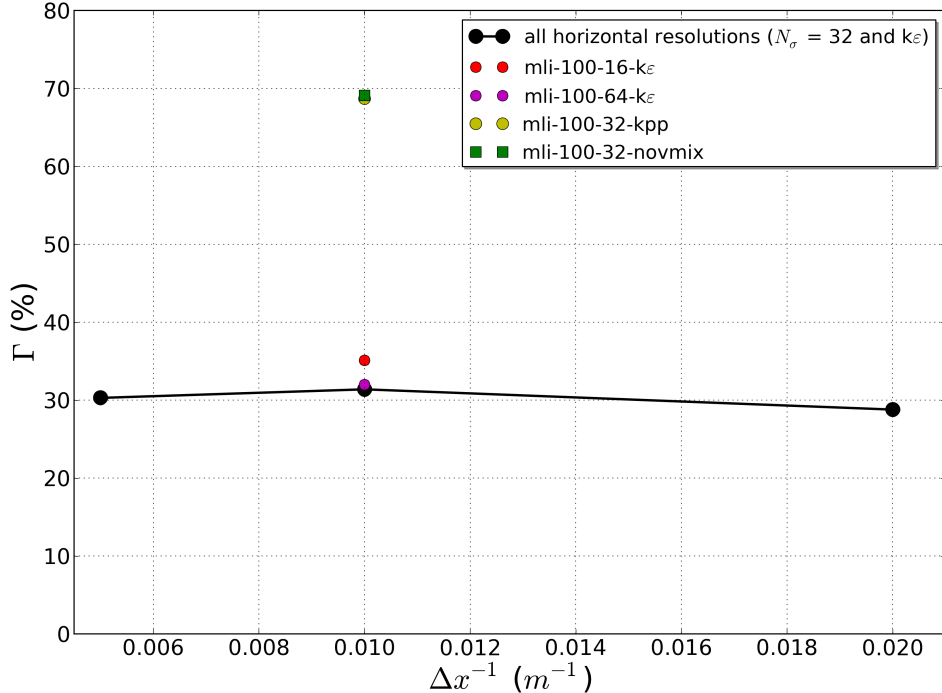


**Figure 2.13:** Normalized root-mean-square errors computed from the  $y$ -direction horizontal diffusivities  $\langle K_y \rangle$  ( $\Gamma$ , defined by Eq. 2.13; see text for details) as a function of the inverse grid resolution ( $\Delta x^{-1}$ ,  $m^{-1}$ ) for all MLI experiments presented in Table 4.2. Note the overlap between points from experiments mli-100-32- $k\epsilon$  and mli-100-64- $k\epsilon$ ; and mli-100-32-kpp and mli-100-32-novmix

We compute  $K_y$  using a 6-hour interval and then calculate the normalized root-mean-square error ( $\Gamma$ , defined in Eq. 2.13) with respect to the LES diffusivity. This interval is arbitrarily chosen and, qualitatively, the results described below are not sensitive to the time interval used (we tested values ranging from 2 to 24 hours). In

the ROMS experiments, the time-averaged  $y$ -direction horizontal diffusivities  $\langle K_y \rangle$  range from  $2.1$  to  $5.5 \text{ m}^2 \text{ s}^{-1}$ , while for the LES experiment the value is  $2.0 \text{ m}^2 \text{ s}^{-1}$ . These values are all within the limits observed over the continental shelf and below the mixed layer on spatial scales of  $1\text{-}10 \text{ km}$  and timescales of less than  $5 \text{ days}$  (Sundermeyer and Ledwell, 2001; Inall et al., 2013). However, we highlight that in nature the problem is considerably more complex than our idealized case and other processes, such as those associated with external forcing, inertial waves or mean flow, may also influence the lateral dispersion of a dye patch. Therefore, it would be difficult to evaluate our results by relying just on the observations. Fig. 2.13 shows the values of  $\Gamma$  computed for each ROMS simulation. Again, the results are not significantly sensitive to either  $N_\sigma$  or the  $\Delta x$  values tested here. The error for  $\Delta x = 100 \text{ m}$  is the largest (experiment mli-100-32-k $\varepsilon$ ,  $\Gamma=31.4 \%$ ). A small improvement in the solution is achieved if coarser ( $\Delta x = 200 \text{ m}$ ) or higher ( $\Delta x = 50 \text{ m}$ ) horizontal resolutions are used (experiments mli-200-32-k $\varepsilon$  and mli-50-32-k $\varepsilon$ ,  $\Gamma = 30.3 \%$  and  $28.8 \%$ , respectively). The result from an additional experiment (not shown) with  $\Delta x = 25 \text{ m}$  also shows a small improvement in the solution ( $\Gamma = 26.1 \%$ ), but the increase in computing time (wall clock time is  $\sim 2$  times larger than in experiment mli-50-32-k $\varepsilon$ , see Table 2.2) does not justify such gain. Additionally, the results do not converge as the vertical resolution is increased and the best solution is achieved when using an intermediate number of sigma layers ( $N_\sigma = 32$ ). Nonetheless, we highlight that the differences in  $\Gamma$  as horizontal and vertical resolution vary are significantly reduced when compared to those obtained in the LE problem (see Section 2.3.4). Unlike the latter, the hydrostatic approximation holds for the MLI problem (since  $Fr^2 a^{-2} \ll 1$ ). However, our results are not sufficient to make a connection between better spatial convergence and the fact that the hydrostatic approximation holds and further studies should be conducted to address this point.

Finally, the largest errors obtained are related to the choice of turbulence closure. The use of KPP-Ri results in a much larger error (mli-100-32-kpp,  $\Gamma = 68.7\%$ ) compared with  $k-\varepsilon$ /CA (mli-100-32- $k\varepsilon$ ,  $\Gamma = 31.4\%$ ) when using identical horizontal and vertical resolutions. Similarly, the error in the control experiment (mli-100-32-novmix,  $\Gamma = 69.1\%$ ) is significantly larger, suggesting that the turbulence closure has a significant contribution in the stirring of a passive tracer during the MLI adjustment. This point is explored in more detail in the following section.

#### 2.4.5 Restratification and vertical diffusivity

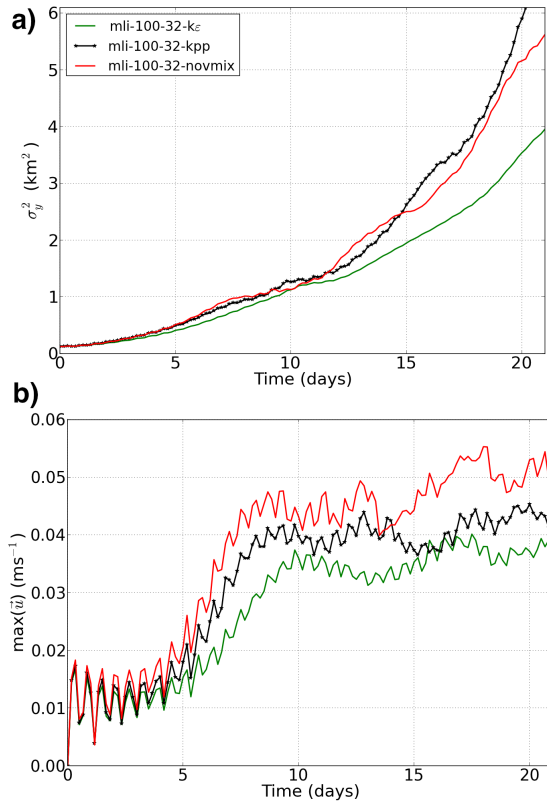


**Figure 2.14:** Time series of (a) near surface tracer second moment ( $\sigma_y^2$ ,  $\text{km}^2$ ) and (b) maximum horizontal velocity ( $\vec{u}$ ,  $\text{m s}^{-1}$ ) in the mixed layer. Results from experiments mli-100-32- $k\varepsilon$ , mli-100-32-kpp and mli-100-32-novmix are shown.

We now focus on experiments mli-100-32-k $\varepsilon$ , mli-100-32-kpp and mli-100-32-novmix and following equation (2.16) release a passive tracer field at the beginning of the simulation (time = 0 days). The corresponding time evolution of  $\sigma_y^2$  in the near surface are presented in Fig. 2.14a. Experiments mli-100-32-kpp and mli-100-32-novmix show larger values of tracer variance throughout the simulation in comparison to mli-100-32-k $\varepsilon$ . The discrepancy is amplified after day 12. It is instructive to compute a metric for the restratification due to the rearrangement of buoyancy by the residual circulation. We compute an overturning eddy streamfunction ( $\psi_e$ ) as follows:

$$\psi_e = \alpha \left( \frac{\alpha \overline{v'b'} \overline{b_z} - \alpha^{-1} \overline{w'b'} \overline{b_y}}{\overline{b_y}^2 + \alpha^2 \overline{b_z}^2} \right), \quad (2.20)$$

where  $b$  is the buoyancy, primes are fluctuations from the mean value (averaged along  $x$  direction and denoted by an overbar) and subscript denotes partial derivatives. This form of  $\psi_e$  (Plumb and Ferrari, 2005; Cerovečki et al., 2009; Mahadevan et al., 2010; Ramachandran et al., 2013) generalizes earlier definitions and remains well defined in situations where  $\overline{b_y}$  or  $\overline{b_z}$  become negligibly small (e.g., weakly stratified environments, like the MLI problem applied here). A coordinate stretching parameter  $\alpha = H/L = 0.05$  is used to account for the skewed aspect ratio. Our results are insensitive to  $\alpha$  over a range  $10^{-2} - 10^{-3}$ . The eddy streamfunction always shows a thermally directed circulation, where warm (light) water rises above cold (dense) water. Snapshots of  $\psi_e$  at day 7 are shown in Fig. 2.15. At this stage, the strength of the secondary circulation is significantly larger in experiments mli-100-32-kpp and mli-100-32-novmix when compared to the case with k- $\varepsilon$ /CA. This is because MLI have grown slower in the latter, as shown by the time series of  $\sigma_y^2$  and maximum horizontal velocity within the ML (Figs. 2.14a and b, respectively). As expected, the discrepancy between experiments with different turbulence closures are due to the

values of the explicit vertical diffusivity (and viscosity, not shown), which are zero in our control case and significantly larger in the case using  $k-\varepsilon/CA$  when compared to the case using KPP-Ri (Fig. 2.16). We emphasize that the Richardson number-dependent KPP parameterization was not designed to work in the mixed layer and, therefore, it is not surprising that this scheme underestimates the amount of vertical viscosity and diffusivity during the MLI adjustment.

Ramachandran et al. (2013) studied the effect of subgrid-scale mixing in the evolution of the submesoscale instabilities generated in a mixed-layer front forced by downfront winds. Although they did not have a ground truth to compare their results with, they used the eddy kinetic budget to estimate physically meaningful levels for the SGS dissipation under quasi-equilibrium (restratification versus destratification) conditions. They found non-trivial variability in the amount of dissipation when varying the vertical viscosity in the simulations (while keeping the lateral viscosity constant) and pointed out the need to explore the sensitivity of submesoscale-resolving simulations to the vertical SGS parameterization. Here this sensitivity has been explored and we highlight the importance of adopting a turbulence closure that is able to provide (even in the absence of external forcing) additional viscosity/diffusivity in the mixed-layer, where entrainment is critical.

## 2.5 Summary and conclusions

This study is motivated by some of the questions that every modeler faces when setting up a problem: what are the most appropriate resolutions, parameters, numerical schemes and turbulence models and how do they affect the solution space? Preferably, such studies should involve oceanic data sets for direct relevance. Nevertheless, in problems involving mixing and stirring, ocean observations can be sparse or incorporate aliasing errors due to the time needed for sampling. In addition, the forcing

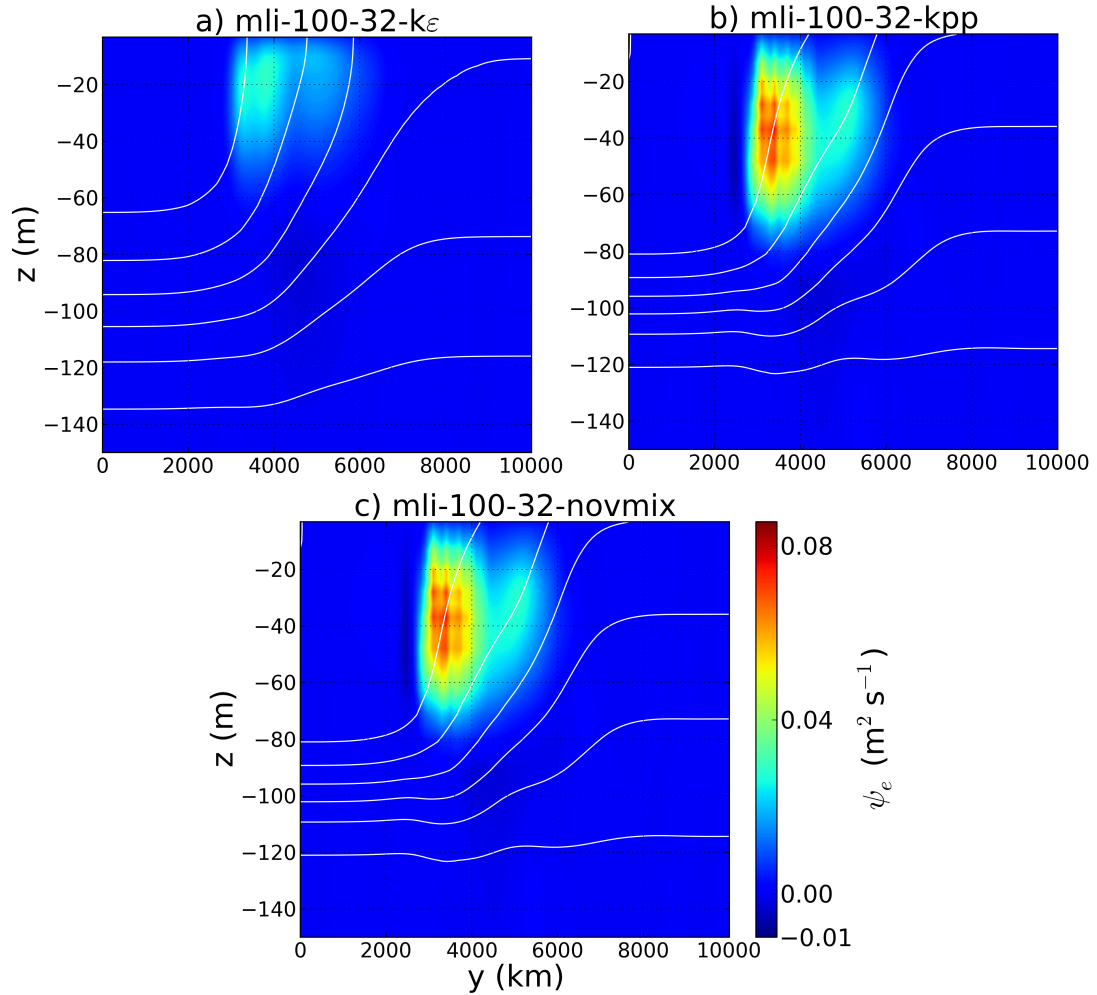


**Figure 2.15:** Eddy streamfunction ( $\psi_e$ ,  $\text{m}^2 \text{s}^{-1}$ ) at day 7 for experiments (a) mli-100-32-k $\varepsilon$ , (b) mli-100-32-kpp and (c) mli-100-32-novmix. White lines show buoyancy contours.

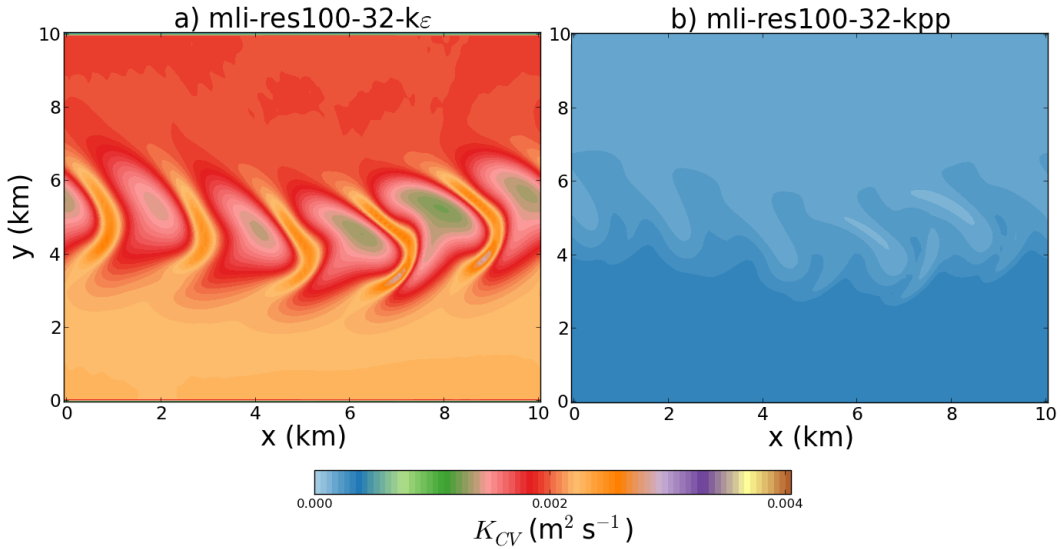


**Figure 2.16:** Snapshots of vertical diffusivities ( $K_{CV}$ ,  $\text{m}^2 \text{ s}^{-1}$ ) at  $\sim 40$  m depth after 7 days of simulations from runs using a) the second order turbulence closure  $k-\varepsilon/\text{CA}$  (experiment mli-100-32-k $\varepsilon$ ) and b) the algebraic Richardson number based KPP (experiment mli-100-32-kpp).

fields that influence the solution might not always be available. There are many examples of studies that have conducted a direct comparison of numerical solutions with observations (Özgökmen et al., 2003; Xu et al., 2006; Ilicak et al., 2008; Chang et al., 2008; Ilicak et al., 2009), and in all of which the precision of comparison was effectively limited by the extent of the observational data set.

Two numerical approaches, LES and OGCM, have recently started to address similar problems in oceanography (i.e., submesoscale motions due to mixed layer instabilities). The LES approach has the full non-hydrostatic dynamics and a more complete way of capturing mixing and stirring (at the expense of computational time), while OGCMs have the full range of functionalities that make the results directly relevant for oceanic applications. However, the LES approach is usually limited in terms of realistic forcing and boundary conditions that drive the flow, whilst in OGCMs mixing and stirring are usually dependent on parameterizations.

As such, a clear avenue for gaining more insight into the accuracy of OGCMs solutions for mixing and stirring problems is using LES as reference, provided that idealized yet oceanographically-relevant problems can be set up.

In this study a series of numerical simulations were conducted for two idealized cases, namely the lock-exchange (LE) and the mixed-layer instability (MLI) problems. Our main goal is to compare mixing and stirring derived from two modeling approaches: an OGCM (ROMS) that solves the hydrostatic primitive equations, and a spectral element model (Nek5000) that integrates the non-hydrostatic Boussinesq equations. Although comparing these two different modeling approaches is not a trivial task, given that the former is configured in terms of dimensional variables while non-dimensional variables are used in the latter, it is a valuable way of testing the accuracy of OGCMs when the scales fall below the mesoscale regime. ROMS is a hydrostatic ocean model formulated in a terrain-following vertical coordinate. Therefore, the results presented here should be fairly general to other OGCMs that follow these characteristics. In addition, the results related to the choice of turbulence closure can be generalized to other OGCMs that contain the closures tested here.

In the first part of this chapter we apply the LE problem to compare the temporal evolution of mixing under various OGCM modeling choices. As a metric we use the background potential energy (BPE), which quantifies mixing in an enclosed system (Winters et al., 1995). The numerical experiments are configured as similarly as possible to the LES settings, which is used as reference. We explore the effects of various modeling parameters and find that, for a fixed horizontal Reynolds number ( $Re_H = 10^3$ ), mixing is most sensitive to the choice of grid resolution. We show that the choice of turbulence closure plays a minor role in the temporal evolution of mixing for the LE problem. No convergence towards the ground truth reference (LES) is attained as the grid resolution is refined and the best results are achieved using an

intermediate spatial resolution (2.5 m). Mixing is underestimated when using a higher grid resolution (1.25 m) and it is overestimated when using coarser grid resolutions (5 and 10 m). Mixing is also better represented at lower  $Re_H$  ( $10^3$ ), since even with our finest grid resolution ( $\Delta x = 1.25$  m) the implicit numerical diffusion associated with the advection scheme does not allow the effective  $Re_H$  to be increased to  $10^4$ . The choice of tracer advection scheme also has an important influence on the mixing. Our results show that the combination formed by U3H/C4V schemes results in excessive mixing (and lack of monotonicity in the BPE), with larger deviation from the LES results when compared to MPDATA. We show the importance of using a monotonic scheme in numerical studies dealing with small-scale stratified mixing, where the initial tracer extrema must be preserved. This outcome is particularly relevant for the studies described in the chapters that follow.

The sensitivity of the transport and stirring of a passive tracer field is then studied within the context of the MLI problem. Our simulations are configured as similarly as possible to the LES ( $Fr = 0.1$  case) presented by Özgökmen et al. (2011), which is treated as our ground truth. As a metric, we compute near surface tracer energy spectra and the time evolution of the second moment (or tracer variance), from which the cross-frontal diffusivity is obtained. A total of seven numerical experiments are carried out, where common modeling choices related to horizontal/vertical resolutions as well as turbulence closure are explored. The results do not converge towards the ground truth reference (LES) as the horizontal and vertical grid resolutions are refined. The best solution is achieved when using an intermediate number of sigma layers ( $N_\sigma = 32$ ) and a horizontal grid resolution of  $\Delta x = 50$  m. However, it is likely that the results have already converged with the coarsest spacial resolution tested here ( $N_\sigma = 32$  and  $\Delta x = 200$  m) and the small differences due to different spatial resolutions are due to numerical artifacts. Varying the amount of vertical viscosity

and diffusivity (by selecting different turbulence closures) shows more impact on the stirring of a passive tracer field than any other modeling choice investigated here. The best results with respect to the LES run are achieved with  $k-\varepsilon/CA$  and the deviation increases by a factor of approximately two when KPP-Ri is selected. We show that this discrepancy is due to the low values of vertical viscosity/diffusivity given by KPP-Ri and highlight the importance of adopting a turbulence closure that is able to provide (even in the absence of external forcing) additional viscosity/diffusivity in the mixed-layer, where entrainment is critical.

### Acknowledgments

The contents of this chapter have been published in Ocean Modelling, 2014, coauthored by Professor Tamay Özgökmen. We greatly appreciate the support of the Office of Naval Research and National Science Foundation via grants N00014-09-1-0267 and OCE-0961369, respectively. This research was made possible, in part, by a grant from BP/The Gulf of Mexico Research Initiative. The LES computations were supported by a grant of computer time from the City University of New York High Performance Computing Center under NSF Grants CNS-0855217 and CNS - 0958379. We also thank University of Miami's Center for Computational Science for making available their resources. The authors appreciate many helpful discussions with Prof. Mohamed Iskandarani and Jean M. Mensa.

# Chapter 3

## Topographic vorticity waves forced by Antarctic dense shelf water outflows

This chapter is motivated by numerical (Wang et al., 2009) and observational (Darelius et al., 2009; Jensen et al., 2013) evidences of subinertial, quasi-periodic oscillations in water properties along the upper continental slope in the southern Weddell. Jensen et al. (2013) have recently shown that the properties of these oscillations are consistent with mode-1 coastal trapped waves, here referred as topographic vorticity waves (TVWs). These authors hypothesized that the TVWs they observed in the southern Weddell Sea were generated by the release of DSW from the Filchner Trough but did not confirm it. We use a combination of idealized and realistic numerical simulations to investigate the generation of topographic vorticity waves by Antarctic dense shelf water outflows through troughs. We also investigate how the dispersion properties of these waves depend on bottom slope, outflow density anomaly, and background along-slope flow representing the Antarctic Shelf Current.

### 3.1 Numerical simulations

We use an idealized model of density outflows and a realistic, atmospherically forced model of the Ross Sea. Both models are based on the Regional Ocean Modeling System (ROMS) (Shchepetkin and McWilliams, 2005). ROMS has been widely used, including applications to overflow-related studies (e.g., Ilicak et al., 2008; Padman et al., 2009).

#### 3.1.1 Idealized model of TVW generation by outflows

The model domain ( $600 \times 300$  km) is a flat continental shelf with depth  $H_0$ , a continental slope  $\alpha$ , and a flat abyssal ocean that is  $H_0+1500$  m deep (Figure 3.1a). The slope is located at latitude  $72^\circ\text{S}$ , corresponding to the Drygalski Trough outflow in the northwest Ross Sea (Padman et al., 2009; Gordon et al., 2009). A half-cosine-shaped canyon, whose axis is centered  $\sim 200$  km from the eastern wall, cuts across the shelf with a maximum depth of  $H_0+200$  m and width of  $\sim 50$  km. The horizontal grid spacing ( $\Delta x$ ) is set to either 3 km or 1 km (see Table 3.2), with the finer spacing needed to resolve the slope when  $\alpha=0.1$ . In the vertical direction, all experiments were discretized using 41 topography-following levels. To do so, the default transformation ( $\text{Vtransform} = 2$ ) and vertical stretching ( $\text{Vstretching} = 4$ ) functions available in ROMS were used. The control parameters (Table 3.1) were set to maximize the vertical resolution near the bottom, while still keeping both the maximum topographic stiffness ratio proposed by Beckmann and Haidvogel (1993) (referred to as “rx0” in the ROMS documentation) and the maximum modified form of the “Haney” condition (referred to as “rx1” in the ROMS documentation; Haney, 1991) below accepted limits. The critical depth was set as  $\text{TCLINE} = 200$  m. An example of layer thickness ( $\Delta z$ ) as a function of vertical level at four different water depths taken from Exp.#01 along  $x = 0$  km is shown in Figure 3.2.

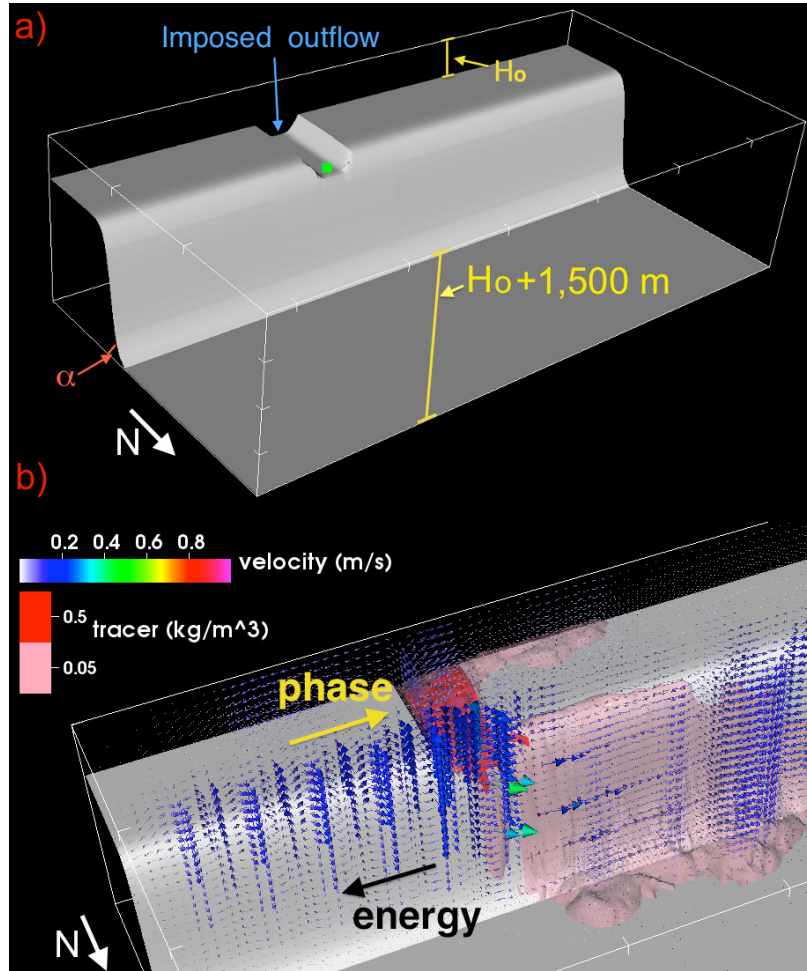


**Figure 3.1:** a) 3D view of the domain for the idealized model. Green point shows the location where  $\Gamma$  values are computed. Thick marks are placed every 100 km in the horizontal and 500 m in the vertical directions. b) Partial view of the idealized domain for the control experiment (Exp.#01, see Table 3.2) at model time  $t=78$  days, showing wave-like velocity structures east of the trough. The phase and energy directions, and two contours of tracer concentration (0.5 and 0.05) are also shown.

The horizontal momentum is discretized with a third-order, upstream-biased advection scheme with velocity-dependent hyper-viscosity (Shchepetkin and McWilliams, 1998). This scheme allows the generation of steep gradients in the solution, enhancing the effective resolution of the solution for a given grid size when the explicit vis-

**Table 3.1:** Vertical s-coordinate parameters and diagnostics (maximum rx0 and rx1) for the different experiments conducted in this study.

Exp. #	$\theta_s$	$\theta_b$	rx0	rx1
01	2.5	1.7	0.03	6.9
02	2.5	1.7	0.03	6.9
03	1.0	3.4	0.09	7.0
04	1.0	1.9	0.07	6.8
05	2.5	3.0	0.07	6.9
06	2.5	1.4	0.13	6.9
07	2.5	1.7	0.08	5.6
08	2.5	1.7	0.03	6.9
09	1.5	3.5	0.04	7.1
10	2.5	1.7	0.08	5.6
11	1.0	1.3	0.09	6.9
12	2.5	1.7	0.03	6.9
13	2.5	1.7	0.03	6.9
14	2.5	1.7	0.03	6.9

cosity is small (Shchepetkin and McWilliams, 1998). For the vertical momentum, a fourth-order centered differences scheme is used. Tracers are advected using the multi-dimensional positive-definite advection transport algorithm (MPDATA). This scheme preserves the positive-definite characteristics of the tracers, which avoids under- and over-shooting of the initial tracer values. As shown in Chapter 2, this property is essential to avoid unphysical behavior in terms of mixing. The baroclinic time step is set to 180 seconds for simulations with  $\Delta x = 3$  km and 60 seconds for simulations with  $\Delta x = 1$  km. The number of barotropic time steps between each baroclinic time step is set to 30.

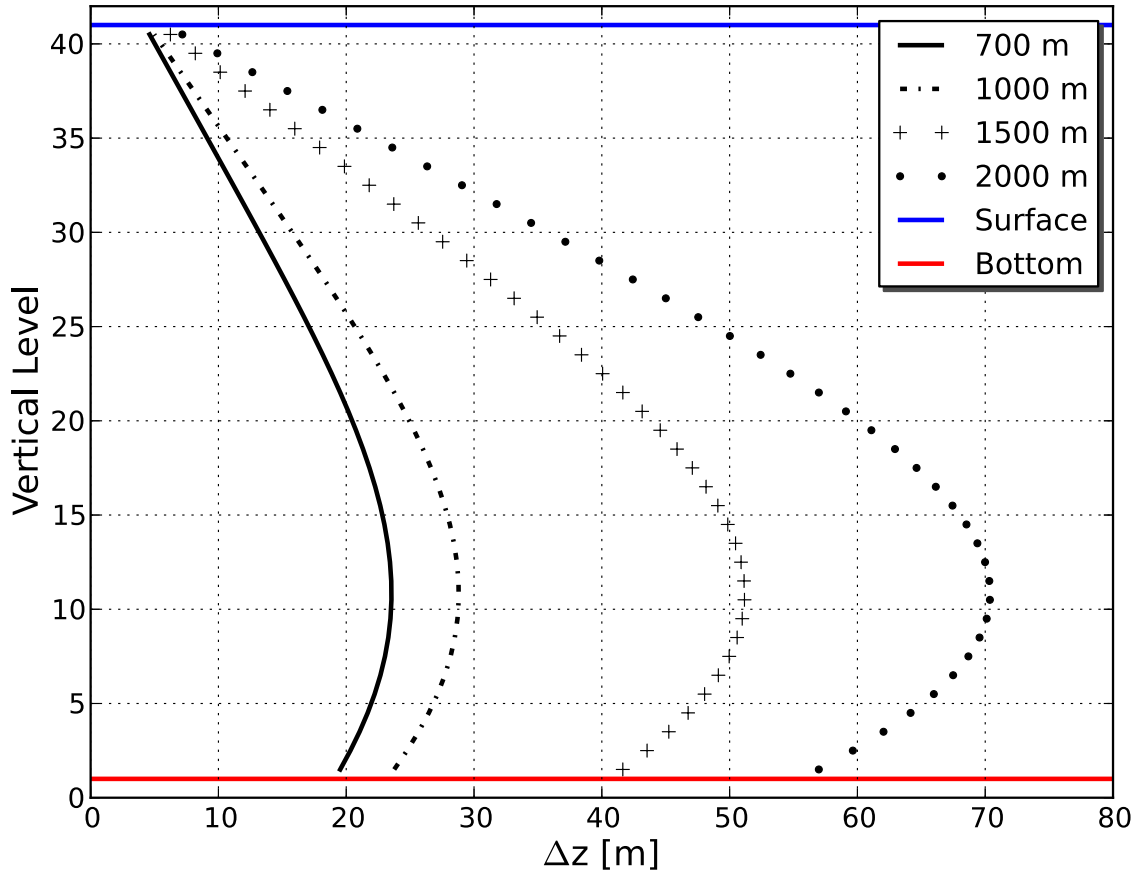


**Figure 3.2:** Layer thickness ( $\Delta z$ , m) as a function of vertical level (from bottom to surface) taken from Exp.#01 along  $x = 0$  km. Conditions at four different water depths are shown: 700 m (shelf break), 1000 m (mid-slope), 1500 m (lower slope) and 2000 m (deep ocean).

Vertical mixing is parameterized by the two-equation standard  $k-\varepsilon$  turbulence closure (Burchard and Baumert, 1995b) with Canuto-A stability function (Canuto et al., 2001). This selection was based on evaluations of turbulence closures in three-dimensional simulations of the Red Sea overflow (Ilicak et al., 2008) and on the results presented in Chapter 2. We use a Laplacian formulation for the horizontal mixing of momentum and tracers. Both the explicit horizontal viscosity ( $\nu_H$ ) and diffusivity ( $\kappa_H$ ) are set to zero in all runs, since the applied advection schemes are naturally

dissipative. Bottom stress is modeled using a quadratic function with drag coefficient  $c_d = 0.003$ , consistent with a previous numerical studies of the Drygalski Trough overflow (Padman et al., 2009).

We carried out a set of 14 simulations (Table 3.2), varying  $\alpha$ ,  $H_0$ ,  $\Delta\rho$ ,  $\Delta x$  and maximum along-slope barotropic velocity ( $U_{max}$ , representing the ASC) over ranges representing typical observed values in the Weddell and Ross seas (Jacobs, 1991; Heywood et al., 1998; Foldvik et al., 2004; Muench et al., 2009a). In our control run (Exp.#01), the main parameters were set as follows:  $\Delta x=3$  km,  $\alpha=0.05$ ,  $H_0=500$  m,  $U_{max}=0$  m s $^{-1}$  and  $\Delta\rho=0.24$  kg m $^{-3}$ . Boundary conditions were similar to those used in previous idealized simulations of overflows (Legg et al., 2006; Ilicak et al., 2011). In the western, eastern and northern boundaries, Flather and Chapman boundary conditions are used for depth-averaged velocities and free surface, respectively. In addition, radiation conditions for tracers and three-dimensional velocities are also applied. The boundary conditions in the southern wall are closed and no slip, except where the trough intersects the wall (see Figure 3.1). At the eastern and western sides, all variables are gradually relaxed towards the initial conditions within nudging zones that are 30 km wide. These are also sponge zones, where horizontal viscosity was enhanced to 500 m $^2$ s $^{-1}$ . The relaxation timescale  $\tau$  is linearly varied from 1 day at the boundary to 60 days towards the interior of the domain. Most simulations were started from rest, except those in which  $U_{max} \neq 0$ . In the latter, the initial conditions (sea surface elevation and along-slope velocity) were set in geostrophic balance such that  $U_{max}$  occurred at the shelf break and exponentially decayed within 10 km to the north and south. The ambient water in all runs was initially homogeneous, with temperature and salinity values set to 0.95°C and 32.5, respectively. Dense water was injected in the trough at the southern wall. A passive tracer with initial concentration  $\tau = 1$  was injected with the dense water and then used to track the bottom plume.

**Table 3.2:** List of numerical experiments conducted. Values of  $c_p < 0$  and  $c_g < 0$  indicate westward along-slope phase and energy propagation, respectively.

Exp. #	$\Delta x$ (km)	$\alpha$	$H_0$ (m)	$\Delta\rho$ ( $\text{kg m}^{-3}$ )	$U_{max}$ ( $\text{m s}^{-1}$ )	$\Gamma_{min.}$	$\Gamma_{max.}$	$\Gamma_{av.}$	$\omega$	$\lambda$	$c_p$ ( $\text{m s}^{-1}$ )	$c_g$ ( $\text{m s}^{-1}$ )
01	3	0.05	500	0.24	0	0.19	0.41	0.33	0.48	39	-0.22	0.13
02	3	0.05	500	0.12	0	0.11	0.28	0.23	0.41	33	-0.16	0.10
03	1	0.05	500	0.24	0	0.09	0.35	0.22	0.52	42	-0.25	0.14
04	1	0.10	500	0.24	0	0.66	0.87	0.77	0.65	32	-0.24	0.11
05	3	0.01	500	0.24	0	0.11	0.11	0.11	0.15	60	-0.10	0.06
06	3	0.05	250	0.24	0	0.38	0.81	0.62	0.58	33	-0.22	0.03
07	3	0.05	750	0.24	0	0.14	0.28	0.22	0.45	45	-0.24	0.12
08	3	0.05	500	0.18	0	0.23	0.39	0.31	0.48	36	-0.20	0.12
09	3	0.01	750	0.12	0	0.03	0.03	0.03	0.10	48	-0.06	0.04
10	3	0.05	750	0.12	0	0.04	0.19	0.14	0.39	36	-0.16	0.10
11	1	0.10	250	0.12	0	0.39	1.10	0.72	0.83	29	-0.28	0.12
12	3	0.05	500	0.24	-0.1	0.09	0.32	0.20	0.55	42	-0.27	0.06
13	3	0.05	500	0.24	-0.2	0.15	0.18	0.18	0.71	54	-0.44	0.03
14	3	0.05	500	0.24	-0.3	0.17	0.17	0.17	0.77	57	-0.51	-0.03

Since angular momentum is conserved, the stretching of overlying ambient water carried by the overflow is an important parameter controlling oscillations in the system. Following Lane-Serff and Baines (1998), we evaluated the stretching parameter  $\Gamma = R_d \alpha/D$ , where  $R_d = \sqrt{\Delta b_0 h_0}/f$  is the baroclinic radius of deformation (defined as in Legg et al., 2006),  $D$  is the depth of the ambient fluid above the bottom density current,  $\Delta b_0$  is the buoyancy anomaly,  $h_0$  is thickness of the bottom density current and  $f$  is the Coriolis parameter. We estimated time-varying values of  $\Gamma(t)$ , between model time  $t=70$  and 100 days, for a point at the northern end of the trough (for location, see Figure 3.1a). We computed  $\Gamma(t)$  every two hours and then removed the lowest and highest 10% of the values, so that the cited range of  $\Gamma$  includes 80% of the data during the 30-day analysis period. For our control run,  $\Gamma(t)$  varied between 0.19 and 0.41, with a time-averaged value ( $\Gamma_{av}$ ) of 0.33. For the other experiments,  $\Gamma_{av}$  values ranged from 0.03 to 0.77 (see Table 3.2). Time series of layer thickness ( $D$ , m) and density anomaly ( $\Delta\rho$ , kg m<sup>-3</sup>) used to compute the  $\Gamma$  values in Exp. #01 are shown in Figure 3.3 (top panel). It is clear that variations in  $\Gamma$  are controlled by both  $\Delta\rho$  and  $D$ . There is a negative correlation between  $D$  and  $\Delta\rho$ ; low values of  $\Delta\rho$  correspond to thin outflows (large  $D$ ), and are found when the northward cross-slope velocity is strong (Figure 3.3, bottom panel).

The wave properties in our simulations were estimated from time series of depth-averaged across-slope velocity extracted along a portion of the upper slope represented by the ( $H_0 + 400$ ) m isobath. Frequencies and wavelengths were estimated using a Fourier transform and correlation, respectively. We compared these wave properties with dispersion curves of inviscid coastal-trapped waves, obtained numerically by resonance iteration using the 2-D (depth versus across-slope direction) code developed by Brink (2006). We used 100 grid points in the across-slope direction and 30 grid points in the vertical direction. The topographic profiles were extracted from the

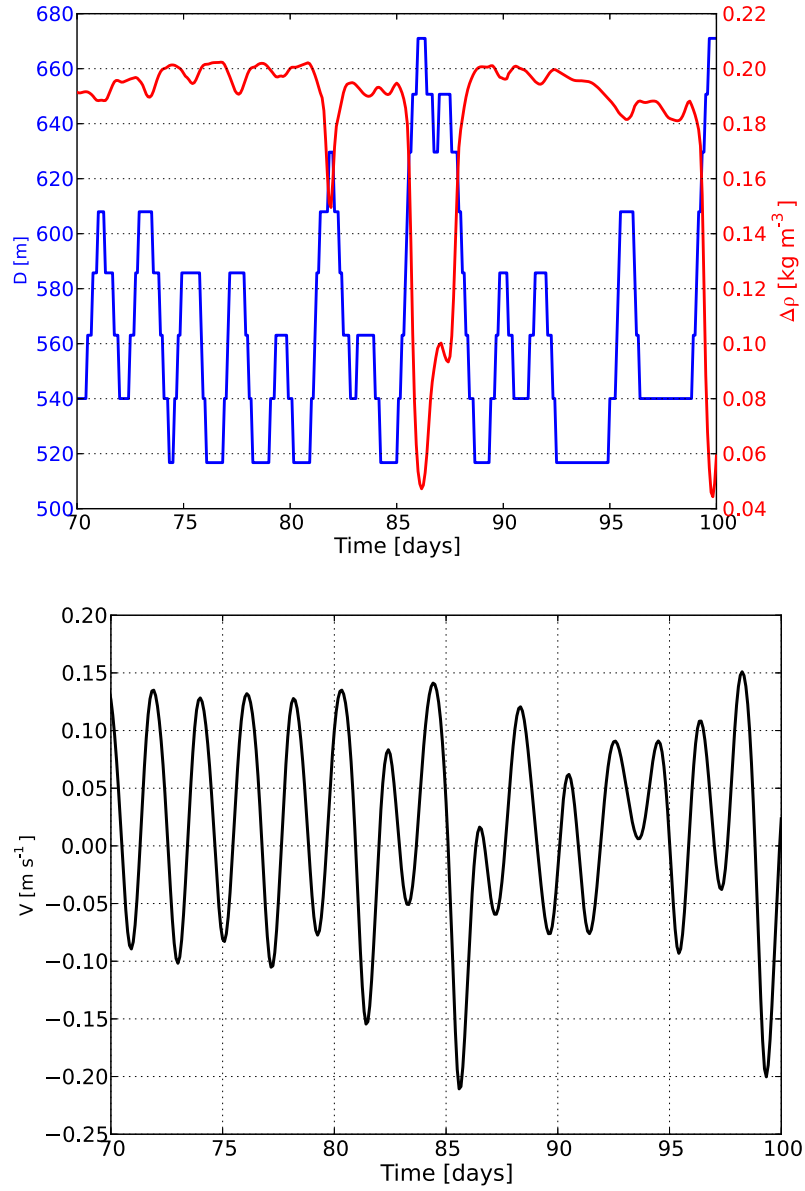


**Figure 3.3:** (top) Time series of layer thickness ( $D$ , m), density difference ( $\Delta\rho$ ,  $\text{kg m}^{-3}$ ) and (bottom) cross-slope depth-averaged velocity ( $V$ ,  $\text{m s}^{-1}$ ) at the northern end of the trough (green dot in Figure 1);  $D$  and  $\Delta\rho$  were used to compute the mean and spread of  $\Gamma$  values in Exp. #01. The total water depth  $H$  at this point is 700 m. Digitization of  $D$  represents steps in the vertical s-coordinate grid.

different ROMS simulations in a location outside the trough (e.g.,  $x = 100$  km). The total width of the domain ( $x_{max}$ ) was kept twice the width occupied by the continental shelf and the shelf slope (see an example of the setup for Exp.#12 in

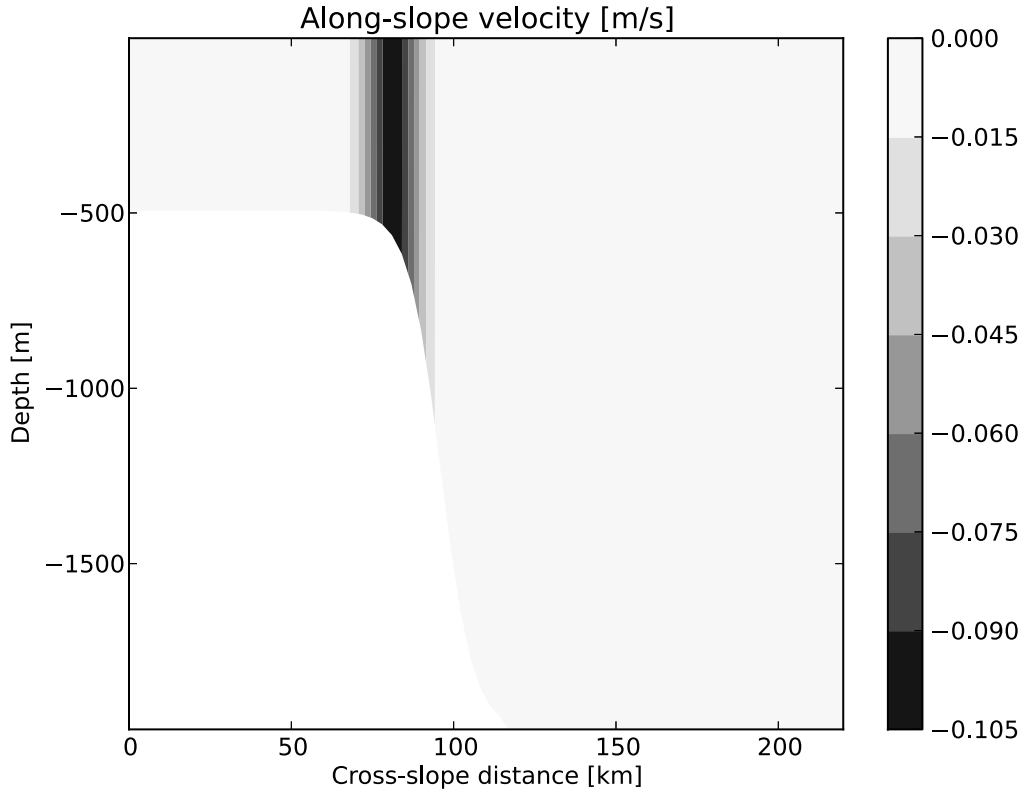


**Figure 3.4:** Domain setup and along-slope velocity ( $\text{m s}^{-1}$ ) used to compute the dispersion curve for Exp.#12.

Figure 3.4). This constraint avoids spurious solutions that appear when  $x_{\max}$  is too large relative to the natural cross-slope scale of the wave. This problem arises because the code uses an arbitrary force to create the resonance near  $x_{\max}/2$ .

In those runs where a background barotropic along-slope flow was prescribed (experiments # 12-14), the maximum along-slope flow ( $U_{\max}$ ) was set at the shelf break and exponentially decayed within 10 km towards the onshore and offshore regions (see an example of this flow field for Exp.#12 in Figure 3.4). Bottom friction was neglected and we used a closed boundary condition at  $x = 0 \text{ km}$  and open at  $x = x_{\max} \text{ km}$ .

### 3.1.2 Realistic model of the Ross Sea

We used a ROMS model developed for realistic simulations of the Ross Sea (Dinniman et al., 2011). The horizontal grid spacing was 5 km and the vertical grid consisted of 24 levels over realistic, but smoothed, bathymetry (Davey, 2004). The model was forced by the Antarctic Mesoscale Prediction System (AMPS), a mesoscale atmospheric forecast model (Bromwich et al., 2005). Rather than specifying surface fluxes due to sea ice from observations (Dinniman et al., 2011), the version used here incorporated a coupled sea-ice model (Budgell, 2005).

The model generates DSW over the continental shelf, primarily in polynyas along the Ross Ice Shelf front and close to the coast. The DSW then flows northward along the Drygalski and Glomar Challenger troughs (DT and GCT, respectively). These DSW flows are generally consistent with observations (Gordon et al., 2009; Budillon et al., 2011). The DSW mixes with other water masses over the outer continental shelf and upper slope to form AABW. Most production of DSW occurs in winter, and northward advection of DSW also varies seasonally due to a strong annual cycle in the wind stress. Delivery of the densest DSW to the continental slope is delayed by several months relative to production further south.

## 3.2 Results

### 3.2.1 Idealized simulations

The DSW prescribed at the southern boundary moves northward along the trough. Once it reaches the continental slope, most of the flow turns westward (left) due to the Earth's rotation (since  $f < 0$ ), while a fraction descends to the abyss in a frictional bottom Ekman layer. In the control run (Exp.#01), the velocity field to the east of the trough (Figure 3.1b) is wave-like, with a frequency ( $\omega$ ) of  $\sim 0.48$  cycles per day

(cpd) and a wavelength ( $\lambda$ ) of  $\sim 39$  km (Table 3.2; Figure 3.5). Wave properties vary as functions of slope, total depth and density anomaly. In all cases, frequencies (0.13–0.83 cpd) are sub-inertial ( $f(72^\circ)=1.91$  cpd), wavelengths (29–66 km) are greater than  $R_d$ , and phase speeds  $c_p = \omega/k$  are westward (0.07–0.51 m s<sup>-1</sup>). In experiments 01 to 13, energy propagates eastward (at the group speed  $c_g = \partial\omega/\partial k$ ), in the direction opposing both the dense outflow and  $c_p$  (Table 3.2). Westward energy propagation only occurs when westward  $U_{max}$  is large (Exp.#14).

Good agreement between the frequencies and wavelengths and theoretical dispersion relations from Brink (2006) confirms that all 14 simulations generated TVWs (Figure 3.5). Eastward energy flux is possible only because the ambient stratification is very weak. The dispersion curves obtained using typical stratification for the Weddell and Ross seas ( $N^2 = 2.5 \times 10^{-7}$  s<sup>-2</sup>) are very similar to the weak stratification case ( $N^2 \approx 0.0$  s<sup>-2</sup>) modeled here. Keeping other parameters consistent with our control run, but using a stratification value ( $N^2 = 7.0 \times 10^{-6}$  s<sup>-2</sup>) taken from a typical oceanic profile near the Mediterranean outflow (Price and Baringer, 1994), changes the characteristics of the TVWs (compare black and green curves in Figure 3.5) so that energy flux is always westward. Similarly, in the presence of strong westward background mean flow, energy at the shortest wavelengths no longer propagates eastward. At particular wavelengths,  $c_g \approx 0$  (Exps.# 13 and 14).

The relationship between the normalized oscillation period ( $T/T_{inertial}$ ) and  $\Gamma_{av}$  (Figure 4.4) is consistent with results from laboratory experiments obtained by Lane-Serff and Baines (1998) and in an idealized numerical study by Spall and Price (1998) (see their Figure 16b). The physical mechanism behind the time dependence of these oscillations can be explained as follows. As the DSW exits the trough, it “captures” the water above it. This ambient water is then stretched as it descends the slope and TVWs are excited as a consequence of potential vorticity conservation. The

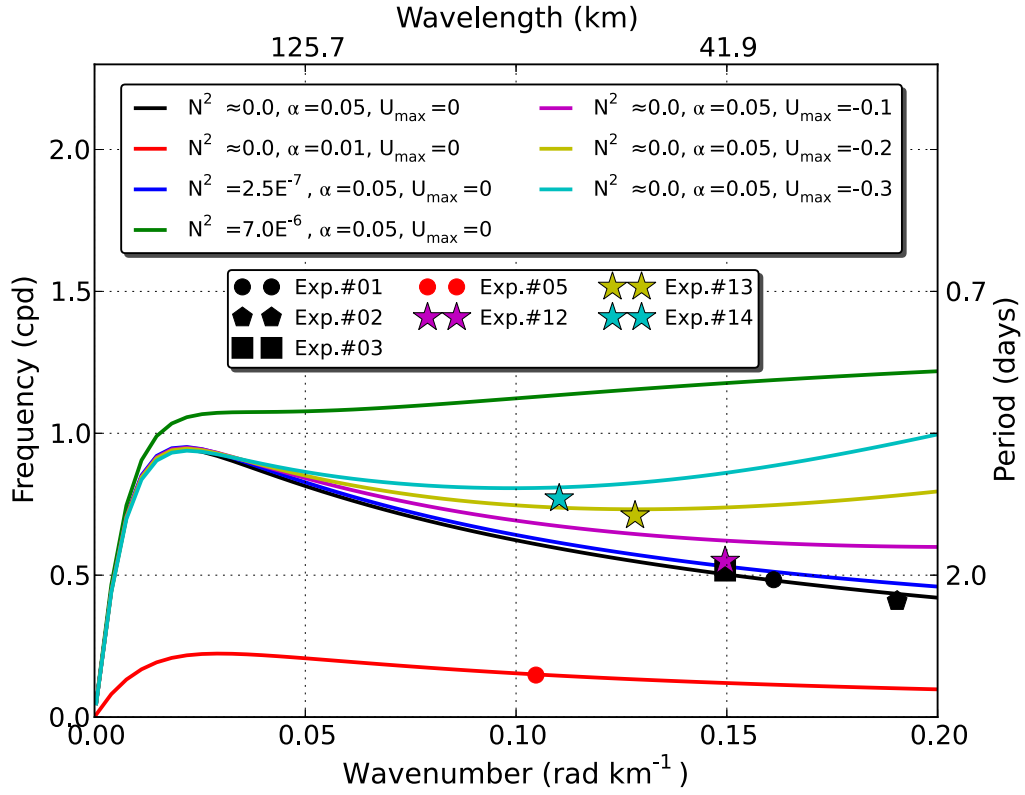


**Figure 3.5:** Dispersion curves from the *Brink* [2006] code (solid lines) using  $H_0 = 500$  m,  $|f| = 13.87 \times 10^{-5} \text{ s}^{-1}$  ( $72^\circ\text{S}$ ), for different ambient stratification ( $N^2$ ,  $\text{s}^{-2}$ ), slope ( $\alpha$ ) and westward along-slope flow ( $U_{max}$ ). Also shown are the frequency and wavenumber pairs calculated from time series of sea surface elevation extracted along the upper slope for selected model experiments. Color of each symbol matches color of the corresponding dispersion curve.

oscillation period decreases as the amount of stretching in the ambient water (with respect to  $D$ ) increases, with a limiting value of  $T \sim 2.3 \times T_{inertial}$  (Lane-Serff and Baines, 1998).

Two important parameters useful in defining the dynamical regime of overflows (Cenedese et al., 2004), are the Ekman number,  $Ek = (\delta/h_0)^2$ , where  $\delta$  is the Ekman layer thickness, and the Froude number,  $Fr = \Delta U / \sqrt{b_0 h_0}$ , where  $\Delta U$  is the velocity difference between the upper and bottom layers. Once the DSW exits the trough, all

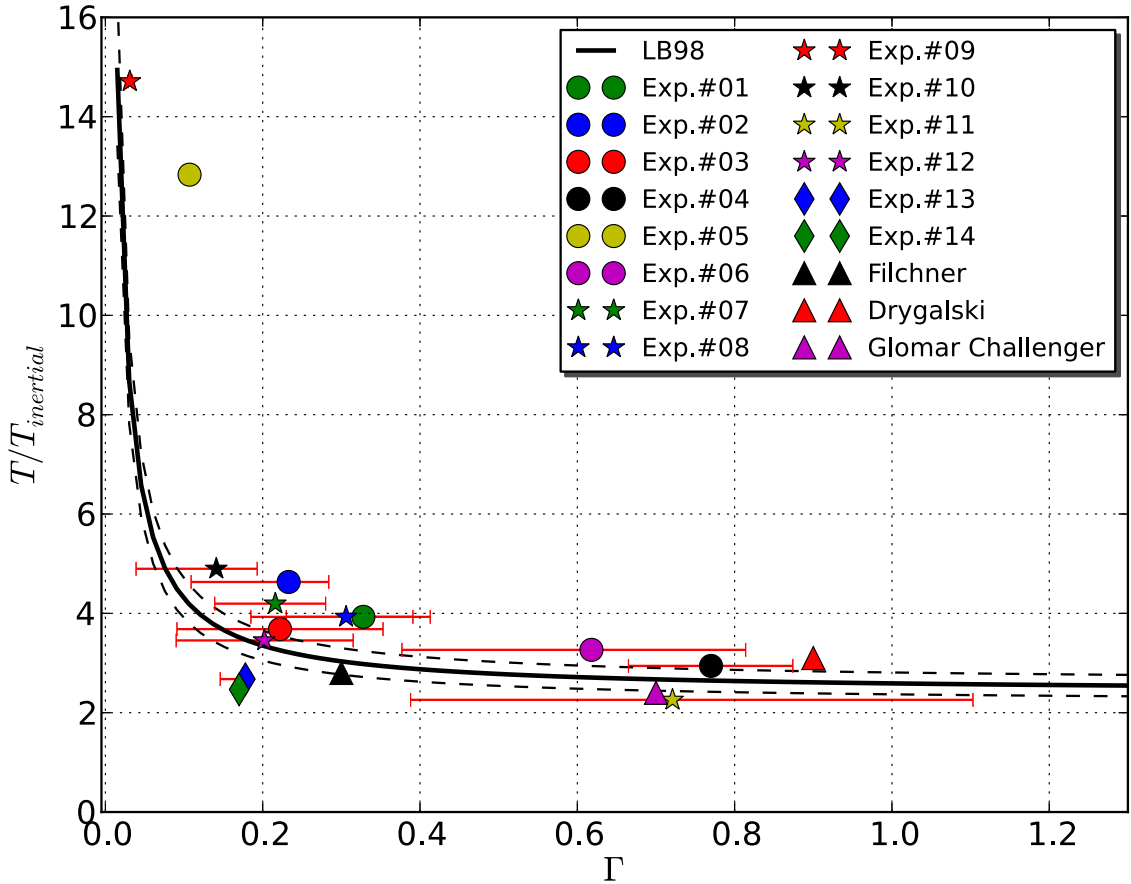


**Figure 3.6:** Wave period ( $T$ ) normalized by the domain-averaged inertial period ( $T_{inertial}$ ) as a function of the stretching parameter ( $\Gamma$ ) for all experiments listed in Table 3.2. The horizontal bars (red lines) are the 80% range of  $\Gamma(t)$  values for model time  $t=70-100$  days (see also Table 3.2). The curves from Lane-Serff and Baines (1998) are plotted for comparison (solid line is the mean and dashed lines show upper and lower limits). Also shown are representative values for the Filchner, Drygalski and Glomar Challenger overflow plumes (see Table 3.3).

idealized simulations presented here are characterized by  $Fr > 1$  and  $0.1 < Ek < 1$  values, which according to the laboratory overflow experiments of Cenedese et al. (2004) justify the wave regime observed.

Typical values for the Filchner, Drygalski and Glomar Challenger outflows yield  $\Gamma \approx 0.3$ , 0.9 and 0.7, respectively (Table 3.3), the difference being primarily due to larger  $\alpha$  in the Ross Sea. When combined with the  $\sim 35$  h oscillation period associated with the TVWs that Jensen et al. (2013) observed next to the Filchner outflow, the 38 h oscillation found in a numerical study of the Drygalski outflow (Padman et al., 2009), and the  $\sim 30$  h observed in our realistic model (see following Section), these estimates show good agreement with the numerical results presented here (Figure 3.6). The dataset analyzed by Jensen et al. (2013) showed seasonal variations in the evolution of the sub-inertial oscillations, with periods of  $\sim 39$  h during summer months and  $\sim 32$  h during winter months. Those authors showed that a stronger westward along-slope current during the winter months (which is the case for the Antarctic Slope Current) explain the higher frequencies observed during that season. Our results are consistent with their explanation, but we also show that wave frequency increases when the density anomaly of the outflow increases, increasing  $R_d$ .

**Table 3.3:** Estimated stretching parameter  $\Gamma$  and shelf waves oscillation period  $T$  for the following overflow plumes: Filchner (Foldvik et al., 2004; Wang et al., 2009; Jensen et al., 2013), Drygalski (Padman et al., 2009; Muench et al., 2009a) and Glomar Challenger (Section 3.2.2).

Variable	Filchner	Drygalski	Glomar Challenger
$R_d$ (km)	4	4.5	3
$\alpha$	0.03	0.1	0.1
$D$ (m)	400	500	400
$T_{inertial}$ (hour)	12.47	12.65	12.65
$\Gamma$	0.3	0.9	0.7
$T/T_{inertial}$	2.8	3.2	2.4

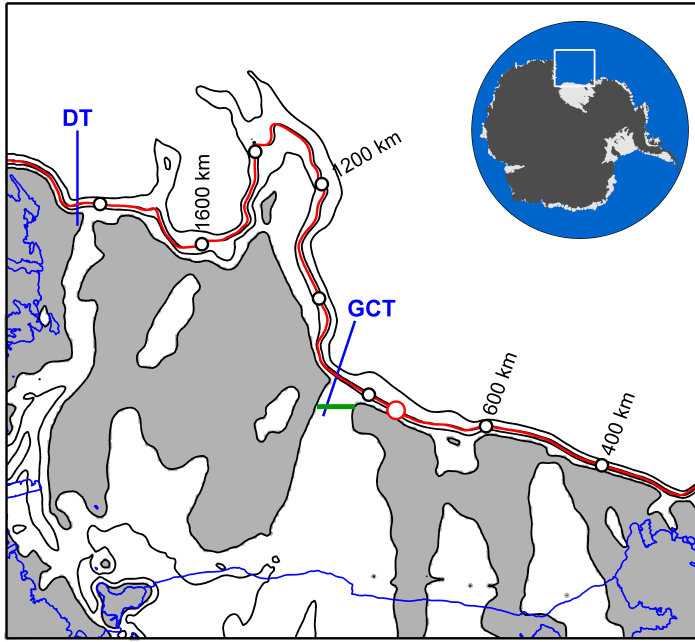


**Figure 3.7:** Map of Ross Sea. Shaded areas are water depths shallower than 530 m; black contours show 750 and 1500 m isobaths. Red line shows 1000 m isobath. Open circles are every 200 km along the isobath.

### 3.2.2 Realistic model of Ross Sea outflows

Analyses of one year of output from our Ross Sea ROMS simulation (see Section 3.1.2) show that oscillations with periods of  $\sim 30$  h occur along sections of the continental shelf north and east of the Drygalski and Glomar Challenger troughs (DT and GCT, respectively; see Figure 3.7e for locations). A Hovmöller diagram of the band-passed (0.3–1 cpd), depth-averaged, cross-slope velocity (Figure 3.8a) shows westward phase propagation at  $c_p \approx 1.6$  m s $^{-1}$  and eastward energy propagation with  $c_g \approx 0.5$  m s $^{-1}$ , confirming that these oscillations are the short-wavelength mode of the TVW dispersion curves. The TVWs propagate several hundred kilometers eastward from their sources.

The realistic, time-varying atmospheric forcing in this simulation modulates DSW production,  $U_{max}$ , and ambient stratification, causing temporal changes in production

and propagation of TVWs. For example, at a location  $\sim$ 100 km east of the GCT, cross-slope velocity associated with the TVWs can vary from negligible to  $>0.25 \text{ m s}^{-1}$  (Figure 3.8b) through the year, with some modulation also on shorter time scales. This modulation provides the signal of eastward energy propagation seen in Figure 3.8a.

The variability in TVW energy is correlated with seasonal changes in the strength of the along-slope mean flow (Figure 3.7b) and mean potential density ( $\sigma_\theta$ ) of the deep water in the northern GCT (Figure 3.7c). The loss of TVWs in winter (days 180–260) corresponds with stronger westward flows and low  $\sigma_\theta$  in the GCT, consistent with the results from our set of idealized models.

### 3.3 Summary

Idealized numerical simulations demonstrate that outflows of dense shelf water (DSW) from the Antarctic shelf seas onto the continental slope generate topographic vorticity waves (TVWs) that then propagate along the slope. The properties of these waves are consistent with observed variability along the southern Weddell Sea continental slope near the Filchner Trough outflow. The period ( $T$ ) of the TVWs decreases as the stretching parameter  $\Gamma$  increases, implying that higher frequency waves will be generated when the continental slope is steeper and when the density anomaly of the outflow is increased. In addition, stronger mean westward along-slope flows, representing the Antarctic Slope Current, will reduce the wave period. For most of our model configurations, the energy flux of the TVWs is eastward from the trough, opposing the westward transport of the dense outflow and the TVWs' phase propagation. Westward TVW energy flux only occurs when the mean westward along-slope flow is sufficiently strong.

In our idealized simulations and in our realistic model of the Ross Sea, the TVW cross-slope currents often exceed  $0.2 \text{ m s}^{-1}$ , suggesting that they contribute to mixing and cross-slope advection in the vicinity of troughs. These are regions of important cross-slope exchanges – outflows of DSW leading to AABW production and inflows of heat onto the continental shelf and south to the ice shelves – implying that our ability to represent these exchanges depends on accurate models of TVW production, propagation and dissipation (not discussed here). The realistic Ross Sea model demonstrates strong time-dependence of TVW energy east of Drygalski and Glomar Challenger troughs, correlated with seasonal variability of DSW properties and along-slope mean flow.

### Acknowledgments

The contents of this chapter have been published in Geophysical Research Letters, 2014, coauthored by Professor Tamay Özgökmen, Dr. Laurie Padman, Dr. Scott R. Springer and Susan L. Howard. This study was funded by the National Science Foundation, grants OCE-0961405 and OCE-0722644 (MRI) to Earth & Space Research (ESR) and OCE-0961369 to the University of Miami. We thank Prof. K. Brink (WHOI) for providing the code for calculating dispersion curves for inviscid coastal trapped waves and M. Dinniman (Old Dominion University) for developing the realistic ROMS model of the Ross Sea. We also thank University of Miami's Center for Computational Science for making available their resources.

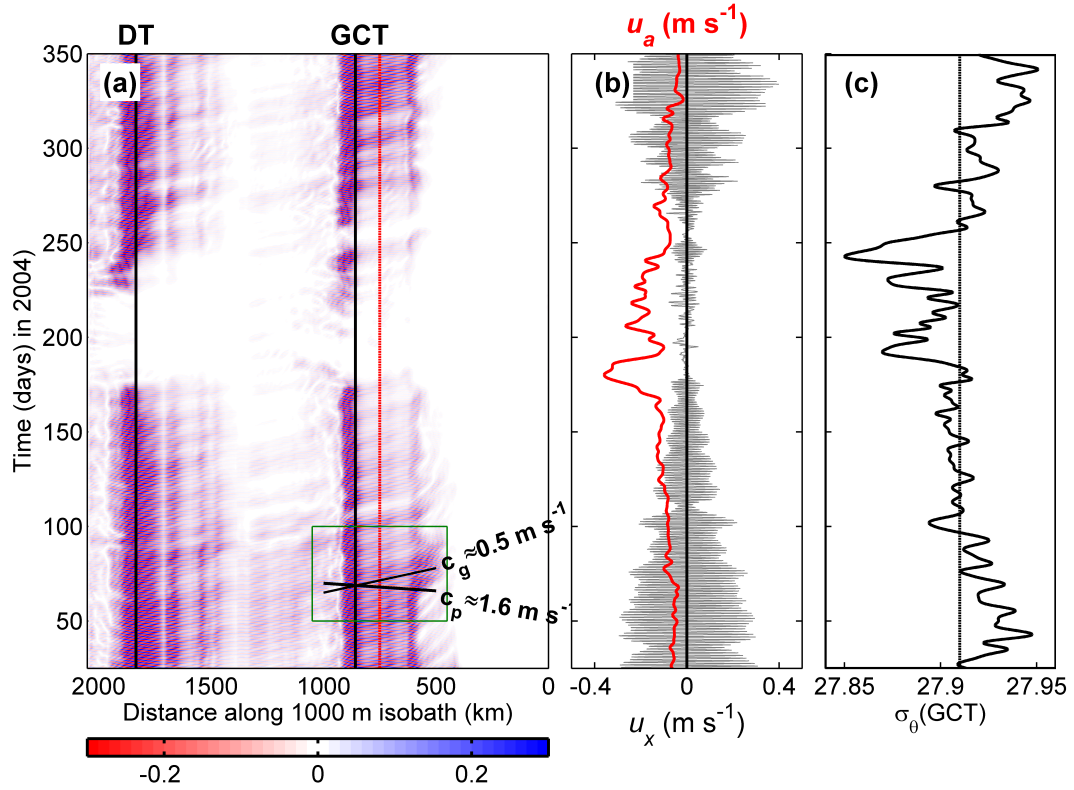


**Figure 3.8:** (a) Hovmöller diagram for band-passed (0.3-1 cycle per day (cpd)) cross-slope, depth-averaged velocity as a function of time in days of 2004 (y-axis) and distance (x-axis) along the 1000-m isobath (red contour in Fig. 3.7), representing the upper continental slope in the Ross Sea, Antarctica. Black vertical lines indicate western edges of the Drygalski Trough (DT) and Glomar Challenger Trough (GCT); see Fig. 3.7 for locations. Red line is location of a point  $\sim 100$  km east of GCT; see red circle on 1000-m isobath in Fig. 3.7. Typical values of group velocity ( $c_g$ ) and phase velocity ( $c_p$ ) are indicated. (b) Band-passed (0.3-1 cpd) across-slope (gray) and low-passed ( $<0.3$  cpd) along-slope (red) velocity components at the 1000-m isobath, at the point  $\sim 100$  km west of GCT. (c) Mean potential density averaged along a transect across the northern GCT, for all model coordinate depths below 300 m; see green line in Fig. 3.7 for location. Vertical line at  $\sigma_0 = 27.91$  is the approximate value below which TVWs are not found.

# Chapter 4

## Double plume formation in numerical simulations of oceanic outflows

The contents of this chapter will be submitted to Ocean Modelling. Here, we explore the formation of a double plume pattern in two-dimensional non-hydrostatic numerical simulations of oceanic outflows. This type of flow has been observed in previous laboratory experiments, and this is the first time that such phenomenon has been captured in numerical simulations. Based on the relevant physical parameters, the conditions under which the double plume regime might occur in oceanic outflows are investigated.

### 4.1 Background

A flow pattern, referred to as double plume regime, has been observed in laboratory experiments of dense water flowing down slopes and into stratified environments (see Fig. 4.1; Baines, 2008). This type of flow is not fully understood, and it has not been modeled yet. It is characterized by the separation of the main plume into two branches: a denser and less diluted plume adjacent to the bottom, and a less dense and more diluted plume located at intermediate depths. The main goal of this

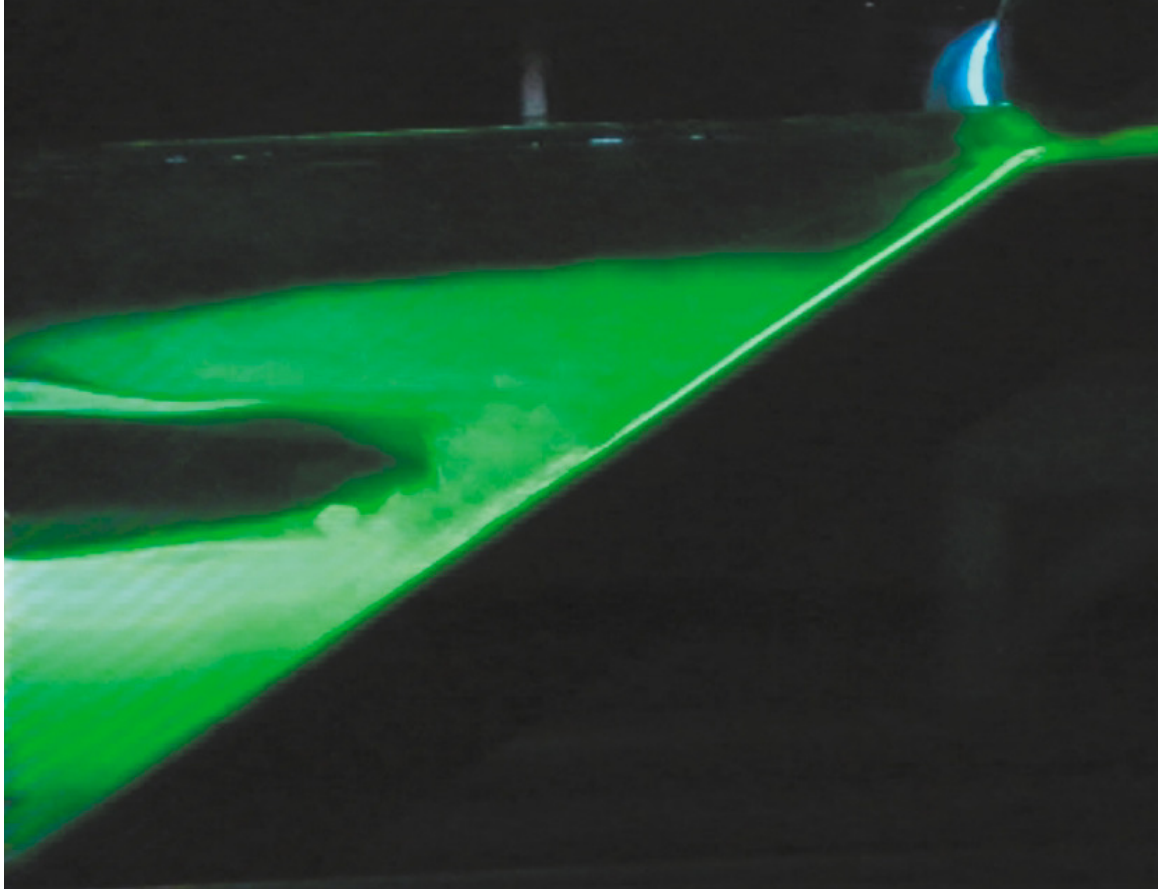


**Figure 4.1:** An example of a double plume regime observed in the laboratory on a slope of  $30^{\circ}$  (from Baines, 2008). The fluid has been dyed with fluorescense and is illuminated by a thin laser beam that scans a central vertical section.

Chapter is to investigate whether a single outflow that delivers water to both the deep benthic ocean and intermediate layers simultaneously can be generated in numerical simulations under realistic geophysical parameters and scales.

A common feature of oceanic outflows is the occurrence of a strong velocity shear at the interface between the dense plume and the overlying less dense ambient water. This shear may lead to Kelvin-Helmholtz instabilities, where less dense water is entrained into the dense plume due to the overturning of isopycnals. Combined with additional turbulent mixing, this process dilutes the dense current, while increasing its volume transport. Entrainment is therefore a fundamental property of oceanic

outflows (e.g., Price and Baringer, 1994; Legg et al., 2009). Another type of shear-induced instability may also occur within the bottom boundary layer as a consequence of the bottom stress at the sea-floor. However, unlike the interfacial instability, the latter has less effect on mixing since it tends to homogenize the tracer properties in the boundary layer (e.g., Peters et al., 2005). In addition, this process acts as an important sink of kinetic energy and must be correctly represented in numerical simulations of oceanic outflows (Legg et al., 2006).

Most of our understanding on entrainment ( $E$ ) in oceanic outflows comes from laboratory experiments of bottom gravity currents (Ellison and Turner, 1959; Lane-Serff and Baines, 1998; Simpson, 1999; Baines, 2001, 2005; Cenedese et al., 2004). Based on the bulk Froude number ( $Fr = \frac{U}{\sqrt{g'h_o}}$ , where  $U$  is the mean plume velocity,  $g'$  is the plume buoyancy anomaly and  $h_0$  is the plume thickness), Ellison and Turner (1959) proposed the following empirical function:

$$E = \begin{cases} \frac{0.08Fr^2 - 0.1}{Fr^2 + 5} & \text{for } Fr \geq 1.25 \\ 0 & \text{for } Fr < 1.25 \end{cases} \quad (4.1)$$

This function works well in the absence of rotation and under homogeneous ambient water. The  $Fr=1.25$  cutoff value determines the nature of the plume (turbulent entraining or laminar). However, laboratory experiments conducted by Cenedese et al. (2004) have shown that, in the presence of rotation and homogeneous ambient stratification, eddies and waves may cause entrainment when  $Fr < 1.25$ . Therefore, equation 4.1 is not applicable to all systems.

As the non-rotating laboratory experiments of Baines (2001, 2005, 2008) have shown, downslope flows into stratified environments may result in three flow types: 1) gravity currents, in which the so-called detrainment takes place; 2) entraining plumes,

which are characterized by the constant entrainment of ambient fluid into the bottom current due to Kelvin-Helmholtz billows; and 3) the double plume regime, where the density current separates into a denser and less diluted plume adjacent to the bottom and a less dense and more diluted plume located at intermediate depths (Fig. 4.1). Baines (2008) showed that the mixing character of the flow in these different regimes can be determined using  $E$ , the slope angle ( $\theta$ ), the drag coefficient ( $C_d$ ) and the so-called buoyancy number ( $B$ ):

$$B = \frac{Q_0 N^3}{g_0' r^2}, \quad (4.2)$$

where  $Q_0$  is the volume flux of the dense water flow per unit width at the top of the slope,  $N$  the ambient stratification frequency and  $g_0'$  is the initial reduced gravity. Overall, gravity currents occurred on sufficiently small slopes and entraining plumes on sufficiently steep slopes. Dynamically, the condition for gravity currents is  $C_d + E > 0.2B^{0.4} \sin\theta$ . The double plume regime was observed in just a few experiments on  $30^\circ$  slopes and with small values of  $B$ . However, laboratory experiments must be configured using slope angles much larger than those observed in nature. Otherwise the dense water cannot accelerate within the bounds of typical laboratory tanks [ $O(1$  m)] and the flow is not turbulent. Therefore, it is uncertain as to whether the results derived from the laboratory experiments of Baines (2002, 2005, 2008) remain valid for geophysical parameters and scales.

Since some realistic parameters cannot be incorporated into laboratory experiments, numerical simulations have been used to complement our understanding of the dynamics of bottom density currents from a geophysical point of view (Özgökmen and Chassignet, 2002; Özgökmen et al., 2004, 2006; Özgökmen and Fischer, 2008). Özgökmen et al. (2006) explored the effects of ambient stratification on the entrainment and properties of dense bottom currents that equilibrated at intermediate

depths. In their experiments,  $0.125 \leq B \leq 0.46$  and  $3^\circ \leq \theta \leq 7^\circ$ . It was found that mixing by Kelvin-Helmholtz rolls did not penetrate all the way to the bottom of the gravity current and, therefore, the densest bottom water remained undiluted until the equilibration level was reached. However, as pointed by the authors, the regime where more vigorous mixing can occur remains to be investigated using a deeper domain so that bottom separation and product water mass formation with smaller  $B$  can be captured.

The present study complements previous investigations by considering cases where  $B \leq 0.125$  and with more realistic domains. The high resolution numerical simulations presented here captured, for the first time, the double plume regime in oceanic environments. The relation between this type of flow and the presence of internal hydraulic jumps is discussed, and the conditions under which the double flow regime might occur in oceanic outflows are investigated.

## 4.2 Numerical setup

The numerical simulations presented here are conducted using the Massachusetts Institute of Technology general circulation model (MITgcm) (Marshall et al., 1997b,a), configured to solve the nonhydrostatic Boussinesq equations in a two-dimensional configuration and without rotation. MITgcm is a height-coordinate model that employs partial step topography (Adcroft et al., 1997) and the configuration employed in this paper includes a free surface. Nonhydrostatic dynamics are essential to correctly represent Kelvin-Helmholtz instabilities, an important mechanism for mixing in bottom gravity currents (Simpson, 1999). Given our available computational resources and the fact that we are using a geophysical domain with very small grid resolution, we are forced to perform two-dimensional simulations. However, this is a reasonable first step since some oceanic outflows are confined into channels and troughs, and in those

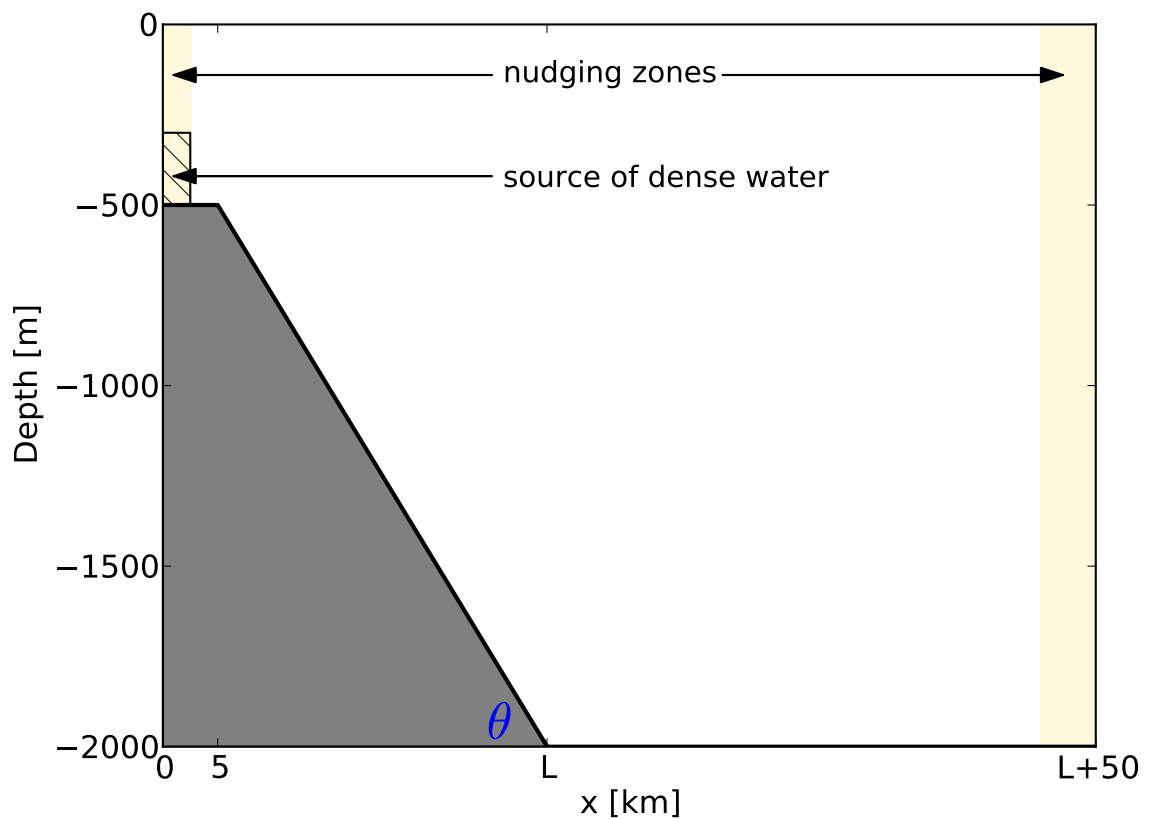


**Figure 4.2:** Schematic of the model domain.

cases the dynamics of the plume may be reasonably represented by two-dimensional processes. In addition, due to the relative inexpensiveness of two-dimensional simulations a complete parameter space investigation can be performed, so that the controlling physical processes can be identified.

The model domain is depicted in Fig. 4.2. It includes a 5 km wide flat continental shelf that is connected to a flat deep ocean through a constant shelf slope  $\alpha = \tan(\theta)$ . Three different shelf slopes are used: steep ( $\alpha = 0.1$ ), moderate ( $\alpha = 0.05$ ) and shallow ( $\alpha = 0.01$ ). We note that the maximum continental shelf slope next to the major oceanic outflows fall within this range (Price and Baringer, 1994). The depth varies from 500 m at the shelf to 2000 m at the deep ocean. The total length (L+50 km) varies between 70 and 205 km, depending on the slope used. The dense water is prescribed in the first 2.5 km of the domain and below 300 m depth (see hatched region in Fig. 4.2). To avoid complications that may arise through processes such as thermobaricity and cabbeling, a linear equation of state as a function of temperature ( $T$ ) is employed:  $\rho = \rho_0(1 - \alpha T)$ , where  $\rho_0 = 1025 \text{ kg m}^{-3}$  is the background density and  $\alpha = 5.3 \times 10^{-5} \text{ }^{\circ}\text{C}^{-1}$  is the thermal expansion coefficient. A passive tracer ( $\tau$ ) with an initial concentration of  $1 \text{ kg m}^{-3}$  is imposed with the dense plume to help visualizing the flow behavior.

Both horizontal ( $\Delta x$ ) and vertical ( $\Delta z$ ) resolutions are set to 5 m, since previous 2D numerical simulations of bottom gravity currents under geophysical scales and parameters have shown that such grid spacing is small enough to resolve the Kelvin-Helmholtz billows (Özgökmen and Chassignet, 2002). These billows pull lighter water down under denser water, and additional mixing results in a water with intermediate density. This is an important process that takes place at the interface between the dense water and the ambient lighter water. In addition,  $\Delta z$  is high enough to resolve the bottom viscous layer and  $\Delta x \leq \Delta z/\alpha$ . Therefore, our simulations capture the

homogenization of tracers induced by the mixing driven by frictionally generated shear (Winton et al., 1998).

In addition to the shelf slope, another key parameter is the initial ambient stratification ( $N$ ), which is constant throughout the water column. As shown in Fig. 4.3, three different background density profiles are used by varying  $N$  over a factor of two:  $1.0 \times 10^{-3} \text{ s}^{-1}$ ,  $7.5 \times 10^{-4} \text{ s}^{-1}$  and  $5.0 \times 10^{-4} \text{ s}^{-1}$ . This range is equal to varying the background density profile by a factor of four (from 0.05 in the weaker stratified case to  $0.2 \text{ kg m}^{-3}$  in the stronger stratified case, see Fig. 4.3). Using these values of  $N$  and the above mentioned values of  $s$ , a set of nine numerical experiments were conducted (Table 4.1). The initial density difference between the outflow and the ambient water just above it (i.e.,  $\rho$  at  $z=-300 \text{ m}$ ) is  $\Delta\rho = 0.2 \text{ kg m}^{-3}$  in all experiments. Therefore, the imposed outflow density is always larger than the initial ambient density at  $z=-2000 \text{ m}$ .

Laplacian friction is employed in the momentum equations. The vertical component of viscosity is set to  $\nu_v = 10^{-4} \text{ m}^2 \text{ s}^{-1}$ , while the horizontal component is set to  $\nu_h = 5.0 \text{ m}^2 \text{ s}^{-1}$ . The latter is chosen such that the grid Reynolds number ( $\text{Re}_g = U\Delta x/\nu_h$ , where  $U$  is the maximum plume velocity) is always less than 1.5. It has been shown that this condition is effective in eliminating grid-scale noise (Griffies, 2004; Ilicak et al., 2012). Although these values are much larger than laboratory and realistic oceanic conditions, they are required for numerical rather than physical reasons, and the simulations will be at lower Reynolds number than laboratory and oceanic flows. Tracers are advected using a third-order direct space-time flux limited scheme, which eliminates grid-scale noise by introducing numerical diffusivity where needed. Therefore, the explicit tracer diffusivities are set to zero. Since the problem investigated here includes shocks and propagating fronts, the use of a flux limited scheme is essential to avoid unphysical behavior in terms of mixing (see Chapter 2).

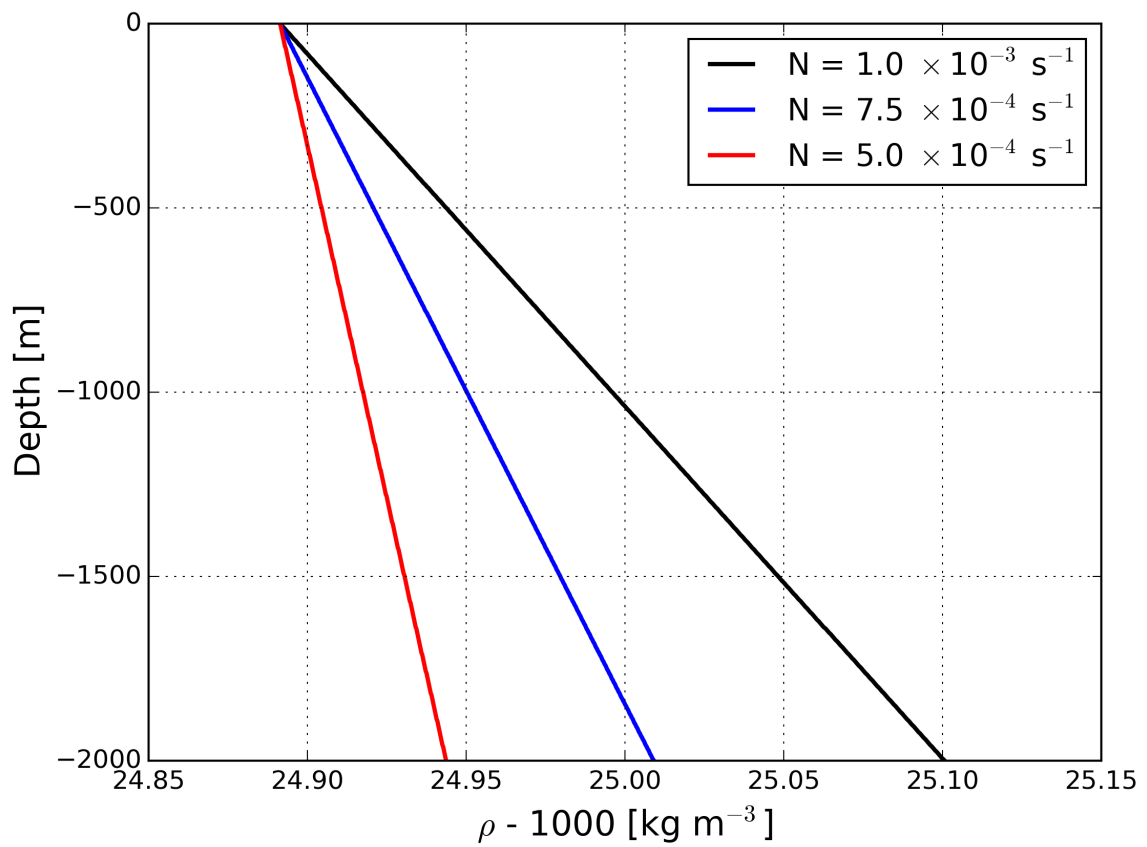


**Figure 4.3:** The three different background density ( $\rho - 1000$ ,  $\text{kg m}^{-3}$ ) profiles used in the numerical experiments.

**Table 4.1:** Summary of numerical experiments conducted.

	$\alpha=\tan(\theta)$	L (km)	N ( $s^{-1}$ )	Run time (hours)
EXP1	0.1	20	$1.0 \times 10^{-3}$	150
EXP2	0.05	35	$1.0 \times 10^{-3}$	180
EXP3	0.01	155	$1.0 \times 10^{-3}$	324
EXP4	0.1	20	$7.5 \times 10^{-4}$	110
EXP5	0.05	35	$7.5 \times 10^{-4}$	180
EXP6	0.01	155	$7.5 \times 10^{-4}$	115
EXP7	0.1	20	$5.0 \times 10^{-4}$	36
EXP8	0.05	35	$5.0 \times 10^{-4}$	50
EXP9	0.01	155	$5.0 \times 10^{-4}$	100

No-slip boundary conditions are applied to the momentum equations at the bottom, while no-flux conditions are applied to tracers at the free-surface. The side boundaries are kept closed and tracers and momentum are nudged towards the initial condition within regions that are 2.5 and 5.0 km wide, starting from the left and right boundaries, respectively (see Fig. 4.2). A relaxing timescale of 360 seconds is used for both tracers and momentum. This procedure avoids that internal waves are reflected at the boundaries and also acts as a source/sink of momentum and tracers. All simulations are started from rest and the model is stopped instants after the passive tracer reaches the nudging zone at the right boundary. The total integration time for each simulation is shown in Table 4.1.

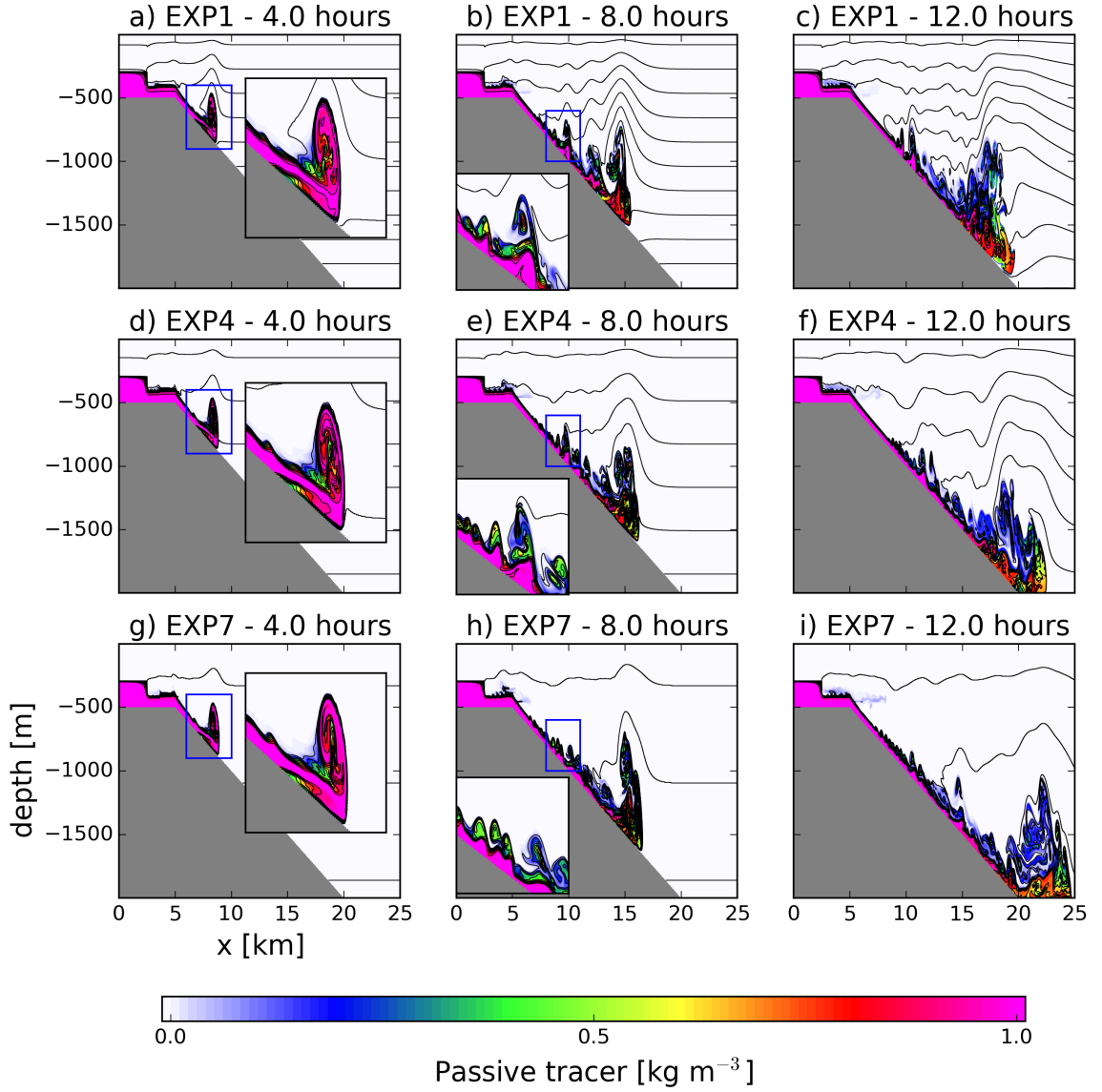


**Figure 4.4:** Snapshots of passive tracer distribution ( $\text{kg m}^{-3}$ , color) and density contours ( $\text{kg m}^{-3}$ , black lines plotted every  $0.02 \text{ kg m}^{-3}$ ) for three different experiments: (top) EXP1,  $N = 10^{-3} \text{ s}^{-1}$ ; (middle) EXP4,  $N = 5 \times 10^{-4} \text{ s}^{-1}$  and (bottom) EXP7,  $N = 7.5 \times 10^{-4} \text{ s}^{-1}$ . Each simulation is shown at three instants (left)  $t = 4$  hours; (center)  $t = 8$  hours and (right)  $t = 12$  hours. The blue boxes in the left and middle panels denote the boundaries for the closeups shown on the plots. Note that only the nearshore portion of the computational domain is illustrated here.

## 4.3 Results

### 4.3.1 Flow description

We start by analyzing the passive tracer distribution and density contours taken at 4, 8 and 12 hours after the system has started. Three different experiments are described EXP1, EXP4 and EXP7, and the only difference between them is in the initial ambient stratification imposed, which is strong ( $1.0 \times 10^{-3} \text{ s}^{-1}$ ), moderate ( $7.5 \times 10^{-4} \text{ s}^{-1}$ ) and weak ( $5.0 \times 10^{-4} \text{ s}^{-1}$ ), respectively (see Table 4.1). In all these experiments the shelf slope is  $\alpha = 0.1$ .

The initial development of the system is that of the so-called lock-exchange flow (e.g., Simpson, 1999), in which the denser fluid propagates downslope while the lighter fluid flows in the opposite direction along the top boundary of the domain. All cases show the development of a characteristic head as the leading edge of the outflow propagates downslope (left panels in Fig. 4.4). The head is half of a dipolar vortex, which is a typical feature observed in two-dimensional systems by self-organization of the flow (e.g., Flierl et al., 1983) and corresponds to the most probable equilibrium state maximizing entropy (Smith, 1991). The initial growth of the head is observed in all experiments, as less dense ambient water entrains into the leading plume.

At the tail of the current (i.e., the region behind the head), it is possible to observe the rolling up of the density interface at the top edge of the current (middle panels in Fig. 4.4). These counter-clockwise vortices are indicative of Kelvin-Helmholtz instability, in which waves made up of less dense fluid entrain into the dense current. The size of these features varies between 50-200 m and, therefore, the grid resolution employed here ( $\Delta x = \Delta z = 5 \text{ m}$ ) is enough to capture them. There is a general tendency of these vortices to coalesce and form larger vortices via pairing (not shown), and this a well documented behavior of two-dimensional Kelvin-Helmholtz instability

(e.g., Özgökmen and Chassignet, 2002). At this point, clockwise vortices due to frictionally generated shear are also evident in the bottom boundary layer (middle panels of Fig. 4.4). These features act as a sink of kinetic energy and, unlike the Kelvin-Helmholtz rolls, tend to homogenize the water properties next to the bottom with (i.e., they have less effect on interfacial mixing).

In EXP1 the head merges with the trailing current before the leading edge reaches the end of the slope (Fig. 4.4b). Soon after, a portion of the passive tracer leave the slope and flow out into the interior (Fig. 4.4c). This indicates that mixing between the density current and the ambient water generated fluid parcels that have found their neutral buoyancy level. This process is known as detrainment and it has been previously observed in laboratory experiments of dense water flowing down slopes into stratified environments (Baines, 2005). Although less evident, a similar process occurs in EXP4 (Fig. 4.4h and i), but this takes place at a latter time in the run when compared to EXP1. Finally, in EXP7 the head always remains attached to the main bottom current, and head growth (or entrainment) occurs even after the outflow reaches the end of the slope (Fig. 4.4e and f).

Snapshots of passive tracer taken at the end of the simulations show the impact of ambient stratification on the structure of the density current (Fig. 4.5). In EXP1, mixing results in the generation of two plumes (Fig. 4.5a): one denser (less diluted) at the bottom and one less dense (more diluted) at intermediate depths. The structure of the system resembles the double outflow regime observed in a laboratory experiment presented by Baines (2008) and previously discussed in Section 4.1 (see Fig. 4.1).

A similar double outflow structure is seen in the moderate ambient stratification experiment, EXP4 (Fig. 4.5b). However, the vertical distance between the two outflows is smaller than in EXP1. The weaker passive tracer concentration in the bottom and intermediate plumes of EXP4 suggests that mixing is stronger than in EXP1.

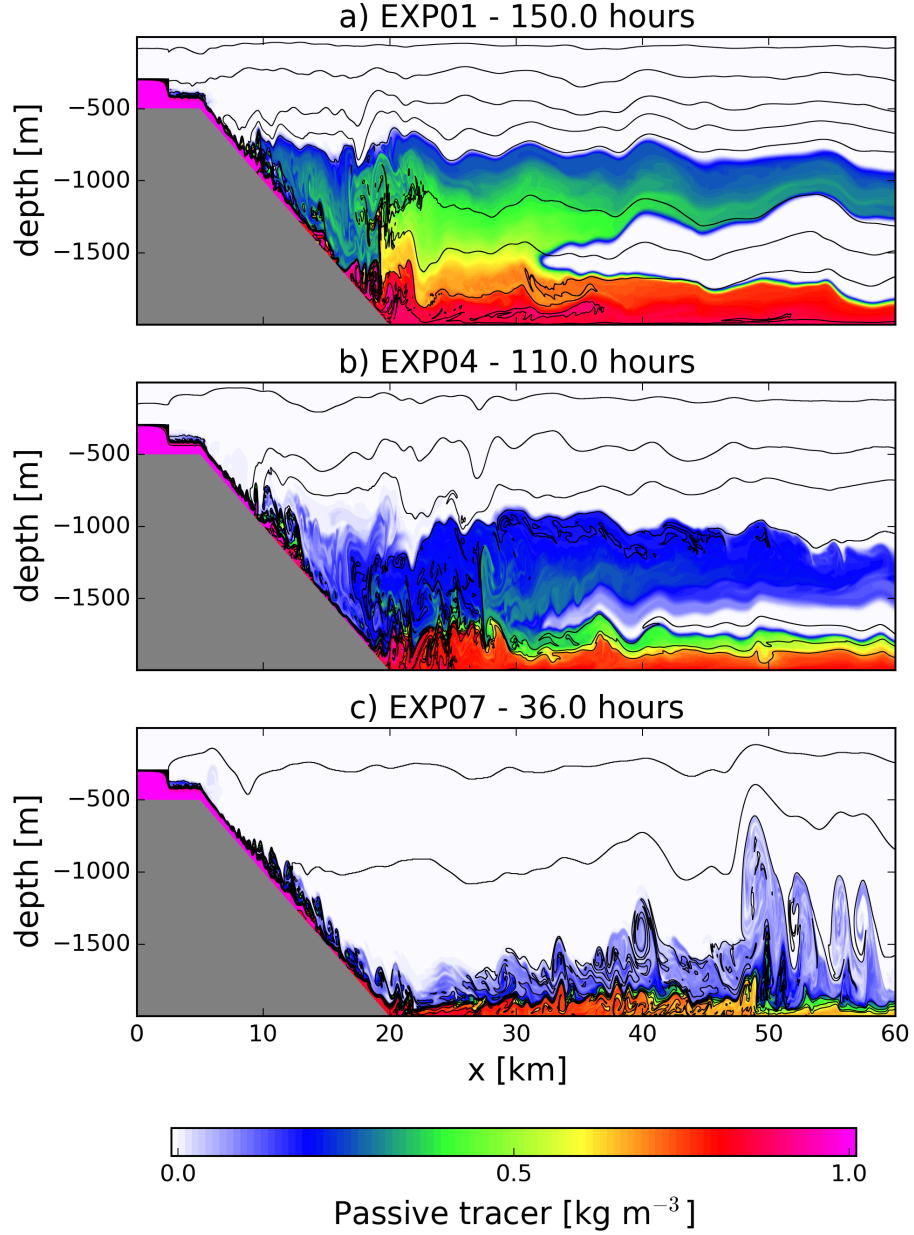


**Figure 4.5:** Snapshots of passive tracer distribution ( $\text{kg m}^{-3}$ , color) and density contours ( $\text{kg m}^{-3}$ , black lines plotted every  $0.02 \text{ kg m}^{-3}$ ) at the end of the simulation for three different experiments: a) EXP1 at  $t = 150$  hours; b) EXP4 at  $t = 110$  hours and c) EXP7 at  $t = 36$  hours.

Finally, unlike the previous cases, the final condition for the weak ambient stratification experiment (EXP7) shows only one plume (Fig. 4.5c). With exception of a

small region located at the upper slope ( $\sim 7$  km long), the bottom current shows sign of strong turbulence throughout the domain.

### 4.3.2 Dense water thickness, Froude number and energy dissipation

The passive tracer field in EXP01 shows different mixing regions before and after  $x \sim 18$  km (Fig. 4.5a). The onshore region is characterized by a “pool” of homogeneous fluid sitting on the top of the bottom current. This fluid has been strongly diluted by the Kelvin-Helmholtz rolls and the subsequent mixing. The offshore region is characterized by a thick plume with water classes ranging between the less dense intermediate plume to the denser and less diluted plume. The presence of different mixing zones also occurs in EXP4 (Fig. 4.5a), although in this case the separation boundary occurs further offshore ( $x \sim 27$  km). However, these different mixing zones are not present in EXP7 (Fig. 4.5c). We then define the bottom plume thickness ( $h_0$ ) in experiments EXP1, EXP4 and EXP7 based on the  $\tau = 0.75, 0.56$  and  $0.38 \text{ kg m}^{-3}$  contours, respectively. This selection is somehow arbitrary and  $h_0$  is sensitive to the choice of  $\tau$ . Based on visual inspection of the passive tracer fields in EXP1, the  $\tau = 0.75 \text{ kg m}^{-3}$  contour seems to distinguish the bottom density current from the upper tracers that have been detrained. The values for EXP4 and EXP7 were then scaled based on the ambient stratification with respect to that in EXP1.

In EXP1, the plume thickness averaged over the last 25 hours of simulation ( $\langle h_0 \rangle$ ) shows a strong jump between  $17 \leq x \leq 19$  km (Fig. 4.6, black line on top panel). A similar jump also occurs in EXP4 (Fig. 4.6, blue line on top panel), but it is weaker and further offshore than in EXP1. The presence of a “pool” of homogeneous fluid sitting on the top of the bottom current in combination with internal hydraulic jump has been previously observed and modeled by Cummins et al. (2006). However, in that

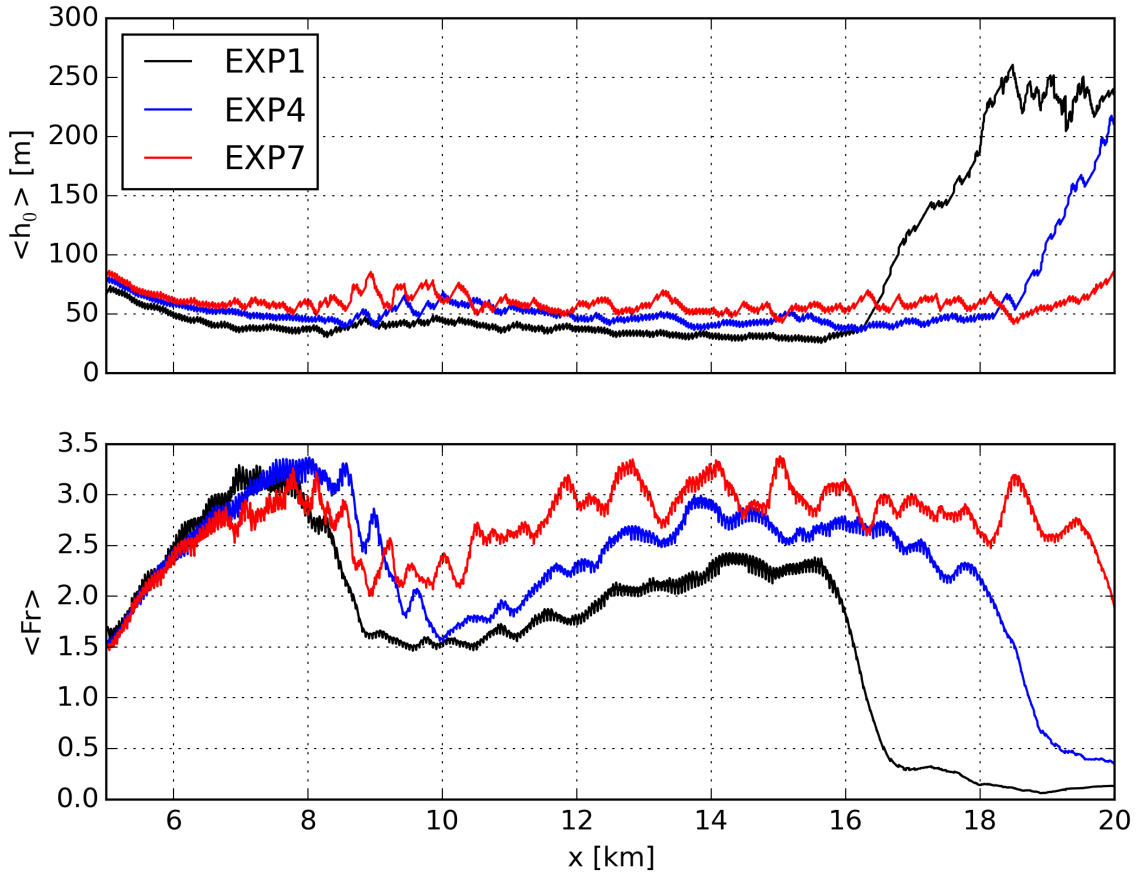


**Figure 4.6:** Time-averaged plume thickness,  $\langle h_0 \rangle$  (top) and Froude number,  $\langle Fr \rangle$  (bottom) as a function of cross-slope distance for experiments EXP1, EXP4 and EXP7.

case the jump occurs in the upper ocean. In EXP7, the jump is not present and  $\langle h_0 \rangle$  is almost constant throughout the slope (Fig. 4.6, red line on top panel). The presence of jumps, or discontinuities, are often associated with internal hydraulic jumps, where the flow transitions from supercritical to subcritical (e.g., Long, 1953, 1954; Legg and Klymak, 2008). Supercritical flows are characterized by Froude number ( $Fr = \frac{U}{\sqrt{g/h_0}}$ ) values exceeding unity, i.e., the mean bottom current speed  $U$  exceeds the long-wave phase speed  $\sqrt{g/h_0}$ , where  $g' = g \frac{\rho_2 - \rho_1}{\rho_2}$  is the reduced gravity,  $\rho_2$  is the mean density of the bottom plume,  $\rho_1$  is the density of the fluid that immediately overlies the bottom plume and  $g$  is the gravitational acceleration. Indeed, the time-averaged

Froude number ( $\langle Fr \rangle$ ) in EXP1 and EXP4 shows a transition from supercritical to subcritical consistent with the discontinuity in  $\langle h_0 \rangle$  (Fig. 4.6, black and blue lines on bottom panel). On the other hand,  $\langle Fr \rangle$  remains supercritical throughout the slope in experiment EXP7 (Fig. 4.6, red line on bottom panel).

Since the flow transitions from supercritical to subcritical, it is useful to visualize how kinetic energy is being dissipated in the system. Snapshots of kinetic energy dissipation,  $\varepsilon = \nu_i (\partial u_j / \partial x_i)^2$ , at three different times are shown for experiments EXP1, EXP4 and EXP7 (Figs. 4.7 to 4.9, respectively). All cases display strong, and somehow intermittent, dissipation in both shear instability regions, at the bottom boundary layer and at the interfacial layer between the outflow and the ambient water. However, in experiments EXP1 and EXP4 there is an additional region where a significant amount of kinetic energy is constantly dissipated. This region coincides to where hydraulic jump occurs and the flow transitions from supercritical to subcritical. Once the flow pass through this region, part of the total kinetic energy is converted into potential energy as a consequence of mixing, and intermediate water masses are then generated.

### 4.3.3 Water mass formation

Following Ezer (2005), Legg et al. (2006), and Ezer (2006), we evaluate the water mass formation within the model domain using histograms of tracer distribution as a function of downstream distance from the shelf and density anomaly ( $\delta\rho$ ). The latter is computed with respect to the initial density field at  $t = 0$  hours (i.e.,  $\delta\rho(x, z, t) > 0$  means that at this position and time, the tracer is in water that is heavier than  $\rho(x, z, t = 0)$ ). The histograms were computed by averaging the results over the last 25 hours of simulation, and the percentage of the time-averaged total tracer distribution is calculated.

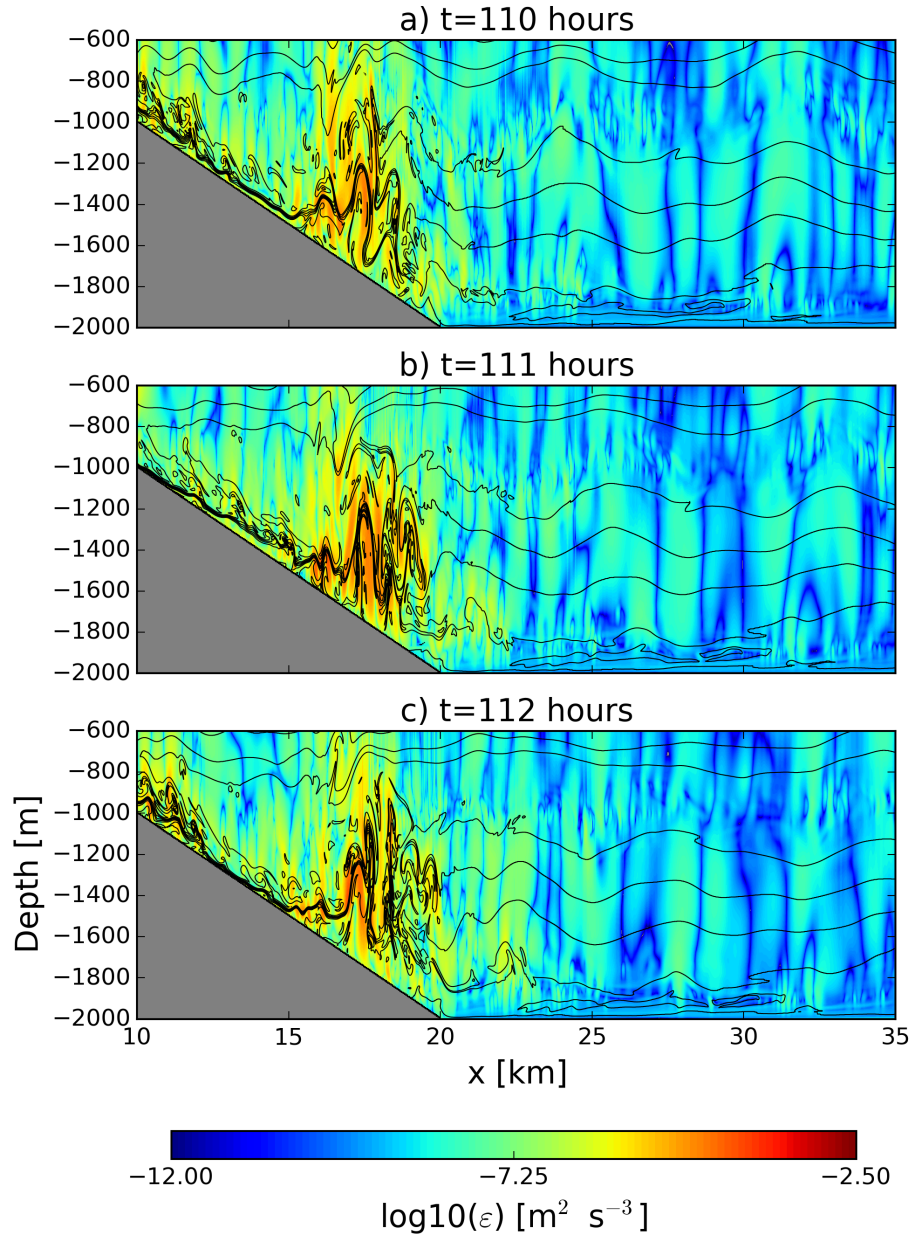


**Figure 4.7:** Snapshots of turbulent kinetic energy dissipation  $\log_{10}(\varepsilon)$  ( $\text{m}^2 \text{ s}^{-3}$ ) and density contours ( $\text{kg m}^{-3}$ , black lines plotted every  $0.02 \text{ kg m}^{-3}$ ) for EXP1 taken at (a)  $t = 110$  hours; (b)  $t = 111$  hours; and (c)  $t = 112$  hours. Note that just a subset of the total domain is shown.

Until  $x \sim 10$  km the pattern is very similar in the three cases and most of the tracer is confined in the dense current (Fig. 4.10). However, in EXP1 (Fig. 4.10a) and

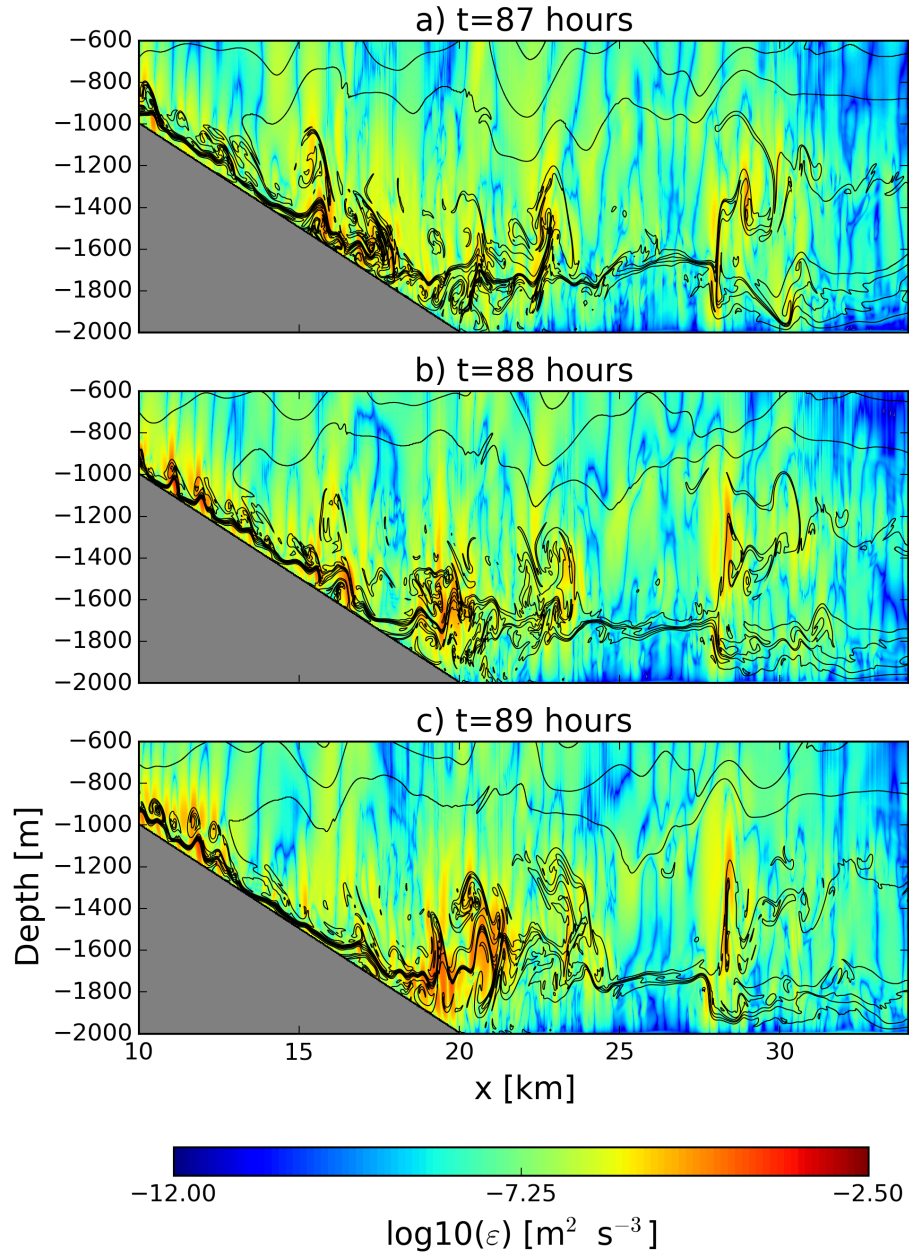


**Figure 4.8:** Same as Fig. 4.7, but for EXP4 at (a)  $t=87$  hours; (b)  $t=88$  hours; and (c)  $t=89$  hours.

EXP4 (Fig. 4.10b), a significant amount of tracer detrains ( $\delta\rho < 0$ ) from the dense current in the lower part of the slope, between  $12 \geq x \geq 20$  km. The amount of tracer associated with less dense water in this region is larger than the values within the dense plume. The region where the less dense water is located was initially (at  $t=0$

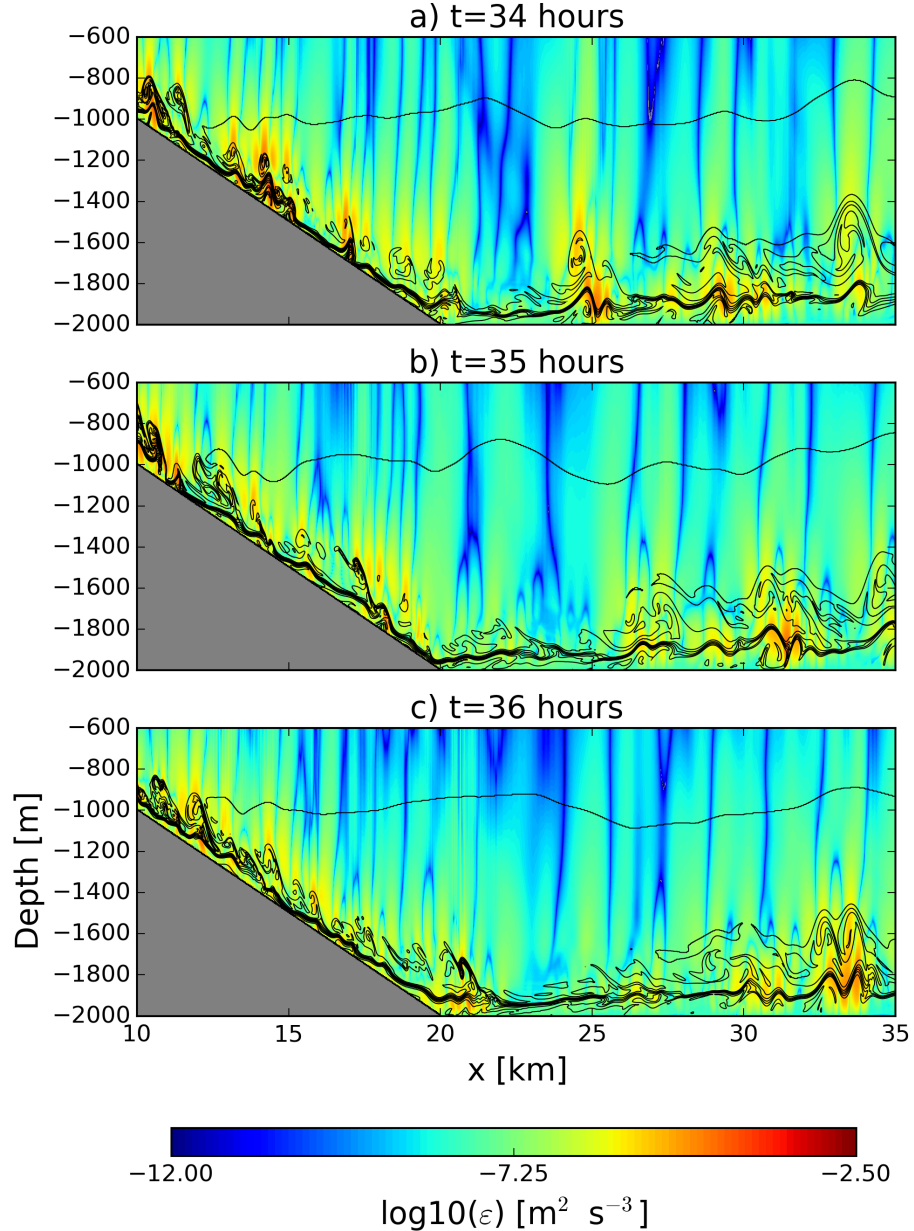


**Figure 4.9:** Same as Fig. 4.7, but for EXP7 at (a)  $t=34$  hours; (b)  $t=35$  hours; and (c)  $t=36$  hours.

hours) occupied by denser water. This is also evident from the isopycnals shown in Figs. 4.5 a and b. Since the density difference between the dense plume and the water just above it has increased, the speed of the flow is also increased. This might help to explain why the flow experiences a hydraulic jump further downstream. On the

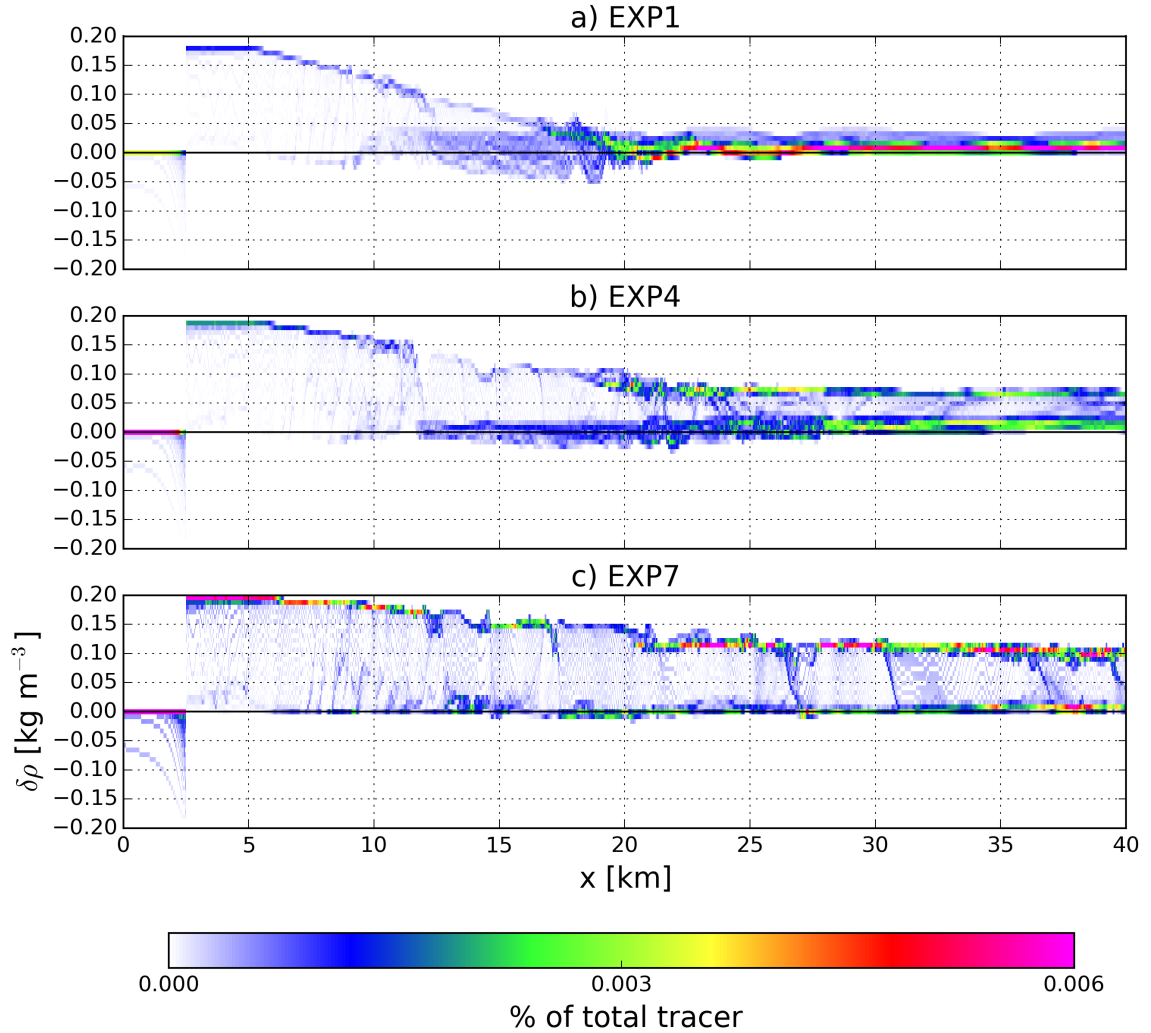


**Figure 4.10:** Time-averaged histograms of total tracer distribution (in %) as a function of downstream distance from the shelf and density anomaly  $\delta\rho$ . The averages were taken over the last 25 hours of simulation and  $\delta\rho$  was computed with respect to the initial density field. (a) EXP1,  $N = 10^{-3} \text{ s}^{-1}$ ; (b) EXP4,  $N = 5 \times 10^{-4} \text{ s}^{-1}$  and (c) EXP7,  $N = 7.5 \times 10^{-4} \text{ s}^{-1}$ .

other hand, in EXP7 most of the tracer within the bottom plume and, in comparison to experiments EXP1 and EXP4, just a small amount of less dense water is formed (Fig. 4.10c).

#### 4.3.4 Slope angle

Laboratory experiments by Baines (2005) show that the bottom slope plays a key role in regulating the mixing regime of downslope flows into stratified environments, where small (steep) slopes have the character of detraining gravity current (entraining plumes). As mentioned earlier, the parameters (i.e., bottom slope and ambient stratification) used in laboratories experiments are much larger than the values observed in the ocean. Therefore, it is useful to verify if the same reasoning applies to the oceanic parameter space employed in our simulations. To this end, we conducted additional simulations using  $\alpha = 0.05$  and  $0.01$ . The same ambient stratification values described earlier were used, resulting in a total of six additional experiments.

Strong ambient stratification ( $1.0 \times 10^{-3} \text{ s}^{-1}$ ) in combination with moderate ( $\alpha=0.05$ , EXP2) and shallow ( $\alpha=0.01$ , EXP3) slopes also result in the double plume condition (Fig.4.11a and Fig.4.12a, respectively). The difference, with respect to the steep slope case (EXP1), is that in both cases the hydraulic jump occurs in the lower part of slope, before the main plume reaches the bottom of the domain ( $x \sim 30$  and  $120$  km, for EXP2 and EXP3, respectively). In addition, once the flow has separated the bottom plume becomes more turbulent as the bottom slope decreases and, therefore, the vertical distance between the plumes decreases as the shelf slope becomes shallower.

Moderate ambient stratification ( $7.5 \times 10^{-4} \text{ s}^{-1}$ ) in combination with moderate slope ( $\alpha=0.05$ , EXP5) results in the double plume regime (Fig. 4.11b). However, the same ambient stratification combined with a shallow slope ( $\alpha=0.01$ , EXP6) results in a single plume (Fig. 4.12b). Lastly, weak ambient stratification ( $5.0 \times 10^{-4} \text{ s}^{-1}$ ) in combination with moderate ( $\alpha=0.05$ , EXP8) and shallow ( $\alpha=0.01$ , EXP9) slopes result in a single plume (Fig.4.11c and Fig.4.12c, respectively).

In summary, the combination of strong ambient stratification with any of the shelf slope values employed here result in the double plume regime. Under moderate ambient stratification, the flow regime is then determined by the shelf slope. The steep ( $\alpha=0.1$ ) and intermediate ( $\alpha=0.05$ ) slopes lead to the double plume regime while the shallow ( $\alpha=0.01$ ) slope leads to the single plume regime. Finally, experiments with weak ambient stratification always resulted in the single plume regime, regardless of the shelf slope values used here.

## 4.4 Flow regimes and application to oceanic out-flows

We follow Baines (2002, 2005, 2008) and compute the buoyancy number  $B = \frac{QN^3}{g'^2}$ , where  $g' = \frac{g\Delta\rho_o}{\rho_0}$  is the reduced gravity and  $\Delta\rho_o$  is the density difference between the outflow and the ambient water above it. Unlike in previous sections, the thickness of the outflow ( $h_0$ ) is defined by the  $\tau = 0.05 \text{ kg m}^{-3}$  contour. We computed  $B$  at  $x = 5 \text{ km}$  in all numerical experiments by averaging  $Q$ ,  $N$  and  $g'$  over the last 25 hours of simulation. The corresponding values are presented in Table 4.2. For comparison, Table 4.2 also shows the parameter values inferred from observations of various oceanic outflows.

It is useful to plot  $B$  versus the bottom slope  $\alpha$  for the model results and observational data shown in Table 4.2 (Fig. 4.13). The boundary between double and single plumes (red and blue squares, respectively) obtained in the numerical simulations is quite clear, and in these experiments  $B$  ranges from  $1.87 \times 10^{-3}$  to  $1.69 \times 10^{-2}$ . Lower  $B$  values result in the single plume regime while higher  $B$  values lead to the double plume regime, regardless of the slope. Intermediate  $B$  values result in the double outflow (single outflow) for steep (shallow) bottom slopes. We also plotted in

**Table 4.2:** Parameter values for the numerical experiments and for various oceanic outflows as described in Section 4.4. The values for oceanic outflows were taken from the field campaigns described in the following publications: Ross Sea: Gordon et al. (2004); Muench et al. (2009a); Mediterranean Sea: Price et al. (1993); Baringer and Price (1997); Red Sea: Peters et al. (2005); Matt and Johns (2007); Weddell Sea: Foldvik et al. (2004); Denmark Straits: Girton and Sanford (2003).

Experiments	Q (m <sup>2</sup> s <sup>-1</sup> )	g' (m s <sup>-2</sup> )	N (s <sup>-1</sup> )	B	$\alpha=\tan(\theta)$
EXP1	50.2	$1.7 \times 10^{-3}$	$1.0 \times 10^{-3}$	$1.69 \times 10^{-2}$	0.1
EXP2	49.7	$1.7 \times 10^{-3}$	$1.0 \times 10^{-3}$	$1.63 \times 10^{-2}$	0.05
EXP3	51.3	$1.7 \times 10^{-3}$	$1.0 \times 10^{-3}$	$1.67 \times 10^{-2}$	0.01
EXP4	51.5	$1.8 \times 10^{-3}$	$7.5 \times 10^{-4}$	$6.59 \times 10^{-3}$	0.1
EXP5	50.4	$1.8 \times 10^{-3}$	$7.5 \times 10^{-4}$	$6.47 \times 10^{-3}$	0.05
EXP6	50.7	$1.8 \times 10^{-3}$	$7.5 \times 10^{-4}$	$6.53 \times 10^{-3}$	0.01
EXP7	51.7	$1.8 \times 10^{-3}$	$5.0 \times 10^{-4}$	$1.90 \times 10^{-3}$	0.1
EXP8	52.3	$1.8 \times 10^{-3}$	$5.0 \times 10^{-4}$	$1.92 \times 10^{-3}$	0.05
EXP9	51.5	$1.9 \times 10^{-3}$	$5.0 \times 10^{-4}$	$1.87 \times 10^{-3}$	0.01
Location					
Ross Sea	150	$2 \times 10^{-3}$	$7.0 \times 10^{-4}$	$1.3 \times 10^{-2}$	0.11
Mediterranean Sea	200	$1.6 \times 10^{-3}$	$2.0 \times 10^{-3}$	$7.2 \times 10^{-1}$	0.15
Red Sea	55	$1.4 \times 10^{-2}$	$7.0 \times 10^{-3}$	$9.6 \times 10^{-2}$	0.004
Weddell Sea	100	$2 \times 10^{-3}$	$7.0 \times 10^{-4}$	$9.0 \times 10^{-3}$	0.03
Denmark Straits	140	$2 \times 10^{-3}$	$1.3 \times 10^{-3}$	$7.7 \times 10^{-2}$	0.03

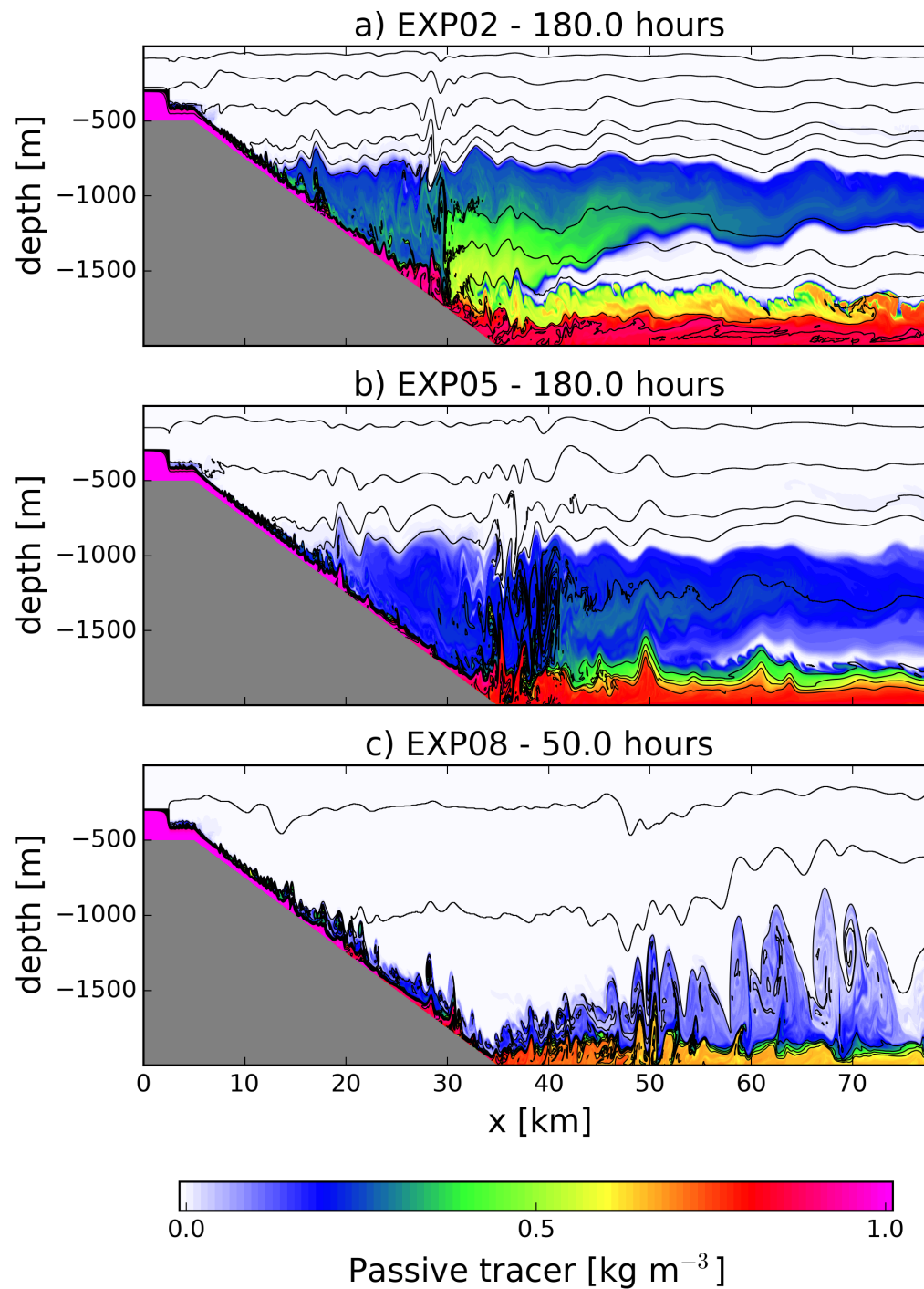


**Figure 4.11:** Similar to Fig. 4.5, but for experiments where the shelf slope is  $s = 0.05$ .

(a) EXP2 at  $t = 180$  hours; (b) EXP5 at  $t = 180$  hours and (c) EXP8 at  $t = 50$  hours.

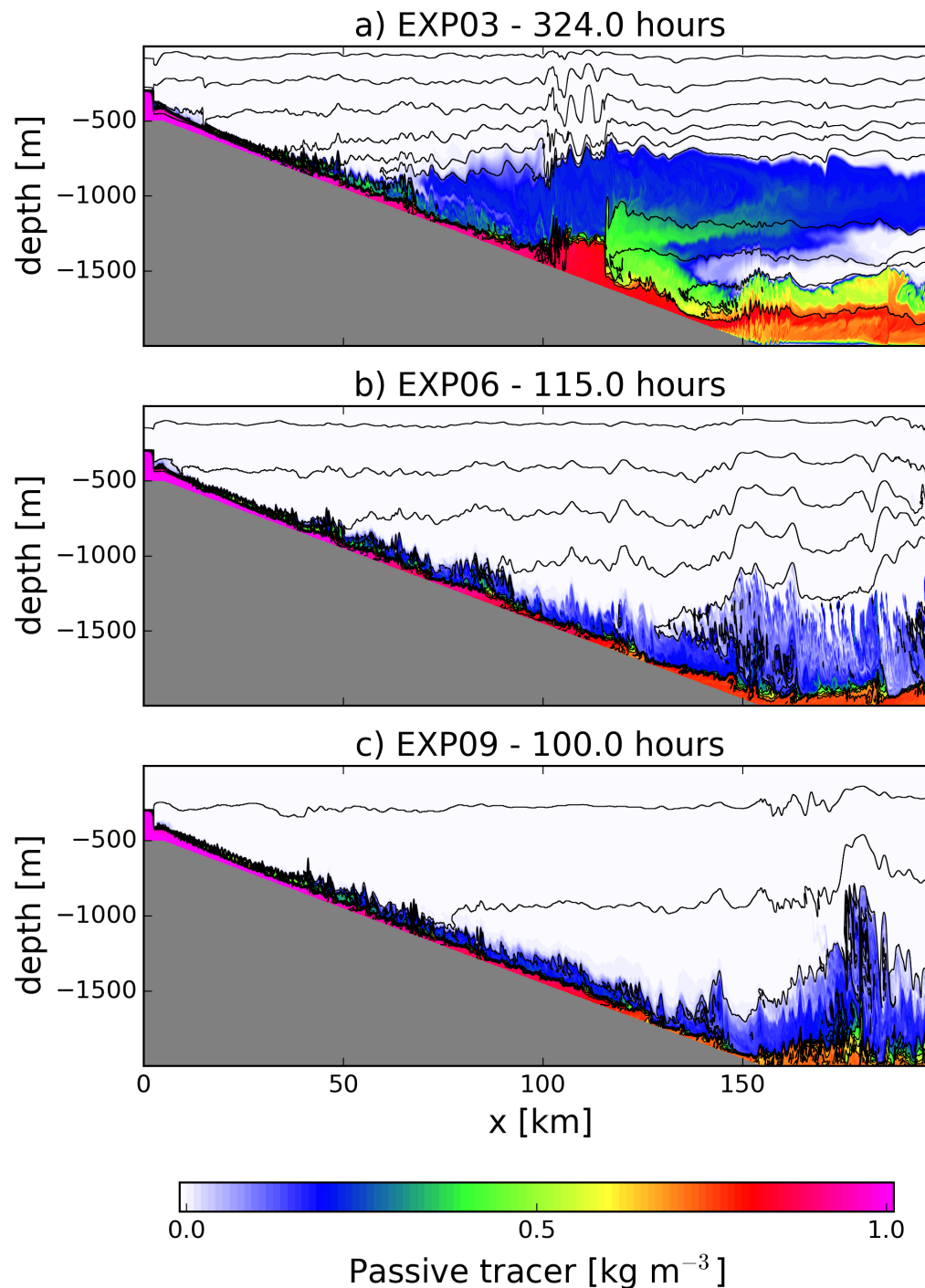


**Figure 4.12:** Similar to Fig. 4.5, but for experiments where the shelf slope is  $\alpha = 0.01$ .

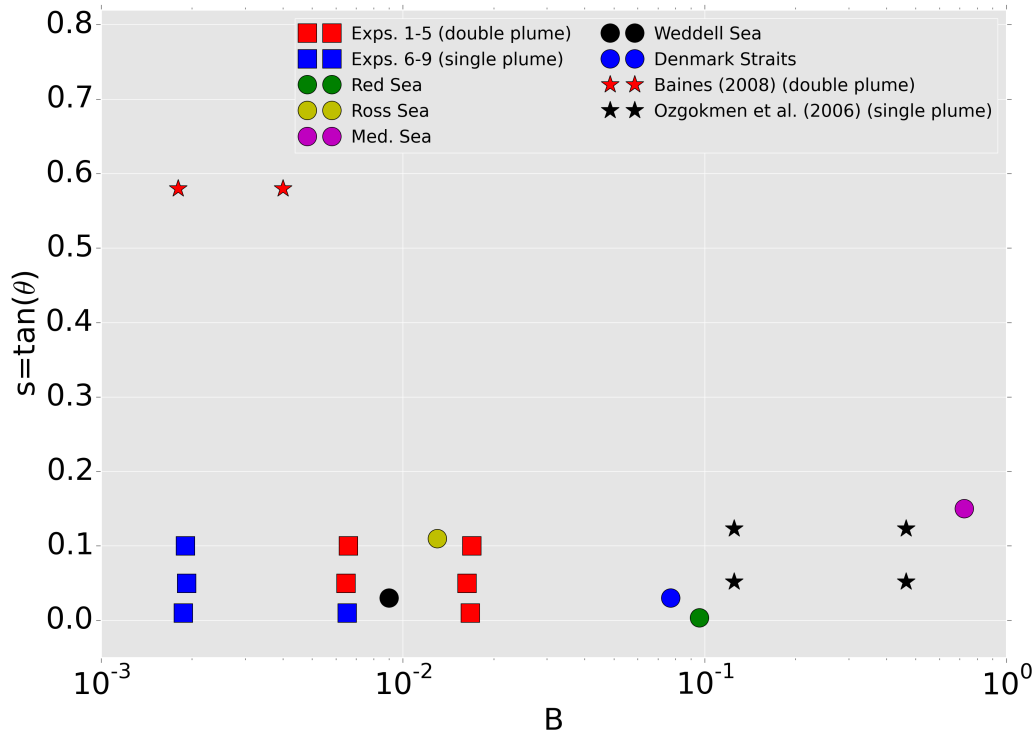
(a) EXP3 at  $t = 268$  hours; (b) EXP6 at  $t = 115$  hours and (c) EXP9 at  $t = 100$  hours

Fig. 4.13 the range of values from the numerical experiments conducted by Özgökmen et al. (2006) (black stars). The strong ambient stratification applied in their cases resulted in  $B$  values between  $1.25 \times 10^{-1}$  and  $4.65 \times 10^{-1}$  while  $s$  varied between 0.05 and 0.12. All the experiments presented by Özgökmen et al. (2006) resulted in a single plume that equilibrated at intermediate depths (i.e., the neutral buoyancy level was achieved before the plumes reached the bottom of the domain). The reason why a single plume is also generated at larger  $B$  values is not clear. Perhaps it is related to numerical parameters (e.g., grid resolution) and/or initial and boundary conditions, but this requires further investigation.

The  $B$  values derived from observations of oceanic outflows are between  $9.0 \times 10^{-3}$  and  $7.2 \times 10^{-1}$ . The parameters estimated for the Ross and Weddell Sea outflows (yellow and black circles) fall in the range of the numerical experiments that resulted in a double plume regime, while the values for the Red Sea, Mediterranean Sea and Denmark Straits outflows (green, magenta and blue circles, respectively) are closer to the values obtained by Özgökmen et al. (2006). None of the estimates from oceanic outflow observations fall within the low  $B$  values range (blue squares) obtained in experiments # 6 to 9.

Finally, results from two laboratory experiments presented by Baines (2008) and that resulted in a double plume pattern are also plotted in Fig. ??4.13Fig. 4.13 starts). The values in the latter differ from the range obtained from the numerical simulations that generated a double plume. It is well known that laboratory experiments must be configured using slope much larger than those observed in nature. Otherwise the dense water cannot accelerate within the bounds of typical laboratory tanks [ $O(1\text{ m})$ ] and the flow does not exhibit a turbulent behavior. In addition, the ambient stratification frequency used in the laboratory experiments conducted by (Baines, 2008) were at least two orders of magnitude larger than the typical values next to

the major oceanic outflows (see Table 1 in Baines (2008)). Therefore, we conclude that the flow regime criteria obtained in laboratory experiments of dense fluid down slope and into stratified environments differ from that obtained under geophysical parameters and scales. Based on our results and using observation taken in the Ross and Weddell Sea, we hypothesize that double plumes around Antarctica could carry water properties from the shelf into the deep ocean at two distinct depths.



**Figure 4.13:** Buoyancy number  $B$  versus shelf slope  $\alpha=\tan(\theta)$  for all numerical experiments conducted here. Experiments that generated a double plume pattern are shown by the red squares while experiments that result in a single plume are shown by the blue squares (see Table 4.2 for the parameter values). Also shown are the values for various oceanic outflows inferred from available observations (circles, see Table 4.2 for additional information) and the results from the numerical simulations of Özgökmen et al. (2006) (black stars). The red stars show the values for the laboratory experiments discussed by Baines (2008) that resulted in double plume.

## 4.5 Summary

Laboratory experiments of dense water flowing down slopes and into stratified environments have revealed that, under a very limited parameter space, the main flow can be split into two plumes and generated the so-called double plume regime (see Fig.1; Baines, 2008). Motivated by observational evidence that the signature of Antarctic dense shelf water appears in both bottom water and intermediate depth intrusions (Carmack and Killworth, 1978), this study investigated whether the double plume regime can be generated in two-dimensional numerical simulations of oceanic outflows.

A series of high resolution numerical experiments were conducted using the Massachusetts Institute of Technology general circulation model (MITgcm). This model was configured to solve the nonhydrostatic Boussinesq equations in a two-dimensional configuration without rotation. Dense water was released (via nudging) on the top of a flat continental shelf that is connected to the deep ocean through a constant bottom slope. A passive tracer was injected with the dense water to help visualizing the flow. A total of nine experiments were conducted, consisting of three different slopes ( $\alpha=0.1$ , 0.05 and 0.01) and three different constant ambient stratification frequency ( $N = 1.0 \times 10^{-3}$ ,  $7.5 \times 10^{-4}$  and  $5.0 \times 10^{-4} \text{ s}^{-1}$ ).

The numerical simulations presented in this study are the first indication that the double plume regime may occur in oceanic environments, such as the Antarctic outflows. The parameters needed to identify the flow regimes are  $\alpha$  and the buoyancy number ( $B$ ) proposed by Baines (2001, 2005, 2008). Regardless of the bottom slopes tested here, the double plume regime occurred when  $B \sim 0.02$ . When  $B$  was about one order of magnitude smaller ( $\sim 0.002$ ), a single plume was always observed. For intermediate  $B$  values ( $B \sim 0.007$ ), a double plume regime occurred for steeper slopes ( $\alpha=0.1$  and  $\alpha=0.05$ ) and a single plume occurred for the shallower slope ( $\alpha=0.01$ ).

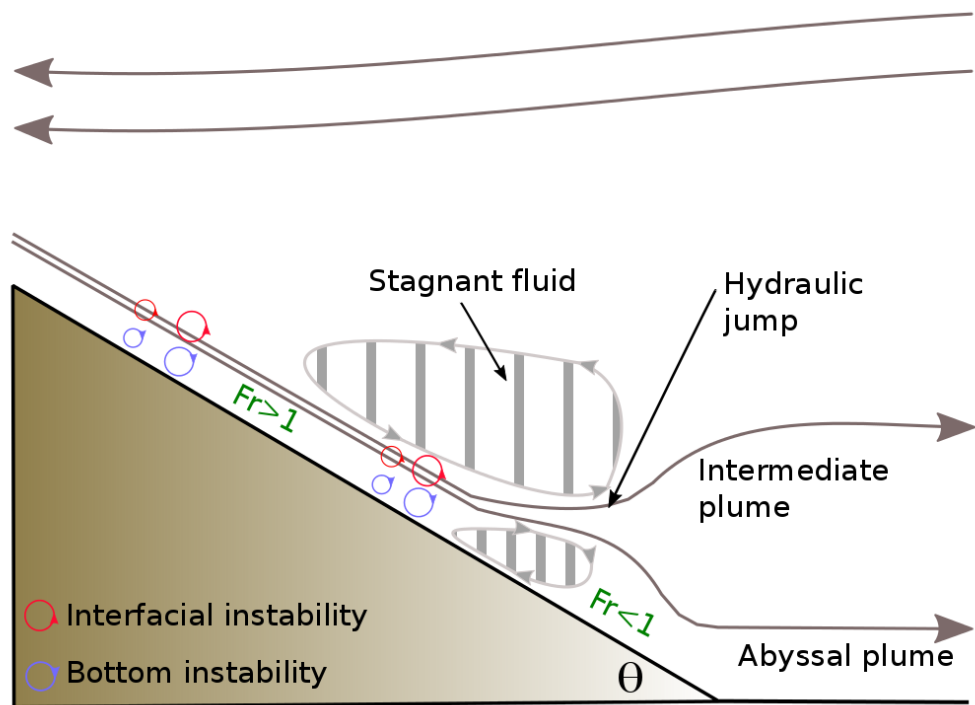


**Figure 4.14:** Schematic depiction of the processes occurring in the double plume regime.

The overall flow characteristics in the double plume regime is depicted in Fig. 4.14. The dense plume is initially mixed with ambient water as a consequence of shear-generated Kelvin-Helmholtz billows at the top boundary of the outflow (red circles in Fig. 4.14). This process results in a fluid with intermediate density between the dense plume and the ambient water. Soon after, this newly formed fluid becomes neutrally buoyant relative to the environment and no longer experiences downslope acceleration. This water then detrains from the main plume and forms a “pool” of stagnant homogeneous fluid sitting on the top of the bottom current. Meanwhile, shear-induced instabilities in the bottom boundary layer act as sink of kinetic energy and just homogenize the dense plume, i.e., they have less effect on mixing of density than the Kelvin-Helmholtz billows. As the dense plume decelerates, the fluid transitions from a supercritical condition ( $Fr > 1$ ) to a slower and more uniform

subcritical condition ( $Fr < 1$ ). This transition results in an internal hydraulic jump, where kinetic energy is converted into potential energy as a consequence of strong mixing and intermediate water masses are then generated. The fluid in the bottom boundary layer undergoes little dilution and results in a denser plume sitting at the bottom.

# Chapter 5

## Conclusions

Oceanic outflows play an important role in the formation of deep and intermediate water masses and, therefore, contribute to the establishment of the meridional overturning circulation (MOC). Antarctic outflows are particularly important, since they lead to the formation of Antarctic Bottom Water, the most voluminous bottom water of the world ocean. The success of climate predictions for any given time relies on how accurate ocean models represent the MOC. Since it is not likely that these models will be able to explicitly resolve small-scale outflow processes in the near future, parameterizations of such processes must be developed and then incorporated into ocean models. The main goal of this dissertation has been to advance the understanding of the processes associated with oceanic outflows, focusing on the outflows of dense shelf water in Antarctica. The results presented here provide new insights on how to improve future observational and modeling efforts of Antarctic outflows, and perhaps other oceanic outflows. The most important conclusions from the studies performed in this dissertation are summarized next.

In Chapter 2, a series of numerical simulations for two idealized problems was performed. The lock-exchange (LE) problem, which is a simple computational setting with low-aspect domain ratio and no ambient rotation, was used to study the

temporal evolution of mixing in a stratified fluid. The mixed-layer instability (MLI) problem, which is very similar to the LE problem in terms of the computational setting, but differs dynamically due to the presence of ambient rotation and a high-aspect domain ratio, was used to study the transport and stirring of a passive tracer due to submesoscale eddies. This study attempted to quantify how the mixing and stirring in OGCMs is affected by common modeling choices, namely spatial resolution, tracer advection schemes, Reynolds number and turbulence closure schemes. Although this study was not directly related to oceanic outflows, it provided useful guidance on the setup of the numerical experiments designed to investigate buoyancy driven flows in general, including oceanic outflows. Two modeling approaches were applied: an OGCM (ROMS) that solves the hydrostatic primitive equations; and a spectral element model (Nek5000) that integrates the nonhydrostatic Boussinesq equations. The latter was used to perform large eddy simulations (LES) for the two idealized problems, and these results were treated as the optimum solution.

In the LE problem, the effects of various modeling parameters were explored and it was found that, for a fixed horizontal Reynolds number ( $Re_H=10^3$ ), mixing was most sensitive to the choice of grid resolution. No convergence towards the optimum solution (LES) was attained as the grid resolution was refined and the best results were achieved using an intermediate spatial resolution. Mixing was underestimated (overestimated) when using a finer (coarser) spatial resolution. The results showed the importance of using a tracer advection scheme that preserves the initial extrema in numerical studies dealing with small-scale stratified mixing. Advection schemes that did not preserve the initial tracer extrema resulted in the generation of unrealistic water masses, which led to excessive mixing when compared to the ground truth experiment. Note that a correct representation of the LE problem is a challenging task for any advection scheme available in OGCMs, since it includes sharp gradients

in the velocity and density fields as well as non-hydrostatic dynamics. Therefore, one cannot expect the solutions to converge following the order of the numerical scheme, as is the case for classical convergence analysis for smooth solutions. Given that the results are largely influenced by the errors associated with the numerical schemes, it is not possible to find a scaling to predict an optimal resolution *a priori*.

The sensitivity of the transport and stirring of a passive tracer field was then studied within the context of submesoscale eddies generated by surface density fronts (i.e., the MLI problem). As in the LE problem, the results did not converge towards the reference nonhydrostatic LES solution when the grid resolution was refined. However, for this problem the choice of turbulence closure had more impact on the stirring of a passive tracer field than any other modeling choice investigated here. The best results with respect to the LES were achieved when using a second-order turbulence closure ( $k-\epsilon/CA$ ), which resulted in an accurate representation of the restratification in the mixed layer. The widely used Richardson number based KPP scheme yielded low vertical diffusivities and, therefore, the restratification in the mixed layer was poorly represented.

While ROMS simulations differed from LES in the amount of mixing and tracer stirring, the simulated coherent features were quite similar. However, although the metrics used for comparison are quite precise and perhaps can only be implemented in a model to model comparison, they could be too challenging to compute from ocean observations. Therefore, different types of metrics should be applied when comparing models with observations. It is unclear how much of the differences between the models were related to nonhydrostatic effects, as the MLI is still under rotational control and ROMS simulations showed considerable variability with different parameterizations. Processes at the next range of scales, namely those between the rotationally-controlled MLI and three-dimensional stratified turbulence, such as

Langmuir turbulence, diurnal convection in the mixed layer and inertia gravity waves are expected to contain significant nonhydrostatic dynamics. Future studies should address whether these processes might pose a natural resolution limit to the applicability of hydrostatic dynamics. Furthermore, the impact of both the hydrostatic approximation and the different modeling choices in OGCMs on the dispersive characteristic of the flow remain to be quantified. Given the fact that multi-scale problems are ubiquitous in oceanography, the most logical choice is for OGCMs to start adopting nonhydrostatic pressure solvers, high-order advection schemes (where the associated numerical diffusion will not act as an implicit closure) and SGS parameterizations that depend explicitly on the resolution of the model. There should also be a much more careful evaluation of the latter. There are certainly several attempts in that direction (e.g., Marshall et al., 1998; Fringer et al., 2006; Kanarska et al., 2007; Piggott et al., 2008), even though the pace of change is still dictated by the computational constraints and sparse observational data sets for accurate evaluation.

In Chapter 3 we investigated the connection between Antarctic outflows and topographic vorticity waves (TVWs). The goals of this study were to 1) investigate whether the outflows of Dense Shelf Water (DSW) through troughs around Antarctica can trigger TVWs, and 2) if so, identify the main parameters controlling the properties of these waves and investigate how they affect their dispersion relation. A set of fourteen idealized numerical experiments were performed by varying the following parameters: horizontal grid resolution, continental shelf slope ( $\alpha$ ), density difference between the outflow and the ambient water ( $\Delta\rho$ ), and the strength of the background westward along-slope flow representing the Antarctic Slope Current. All experiments were configured with homogeneous initial ambient water, which is a reasonable simplification for Antarctic environments where the vertical variations in density are usually small. In addition, a realistic model configured for the Ross Sea

was used in the analysis. The latter included a sea ice component and was forced by a mesoscale atmospheric forecast model.

Both idealized and realistic numerical simulations showed that TVWs can be triggered along the Antarctic continental slope by the outflows of DSW through troughs. The modeled cross-slope currents associated with the TVWs often exceed  $0.2 \text{ m s}^{-1}$ , suggesting that TVWs could contribute to mixing and cross-slope advection in the vicinity of troughs. These are regions of important cross-slope exchanges – outflows of DSW leading to AABW production and inflows of heat onto the continental shelf and south to the ice shelves – implying that our ability to represent these exchanges depends on accurate models of TVW production, propagation and dissipation.

For most of the idealized simulations, the energy flux of the TVWs was eastward from the trough, opposing the westward transport of the dense outflow and the TVWs' phase propagation. Westward TVW energy flux only occurred when the ambient westward along-slope flow was sufficiently strong. The period of these waves is a function of the stretching parameter  $\Gamma = \frac{R_d\alpha}{D}$ , where  $R_d = \sqrt{\Delta\rho/\rho_0gh_0}/f$  is the baroclinic radius of deformation,  $D$  is the depth above the bottom density current,  $g$  is the acceleration due to gravity,  $\rho_0$  is the reference density,  $h_0$  is thickness of the bottom density current and  $f$  is the Coriolis parameter. Wave frequency increases as  $\Gamma$  decreases, implying that higher frequency waves will be generated when  $\alpha$  is steeper and when  $\Delta\rho$  is increased. In addition, the numerical experiments showed that stronger mean westward along-slope flows, representing the Antarctic Slope Current, reduced the wave period.

The changes in TVW properties in both idealized and realistic simulations were consistent with the observed variability along the southern Weddell Sea continental slope near the Filchner Trough outflow reported by Jensen et al. (2013). The results from the realistic Ross Sea model showed a strong time-dependence of the TVW

energy east of Drygalski and Glomar Challenger troughs, correlated with seasonal variability of DSW properties and along-slope mean flow. However, the isolated effect of these changes were not investigated with the realistic model. Although the idealized experiments confirmed that the TVWs depend on the DSW properties (i.e.,  $\Delta\rho$ ), the influence of changing  $\Delta\rho$  on  $\Gamma$  is not as significant as are changes in either  $\alpha$  or  $D$ . For example, to increase the baroclinic radius of deformation by a factor of two,  $\Delta\rho$  would have to increase by a factor of four. This means that small changes in the DSW properties along the Antarctic continental shelf, due to for example increased ice-shelf melting, may not significantly affect the properties of the TVWs.

Previous studies have shown that tides can also generate TVWs with diurnal frequencies in the shelf break regions around Antarctica (Middleton et al., 1987). In addition, tides have a significant impact on the outflow of DSW at particular locations, such as the Drygalski Trough in the Ross Sea (Padman et al., 2009). Therefore, the combined effects of tides and outflows on the generation of TVWs should be addressed in future works. The sensitivity of TVWs generated by outflows to the strength of the ambient stratification frequency ( $N$ ) also remains to be investigated. This will be particularly relevant for oceanic outflows that equilibrate at intermediate depths; i.e., where vertical gradients in background density are significant relative to the density of the outflow. For those situations where background  $N$  is large, the stretching parameter  $\Gamma$  discussed in the present study will not be valid. A modified version of  $\Gamma$  that accounts for the effects of  $N$  has been proposed based on laboratory experiments (Lane-Serff and Baines, 2000), and should provide a starting point for future studies.

In conclusion, TVWs generated by DSW outflows from Antarctic shelf seas play a role in processes linking the circulation of the deep Southern Ocean to continental shelf processes including southward heat advection, sea-ice and DSW formation, and ice-shelf mass loss through basal melting. Furthermore, since cross-slope advection

and mixing by TVWs contributes to the background state in which the TVWs are generated and propagate, the effect of these waves cannot be simply parameterized in OGCMs as an added source of kinetic energy. Instead, feedbacks between the TVWs and the background state are expected, requiring explicit representation of these processes in models representing the role of Antarctic shelf seas in the global climate system.

Finally, in Chapter 4, a series of high resolution numerical experiments were conducted to address the question of whether a single outflow can simultaneously delivers water to both the deep benthic ocean and intermediate layers. The numerical model used (MITgcm) was configured to solve the nonhydrostatic Boussinesq equations in a two-dimensional configuration without rotation. Dense water was released on the top of a flat continental shelf that is connected to the deep ocean through a constant bottom slope. A passive tracer was injected with the dense water to help visualize the flow. A total of nine experiments were conducted, consisting of three different slopes ( $\alpha=0.1$ , 0.05 and 0.01) and three different values of constant ambient stratification frequency ( $N = 1.0 \times 10^{-3}$ ,  $7.5 \times 10^{-4}$  and  $5.0 \times 10^{-4} \text{ s}^{-1}$ ).

The numerical simulations presented in this study are the first evidence that the double plume regime may occur in oceanic outflows. The overall flow characteristics in this regime were as follows. First, the dense plume is mixed with ambient water as a consequence of shear-generated Kelvin-Helmholtz billows at the top boundary of the outflow. This process results in a fluid with intermediate density between the dense plume and the ambient water. Soon after, this newly formed fluid becomes neutrally buoyant relative to the environment and no longer experiences downslope acceleration. This water then detrains from the main plume and forms a “pool” of homogeneous fluid sitting on the top of the bottom current. Meanwhile, shear-induced instabilities in the bottom boundary layer act as sink of kinetic energy and

just homogenize the dense plume, i.e., they have less effect on mixing of density than the Kelvin-Helmholtz billows. As the dense plume decelerates, the fluid transitions from a supercritical condition, where the Froude number ( $Fr$ ) is greater than one, to a slower and more uniform subcritical condition ( $Fr < 1$ ). This transition results in an internal hydraulic jump, where mixing is very strong. Offshore of the jump, the flow splits into two plumes: one denser (less diluted) at the bottom, and one less dense (more diluted due to mixing) detraining at intermediate depths. If the system is integrated for enough time, the final state in the abyssal region is a very thick and continuous plume (e.g., similar to the scenario shown in Fig. 4.4 at  $x \sim 25$  km). This final condition should be relatively easy to parameterize in OGCMs and coupled climate models. Future parameterizations should be considered in the form of a stream tube model (e.g.; Smith, 1975; Price and Yang, 1998), given that this type of model has already been incorporated into climate models (Danabasoglu et al., 2010).

Based on Baines (2001, 2005, 2008), the parameters needed to identify the flow regimes are  $\alpha$  and the buoyancy number  $B = \frac{QN^3}{g\ell^2}$ , where  $Q$  is the cross-slope transport per unit width,  $g\ell = \frac{g\Delta\rho_o}{\rho_0}$  is the reduced gravity and  $\Delta\rho_o$  is the density difference between the outflow and the ambient water above it. Regardless of the bottom slopes tested here, the double plume regime occurred when  $B \sim 0.02$ , while in the experiments where a single plume was observed  $B$  was approximately one order of magnitude smaller. For an intermediate buoyancy number  $B \sim 0.007$ , a double plume occurred for steeper slopes ( $\alpha=0.1$  and  $0.05$ ) and a single plume occurred for the shallower slope ( $\alpha=0.01$ ). Based on our results and using the parameters derived from observations, the Weddell and Ross Sea outflows fall within the double plume regime, assuming that rotation is not important.

In most oceanic outflows, however, rotation and along-slope flow variations (i.e., three-dimensionality) are important. Therefore, future research is needed to confirm the outcomes of this study. This will perhaps require a combination of theoretical analysis with high-resolution three-dimensional simulations. It is known that shear instabilities generated in similar two-dimensional numerical simulations, but with homogeneous ambient water, are overestimated when compared to equivalent laboratory experiments (Özgökmen and Chassignet, 2002). This is due to the two-dimensional nature of the flow, which does not allow for lateral spreading and widening of the current as it flows downslope. We therefore hypothesize that, in the presence of ambient stratification, the importance of these instabilities will be also overestimated. Whether internal hydraulic jumps and the consequent double-plume pattern will occur under this condition remains to be investigated.

In summary, the studies presented in this dissertation have significantly improved our understanding of processes that affect cross-slope exchanges along the Antarctic continental margins. We have identified two new processes – topographic vorticity waves and double plume formation – that may influence the properties of dense and intermediate waters that enter the Southern Ocean around Antarctica. These processes depend on two unique characteristics of Antarctic environments: weak ambient stratification ( $N \sim 7 \times 10^{-4} \text{ s}^{-1}$ ) and steep shelf slopes ( $\alpha > 0.05$ ). These studies have also identified important requirements for numerical models to be able to represent water mass exchange and production processes around Antarctica. The very small spatial and temporal scales associated with important processes in this region prohibits their representation in the current generation of OGCMs and coupled climate models. Although several parameterizations for the entrainment in oceanic outflows have been developed (e.g., Smith, 1975; Turner, 1986; Price and Yang, 1998; Xu et al., 2006; Cenedese and Adduce, 2010; Danabasoglu et al., 2010), none of them take into

account neither  $\Gamma$  nor  $B$ . As shown in this dissertation, these parameters have some diagnostic value for predicting the characteristics of Antarctic outflows. Therefore, future work should focus on how to incorporate  $\Gamma$  and  $B$  into parameterizations of oceanic outflows.

# References

- Adcroft, A., C. Hill, and J. Marshall, 1997: Representation of topography by shaved cells in a height coordinate ocean model. *Monthly Weather Review*, **125** (9), 2293–2315. 85
- Baines, P. G., 2001: Mixing in flows down gentle slopes into stratified environments. *Journal of Fluid Mechanics*, **443**, 237–270. 83, 109, 119
- Baines, P. G., 2002: Two-dimensional plumes in stratified environments. *Journal of Fluid Mechanics*, **471**, 315–337. 84, 103
- Baines, P. G., 2005: Mixing regimes for the flow of dense fluid down slopes into stratified environments. *Journal of Fluid Mechanics*, **538**, 245–267. 5, 83, 84, 93, 102, 103, 109, 119
- Baines, P. G., 2008: Mixing in downslope flows in the ocean-plumes versus gravity currents. *Atmosphere-ocean*, **46** (4), 405–419. xiv, xvi, 5, 11, 81, 82, 83, 84, 93, 103, 107, 108, 109, 119
- Bairinger, M. and J. Price, 1997: Mixing and spreading of the Mediterranean outflow. *J. Phys. Oceanogr.*, **27** (8), 1654–1677. xviii, 4, 104
- Baumert, H. and H. Peters, 2004: Turbulence closure, steady state, and collapse into waves. *J. Phys. Oceanogr.*, **34** (2), 505–512. 14
- Baumert, H. Z., J. Simpson, and J. Sündermann, 2005: *Marine turbulence: theories, observations, and models*, Vol. 1. Cambridge University Press. 14
- Beckmann, A. and D. B. Haidvogel, 1993: Numerical simulation of flow around a tall isolated seamount. part i: problem formulation and model accuracy. *J. Phys. Oceanogr.*, **23** (8), 1736–1753. 63
- Bergamasco, A., V. Defendi, E. Zambianchi, and G. Spezie, 2003: Evidence of dense water overflow on the Ross Sea shelf-break. *Antarctic Science*, **14** (03), 271–277. 7
- Berselli, L. C., P. F. Fischer, T. Iliescu, and T. M. Özgökmen, 2011: Horizontal large eddy simulation of stratified mixing in a lock-exchange system. *Journal of Scientific Computing*, **49** (1), 3–20. 15

- Boccaletti, G., R. Ferrari, and B. Fox-Kemper, 2007: Mixed layer instabilities and restratification. *J. Phys. Oceanogr.*, **37** (9), 2228–2250. 15, 47
- Botelho, D., J. Imberger, C. Dallimore, and B. Hodges, 2009: A hydrostatic/non-hydrostatic grid-switching strategy for computing high-frequency, high wave number motions embedded in geophysical flows. *Env. Modelling & Software*, **24**, 473–488. 15
- Bower, A. S., W. E. Johns, D. M. Fratantoni, and H. Peters, 2005: Equilibration and circulation of red sea outflow water in the western gulf of aden\*. *J. Phys. Oceanogr.*, **35** (11), 1963–1985. 4
- Boyd, J. P., 2001: *Chebyshev and Fourier spectral methods*. Courier Dover Publications. 17
- Brink, K. H., 2006: Coastal-trapped waves with finite bottom friction. *Dyn. Atmos. Oceans*, **41** (3), 172–190. 69, 73
- Broecker, W. S., et al., 1998: How much deep water is formed in the southern ocean? *J. Geophys. Res.*, **103** (C8), 15 833–15 843. 1
- Bromwich, D. H., A. J. Monaghan, K. W. Manning, and J. G. Powers, 2005: Real-Time forecasting for the Antarctic: an evaluation of the Antarctic mesoscale prediction system (AMPS)\*. *Mon. Weather Rev.*, **133** (3), 579–603. 72
- Budgell, W., 2005: Numerical simulation of ice-ocean variability in the Barents Sea region. *Ocean Dynamics*, **55** (3-4), 370–387. 72
- Budillon, G., P. Castagno, S. Aliani, G. Spezie, and L. Padman, 2011: Thermohaline variability and Antarctic bottom water formation at the Ross Sea shelf break. *Deep Sea Res. Part I*, **58** (10), 1002–1018. 6, 7, 72
- Burchard, H. and H. Baumert, 1995a: On the performance of a mixed-layer model based on the  $k - \varepsilon$  turbulence closure. *J. Geophys. Res.*, **100**, 8523–8540. 14, 27
- Burchard, H. and H. Baumert, 1995b: On the performance of a mixed-layer model based on the  $\kappa-\epsilon$  turbulence closure. *J. Geophys. Res.*, **100** (C5), 8523–8540. 66
- Burchard, H. and K. Bolding, 2001: Comparative analysis of four second-moment turbulence closure models for the oceanic mixed layer. *J. Phys. Oceanogr.*, **31**, 1943–1968. 14
- Calil, P. H. R. and K. J. Richards, 2010: Transient upwelling hot spots in the oligotrophic North Pacific. *J. Geophys. Res.*, **115** (C2), 1–20. 16
- Campin, J.-M., C. Hill, H. Jones, and J. Marshall, 2010: Super-parameterization in ocean modeling: application to deep convection. *Ocean Modelling*, **36**, 90–101. 15

- Canuto, V., Y. Cheng, and A. Howard, 2007: Non-local ocean mixing mode and a new plume model for deep convection. *Ocean Modelling*, **16**, 28–46. 14
- Canuto, V., A. Howard, Y. Cheng, and M. Dubovikov, 2001: Ocean turbulence. Part I: One-point closure model-momentum and heat vertical diffusivities. *J. Phys. Oceanogr.*, **31**, 1413–1426. 14, 27, 66
- Capet, X., J. C. McWilliams, M. J. Molemaker, and a. F. Shchepetkin, 2008: Mesoscale to submesoscale transition in the California current system. Part I: flow structure, eddy flux, and observational tests. *J. Phys. Oceanogr.*, **38** (1), 29–43. 12, 16
- Carmack, E. C. and P. D. Killworth, 1978: Formation and interleaving of abyssal water masses off Wilkes Land, Antarctica. *Deep Sea Research*, **25** (4), 357–369. 5, 10, 109
- Cenedese, C. and C. Adduce, 2010: A new parameterization for entrainment in overflows. *J. Phys. Oceanogr.*, **40** (8), 1835–1850. 120
- Cenedese, C., J. A. Whitehead, T. Ascarelli, and M. Ohiwa, 2004: A dense current flowing down a sloping bottom in a rotating fluid. *J. Phys. Oceanogr.*, **34** (1), 188–203. 74, 75, 83
- Cerovečki, I., R. A. Plumb, and W. Heres, 2009: Eddy transport and mixing in a wind-and buoyancy-driven jet on the sphere. *J. Phys. Oceanogr.*, **39** (5), 1133–1149. 55
- Chang, Y., Z. Garraffo, H. Peters, and T. Özgökmen, 2009: Pathways of Nordic overflows from climate model scale and eddy resolving simulations. *Ocean Modelling*, **29**, 66–84. 3
- Chang, Y. S., T. M. Özgökmen, H. Peters, and X. Xu, 2008: Numerical simulation of the Red Sea outflow using HYCOM and comparison with REDSOX observations. *J. Phys. Oceanogr.*, **38** (2), 337–358. 14, 58
- Chang, Y. S., X. Xu, T. M. Özgökmen, E. P. Chassignet, H. Peters, and P. F. Fischer, 2005: Comparison of gravity current mixing parameterizations and calibration using a high-resolution 3D nonhydrostatic spectral element model. *Ocean Modelling*, **10** (3-4), 342–368. 14, 17
- Chassignet, E., H. Hurlburt, O. Smedstad, G. Halliwell, P. Hogan, A. Wallcraft, and R. Bleck, 2006: Ocean prediction with the hybrid coordinate ocean model (HYCOM). *Ocean Weather Forecasting*, **5**, 413–426. 12
- Cummins, P. F., L. Armi, and S. Vagle, 2006: Upstream internal hydraulic jumps. *J. Phys. Oceanogr.*, **36** (5), 753–769. 95

- Danabasoglu, G., W. G. Large, and B. P. Briegleb, 2010: Climate impacts of parameterized Nordic Sea overflows. *J. Geophys. Res.*, **115** (C11). 119, 120
- Darelius, E., I. Fer, and D. Quadfasel, 2011: Faroe bank channel overflow: mesoscale variability \*. *J. Phys. Oceanogr.*, **41** (11), 2137–2154. 3
- Darelius, E., L. Smedsrød, S. Østerhus, A. Foldvik, and T. Gammelsrød, 2009: Structure and variability of the filchner overflow plume. *Tellus A*, **61** (3), 446–464. 5, 7, 8, 62
- Davey, F., 2004: *Ross Sea Bathymetry, 1:2,000,000, Version 1.0, Institute of Geological & Nuclear Sciences Geophysical Map 16*. Institute of Geological & Nuclear Sciences Limited, Lower Hutt, New Zealand. 72
- de Lavergne, C., J. B. Palter, E. D. Galbraith, R. Bernardello, and I. Marinov, 2014: Cessation of deep convection in the open southern ocean under anthropogenic climate change. *Nature Climate Change*, **4** (4), 278–282. 1
- Debreu, L., P. Marchesiello, P. Penven, and G. Cambon, 2012: Two-way nesting in split-explicit ocean models: Algorithms, implementation and validation. *Ocean Modelling*, **49-50**, 1–21. 12
- Dinniman, M. S., J. M. Klinck, and W. O. Smith, 2011: A model study of Circumpolar Deep Water on the West Antarctic Peninsula and Ross Sea continental shelves. *Deep Sea Res. Part II*, **58** (13-16), 1508–1523. 72
- Dong, C., J. C. McWilliams, and A. F. Shchepetkin, 2007: Island wakes in deep water. *J. Phys. Oceanogr.*, **37** (4), 962–981. 23
- Duan, J., F. P. F. T. Iliescu, and T. Özgökmen, 2010: Bridging the Boussinesq and primitive equations through spatio-temporal filtering. *Applied Math. Letters*, **23**, 453–456. 15
- Eldevik, T. and K. Dysthe, 2002: Spiral eddies. *J. Phys. Oceanogr.*, **32**, 851–869. 42
- Ellison, T. H. and J. S. Turner, 1959: Turbulent entrainment in stratified flows. *Journal of Fluid Mechanics*, **6** (03), 423–448. 83
- Ezer, T., 2005: Entrainment, diapycnal mixing and transport in three-dimensional bottom gravity current simulations using the mellor–yamada turbulence scheme. *Ocean Modelling*, **9** (2), 151–168. 97
- Ezer, T., 2006: Topographic influence on overflow dynamics: Idealized numerical simulations and the faroe bank channel overflow. *J. Geophys. Res.*, **111** (C2). 97
- Fischer, P., 1997: An overlapping Schwarz method for spectral element solution of the incompressible NavierStokes equations. *Journal of Computational Physics*, **133** (1), 84–101. 17

- Fischer, P., L. W. Ho, G. E. Karniadakis, E. M. Ronquist, and A. T. Patera, 1988: Recent advances in parallel spectral element simulation of unsteady incompressible flows. *Computer and Structures*, **30**, 217–231. 17
- Flierl, G. R., M. E. Stern, and J. A. Whitehead Jr, 1983: The physical significance of modons: Laboratory experiments and general integral constraints. *Dynamics of atmospheres and oceans*, **7 (4)**, 233–263. 92
- Foldvik, A., et al., 2004: Ice shelf water overflow and bottom water formation in the southern Weddell Sea. *J. Geophys. Res.*, **109 (C2)**, 1–15. xviii, 5, 7, 67, 76
- Foster, T. and E. Carmack, 1976: Frontal zone mixing and Antarctic Bottom Water formation in the southern Weddell Sea. *Deep Sea Research and Oceanographic . . .*, **23**. 5
- Fox-Kemper, B. and R. Ferrari, 2008: Parameterization of mixed layer eddies. Part II: prognosis and impact. *J. Phys. Oceanogr.*, **38 (6)**, 1166–1179. 13
- Fox-Kemper, B., R. Ferrari, and R. Hallberg, 2008: Parameterization of mixed layer eddies. Part I: theory and diagnosis. *J. Phys. Oceanogr.*, **38 (6)**, 1145–1165. 13, 15
- Fox-Kemper, B. and D. Menemenlis, 2008: Can large eddy simulation techniques improve mesoscale rich ocean models? *Geophysical Monograph Series*, 319–337. 12, 17
- Fringer, O., M. Gerritsen, and R. Street, 2006: An unstructured-grid, finite-volume, nonhydrostatic, parallel coastal ocean simulator. *Ocean Modelling*, **14 (3-4)**, 139–173. 39, 115
- Geyer, F., S. Osterhus, B. Hansen, and D. Quadfasel, 2006: Observations of highly regular oscillations in the overflow plume downstream of the Faroe Bank Channel. *J. Geophys. Res.*, **111 (C12)**, C12020. 3
- Gill, A., 1973: Circulation and bottom water production in the Weddell Sea. *Deep Sea Res.*, **20**, 111–140. 5, 8
- Girton, J. B. and T. B. Sanford, 2003: Descent and modification of the overflow plume in the Denmark strait\*. *J. Phys. Oceanogr.*, **33 (7)**, 1351–1364. xviii, 104
- Gordon, A., 2001: Bottom water formation. *Encyclopedia of Ocean Sciences*, 334–340. 5
- Gordon, A., E. Zambianchi, and A. Orsi, 2004: Energetic plumes over the western Ross Sea continental slope. *Geophysical Research . . .*, **31 (21)**. xviii, 7, 104
- Gordon, A. L., 1982: Weddell deep water variability. *J. Mar. Res.*, **40**, 199–217. 6

- Gordon, A. L., B. A. Huber, H. H. Hellmer, and A. Ffield, 1993: Deep and bottom water of the Weddell Sea's western rim. *Science*, **262** (5130), 95–97. 5
- Gordon, A. L., A. H. Orsi, R. Muench, B. a. Huber, E. Zambianchi, and M. Visbeck, 2009: Western Ross Sea continental slope gravity currents. *Deep Sea Research Part II: Topical Studies in Oceanography*, **56** (13-14), 796–817. 5, 6, 7, 63, 72
- Griffies, S., et al., 2000: Developments in ocean climate modelling. *Ocean Modelling*, **2** (3-4), 123–192. 12
- Griffies, S. M., 2004: *Fundamentals of ocean climate models*. Princeton University Press. 12, 88
- Haidvogel, D., et al., 2008: Ocean forecasting in terrain-following coordinates: Formulation and skill assessment of the Regional Ocean Modeling System. *Journal of Computational Physics*, **227** (7), 3595–3624. 19
- Haney, R. L., 1991: On the pressure gradient force over steep topography in sigma coordinate ocean models. *J. Phys. Oceanogr.*, **21** (4), 610–619. 63
- Hansen, B. and S. Osterhus, 2000: North Atlantic Nordic Seas exchanges. *Progress in Oceanography*, **45** (2), 109–208. 3
- Hansen, B. and S. Osterhus, 2007: Faroe Bank Channel overflow 1995–2005. *Progress in Oceanography*, **75** (4), 817–856. 3
- Heuzé, C., K. J. Heywood, D. P. Stevens, and J. K. Ridley, 2013: Southern Ocean bottom water characteristics in CMIP5 models. *Geophysical Research Letters*, **40** (7), 1409–1414. 2
- Heywood, K. J., R. A. Locarnini, R. D. Frew, P. F. Dennis, and B. A. King, 1998: Transport and water masses of the Antarctic Slope Front system in the eastern Weddell Sea. *Ocean, ice, and atmosphere: interactions at the Antarctic Continental Margin*, 203–214. 67
- Hodges, B. R., B. Laval, and B. M. Wadzuk, 2006: Numerical error assessment and a temporal horizon for internal waves in a hydrostatic model. *Ocean Modelling*, **13** (1), 44–64. 32
- Hoyer, J. L. and D. Quadfasel, 2001: Detection of deep overflows with satellite altimetry. *Geophysical Research Letters*, **28** (8), 1611–1614. 6
- Hurlburt, H. E., et al., 2008: Eddy-resolving global ocean prediction. *Ocean Modeling in Eddying Regime, AGU monograph*, 3523–382. 13
- Hurlburt, H. E., et al., 2009: High-resolution global and basin-scale ocean analyses and forecasts. *Oceanography*, **3**, 110–127. 13

- Ilicak, M., A. J. Adcroft, S. M. Griffies, and R. W. Hallberg, 2012: Spurious dianeutral mixing and the role of momentum closure. *Ocean Modelling*, **45-46**, 37–58. 20, 28, 30, 35, 39, 88
- Ilicak, M., S. Legg, A. Adcroft, and R. Hallberg, 2011: Dynamics of a dense gravity current flowing over a corrugation. *Ocean Modelling*, **38 (1-2)**, 71–84. 8, 67
- Ilicak, M., T. Özgökmen, H. Peters, H. Baumert, and M. Iskandarani, 2008: Performance of two-equation turbulence closures in three-dimensional simulations of the Red Sea overflow. *Ocean Modelling*, **24 (3-4)**, 122–139. 14, 27, 58, 63, 66
- Ilicak, M., T. M. Özgökmen, E. Özsoy, and P. F. Fischer, 2009: Non-hydrostatic modeling of exchange flows across complex geometries. *Ocean Modelling*, **29 (3)**, 159–175. 28, 58
- Ilcak, M., T. M. Özgökmen, and W. E. Johns, 2011: How does the Red Sea outflow water interact with Gulf of Aden Eddies? *Ocean Modelling*, **36 (1-2)**, 133–148. 4
- Inall, M. E., D. Aleynik, and C. Neil, 2013: Horizontal advection and dispersion in a stratified shelf sea: The role of inertial oscillations. *Progress in Oceanography*, **117**, 25–36. 47, 53
- Jacobs, S. S., 1991: On the nature and significance of the Antarctic Slope Front. *Marine Chemistry*, **35 (1)**, 9–24. 67
- Jacobs, S. S., A. F. Amos, and P. M. Bruchhausen, 1970: Ross Sea oceanography and Antarctic bottom water formation. *Deep Sea Research*, **17 (6)**, 935–962. 5
- Jensen, M. F., I. Fer, and E. Darelius, 2013: Low frequency variability on the continental slope of the southern Weddell Sea. *J. Geophys. Res.: Oceans*, **118 (July)**. xviii, 7, 8, 9, 10, 62, 76, 116
- Johnson, G. C., 2008: Quantifying Antarctic bottom water and north Atlantic deep water volumes. *J. Geophys. Res.*, **113 (C5)**, 1–13. 1
- Johnson, G. C. and S. C. Doney, 2006: Recent western south Atlantic bottom water warming. *Geophysical Research Letters*, **33 (14)**. 1
- Johnson, G. C., S. Mecking, B. M. Sloyan, and S. E. Wijffels, 2007: Recent bottom water warming in the Pacific Ocean\*. *Journal of Climate*, **20 (21)**, 5365–5375. 1
- Kanarska, Y., A. Shchepetkin, and J. McWilliams, 2007: Algorithm for non-hydrostatic dynamics in the regional oceanic modeling system. *Ocean Modelling*, **18 (3)**, 143–174. 115
- Kantha, L. H. and C. A. Clayson, 1994: An improved mixed layer model for geophysical applications. *J. Geophys. Res.*, **99**, 252355–25266. 14

- Kantha, L. H. and C. A. Clayson, 2000: *Numerical models of oceans and oceanic processes*, Vol. 66. Access Online via Elsevier. 15
- Kida, S., J. F. Price, and J. Yang, 2008: The upper-oceanic response to overflows: A mechanism for the azores current. *J. Phys. Oceanogr.*, **38** (4), 880–895. 6
- Kitade, Y., et al., 2014: Antarctic bottom water production from the Vincennes Bay polynya, east Antarctica. *Geophysical Research Letters*, **41** (10), 3528–3534. 6
- Klein, P. and G. Lapeyre, 2009: The oceanic vertical pump induced by mesoscale and submesoscale turbulence. *Annu. Rev. Mar. Sci.*, **1**, 351–375. 16
- Lane-Serff, G. and P. Baines, 1998: Eddy formation by dense flows on slopes in a rotating fluid. *J. Fluid Mech.*, **363**, 229–252. xiii, 9, 69, 73, 74, 75, 83
- Lane-Serff, G. F. and P. G. Baines, 2000: Eddy formation by overflows in stratified water. *J. Phys. Oceanogr.*, **30** (2), 327–337. 117
- Large, W., J. McWilliams, and S. Doney, 1994: Oceanic vertical mixing: a review and a model with a nonlocal boundary layer parameterization. *Reviews of Geophysics*, **32** (4), 363–403. 14, 26, 44
- Large, W. G., 1998: Modeling and parameterizing the ocean planetary boundary layer. *Ocean Modeling and Parameterization*, Springer, 81–120. 14, 17
- Lee, A. and D. Ellett, 1965: On the contribution of overflow water from the Norwegian Sea to the hydrographic structure of the North Atlantic Ocean. *Deep Sea Research and Oceanographic Abstracts*, **12** (2), 129–142. 3
- Legg, S., R. Hallberg, and J. Girton, 2006: Comparison of entrainment in overflows simulated by -coordinate, isopycnal and non-hydrostatic models. *Ocean Modelling*, **11** (1-2), 69–97. 67, 69, 83, 97
- Legg, S. and J. Klymak, 2008: Internal hydraulic jumps and overturning generated by tidal flow over a tall steep ridge. *J. Phys. Oceanogr.*, **38** (9), 1949–1964. 96
- Legg, S., et al., 2009: Improving oceanic overflow representation in climate models: the gravity current entrainment climate process team. *Bulletin of the American Meteorological Society*, **90** (5), 657–670. 2, 16, 83
- Lemarié, F., J. Kurian, A. F. Shchepetkin, M. Jeroen Molemaker, F. Colas, and J. C. McWilliams, 2012: Are there inescapable issues prohibiting the use of terrain-following coordinates in climate models? *Ocean Modelling*, **42**, 57–79. 12
- Lévy, M., P. Klein, and A.-M. Treguier, 2001: Impact of sub-mesoscale physics on production and subduction of phytoplankton in an oligotrophic regime. *Journal of Marine Research*, **59** (4), 535–565. 15

- Long, R. R., 1953: Some aspects of the flow of stratified fluids: I. a theoretical investigation. *Tellus*, **5** (1), 42–58. 96
- Long, R. R., 1954: Some aspects of the flow of stratified fluids: II. experiments with a two-fluid system. *Tellus*, **6** (2), 97–115. 96
- Lumpkin, R. and K. Speer, 2007: Global ocean meridional overturning. *J. Phys. Oceanogr.*, **37** (10), 2550–2562. 1
- MacCready, P., N. S. Banas, B. M. Hickey, E. P. Dever, and Y. Liu, 2009: A model study of tide- and wind-induced mixing in the Columbia River Estuary and plume. *Continental Shelf Research*, **29** (1), 278–291. 16
- Macrander, A., R. H. Käse, U. Send, H. Valdimarsson, and S. Jónsson, 2007: Spatial and temporal structure of the Denmark strait overflow revealed by acoustic observations. *Ocean Dynamics*, **57** (2), 75–89. 3
- Mahadevan, A. and A. Tandon, 2006: An analysis of mechanisms for submesoscale vertical motion at ocean fronts. *Ocean Modelling*, **14**, 241–256. 13
- Mahadevan, A., A. Tandon, and R. Ferrari, 2010: Rapid changes in mixed layer stratification driven by submesoscale instabilities and winds. *J. Geophys. Res.*, **115** (C3), 1–12. 55
- Marshall, J., A. Adcroft, C. Hill, L. Perelman, and C. Heisey, 1997a: A finite-volume, incompressible navier stokes model for studies of the ocean on parallel computers. *J. Geophys. Res.*, **102** (C3), 5753–5766. 85
- Marshall, J., C. Hill, L. Perelman, and A. Adcroft, 1997b: Hydrostatic, quasi-hydrostatic, and nonhydrostatic ocean modeling. *J. Geophys. Res.*, **102** (C3), 5733–5752. 85
- Marshall, J., H. Jones, and C. Hill, 1998: Efficient ocean modeling using nonhydrostatic algorithms. *Journal of Marine Systems*, **18** (1), 115–134. 115
- Martin, P., J. Book, D. Burrage, C. Rowley, and M. Tudor, 2009: Comparison of model-simulated and observed currents in the central Adriatic during DART. *J. Geophys. Res.*, **114**. 12
- Matsumura, Y. and H. Hasumi, 2010: Modeling ice shelf water overflow and bottom water formation in the southern Weddell Sea. *J. Geophys. Res.*, **115** (C10), 1–17. 7
- Matt, S. and W. E. Johns, 2007: Transport and entrainment in the Red Sea outflow plume. *J. Phys. Oceanogr.*, **37** (4), 819–836. xviii, 4, 104

- Mauritzen, C., J. Price, T. Sanford, and D. Torres, 2005: Circulation and mixing in the Faroese channels. *Deep Sea Research Part I: Oceanographic Research Papers*, **52 (6)**, 883–913. 3
- McWilliams, J., 1985a: A uniformly valid model spanning the regimes of geostrophic and isotropic, stratified turbulence: balanced turbulence. *Journal of the Atmospheric Sciences*, **42 (16)**, 1773–1774. 39
- McWilliams, J. C., 1985b: Submesoscale, coherent vortices in the ocean. *Rev. Geophys.*, **23 (2)**, 165–182. 15
- McWilliams, J. C., 2008: Fluid dynamics at the margin of rotational control. *Environmental Fluid Mechanics*, **8 (5-6)**, 441–449. 15, 16
- Mellor, G. L. and T. Yamada, 1982: Development of a turbulence closure model for geophysical fluid problems. *Rev. Geophys.*, **30**, 851–875. 14
- Middleton, J. H., T. D. Foster, and A. Foldvik, 1987: Diurnal shelf waves in the southern weddell sea. *J. Phys. Oceanogr.*, **17 (6)**, 784–791. 117
- Muench, R., L. Padman, A. Gordon, and A. Orsi, 2009a: A dense water outflow from the Ross Sea, Antarctica: Mixing and the contribution of tides. *J. Mar. Sys.*, **77 (4)**, 369–387. xviii, 7, 8, 67, 76, 104
- Muench, R. D., a. K. Wå hlin, T. M. Özgökmen, R. Hallberg, and L. Padman, 2009b: Impacts of bottom corrugations on a dense Antarctic outflow: NW Ross Sea. *Geophysical Research Letters*, **36 (23)**, 1–6. 7, 8
- Müller, P., J. McWilliams, and M. Molemaker, 2005: Routes to dissipation in the ocean: the two-dimensional/three-dimensional turbulence conundrum. *Marine Turbulence: Theories, Observations, and Models. Results of the CARTUM project*, ed. H. Z. Baumert, J. Simpson and J. Sündermann. *Cambridge University Press*, 397–405. 16
- Murray, S. and W. Johns, 1997: Direct observations of seasonal exchange through the Bab el Mandab Strait. *Geophysical Research Letters*, **24 (21)**, 2557–2560. 4
- Noormets, R., J. Dowdeswell, R. D. Larter, C. Ó. Cofaigh, and J. Evans, 2009: Morphology of the upper continental slope in the Bellingshausen and Amundsen Seas—Implications for sedimentary processes at the shelf edge of West Antarctica. *Marine Geology*, **258 (1)**, 100–114. 8
- Ohshima, K. I., et al., 2013: Antarctic bottom water production by intense sea-ice formation in the Cape Darnley polynya. *Nature Geoscience*, **6 (3)**, 235–240. 6
- Olsen, S. M., B. Hansen, D. Quadfasel, and S. Osterhus, 2008: Observed and modelled stability of overflow across the Greenland-Scotland ridge. *Nature*, **455 (7212)**, 519–22. 3

- Orsi, A., 1999: Circulation, mixing, and production of Antarctic Bottom Water. *Progr. in Oceanogr.*, **43** (1), 55–109. 2, 5
- Orsi, A. H., S. S. Jacobs, A. L. Gordon, and M. Visbeck, 2001: Cooling and ventilating the abyssal ocean. *Geophysical Research Letters*, **28** (15), 2923. 3
- Orsi, A. H. and C. L. Wiederwohl, 2009: A recount of Ross Sea waters. *Deep Sea Research Part II: Topical Studies in Oceanography*, **56** (13-14), 778–795. 6
- Özgökmen, T. and P. Fischer, 2012: CFD application to oceanic mixed layer sampling with Lagrangian platforms. *Int. J. Comp. Fluid. Dyn.*, **26** (6-8), 337–348. 16, 17
- Özgökmen, T., T. Iliescu, and P. Fischer, 2009a: Large eddy simulation of stratified mixing in a three-dimensional lock-exchange system. *Ocean Modelling*, **26**, 134–155. 16, 17, 18, 28
- Özgökmen, T., T. Iliescu, and P. Fischer, 2009b: Reynolds number dependence of mixing in a lock-exchange system from direct numerical and large eddy simulations. *Ocean Modelling*, **30**, 190–206. xi, 16, 17, 18, 21, 22, 23, 28, 49
- Özgökmen, T., A. Poje, P. Fischer, H. Childs, H. Krishnan, C. Garth, A. Haza, and E. Ryan, 2012: On multi-scale dispersion under the influence of surface mixed layer instabilities and deep flows. *Ocean Modelling*, **56**, 16–30. 16, 17
- Özgökmen, T., A. Poje, P. Fischer, and A. Haza, 2011: Large eddy simulations of mixed layer instabilities and sampling strategies. *Ocean Modelling*, **39**, 311–331. xi, 16, 17, 40, 41, 42, 47, 51, 60
- Özgökmen, T. M. and E. P. Chassignet, 2002: Dynamics of two-dimensional turbulent bottom gravity currents. *J. Phys. Oceanogr.*, **32** (5), 1460–1478. 84, 87, 93, 120
- Özgökmen, T. M., E. P. Chassignet, and C. G. Rooth, 2001: On the connection between the mediterranean outflow and the azores current. *J. Phys. Oceanogr.*, **31** (2), 461–480. 6
- Özgökmen, T. M. and P. F. Fischer, 2008: On the role of bottom roughness in overflows. *Ocean Modelling*, **20** (4), 336–361. 8, 84
- Özgökmen, T. M., P. F. Fischer, J. Duan, and T. Iliescu, 2004: Three-dimensional turbulent bottom density currents from a high-order nonhydrostatic spectral element model. *J. Phys. Oceanogr.*, **34** (9), 2006–2026. 84
- Özgökmen, T. M., P. F. Fischer, and W. E. Johns, 2006: Product water mass formation by turbulent density currents from a high-order nonhydrostatic spectral element model. *Ocean Modelling*, **12** (3), 237–267. xvi, 84, 107, 108

- Özgökmen, T. M., T. Iliescu, P. Fischer, A. Srinivasan, and J. Duan, 2007: Large eddy simulation of stratified mixing in two-dimensional dam-break problem in a rectangular enclosed domain. *Ocean Modelling*, **16** (1-2), 106–140. 17, 28
- Özgökmen, T. M., W. Johns, H. Peters, and S. Matt, 2003: Turbulent mixing in the Red Sea outflow plume from a high-resolution nonhydrostatic model. *J. Phys. Oceanogr.*, **33**, 1846–1869. 58
- Padman, L., S. L. Howard, A. H. Orsi, and R. D. Muench, 2009: Tides of the north-western Ross Sea and their impact on dense outflows of Antarctic Bottom Water. *Deep Sea Res., Part I*, **56** (13-14), 818–834. xviii, 7, 8, 63, 67, 76, 117
- Patera, A., 1984: A spectral element method for fluid dynamics: laminar flow in a channel expansion. *Journal of Computational Physics*, **54** (3), 468–488. 17
- Peters, H., M. Gregg, and J. Toole, 1988: On the parameterization of equatorial turbulence. *J. Geophys. Res.: Oceans (1978–2012)*, **93** (C2), 1199–1218. 44
- Peters, H., W. E. Johns, A. S. Bower, and D. M. Fratantoni, 2005: Mixing and entrainment in the Red Sea outflow plume. Part I: Plume structure. *J. Phys. Oceanogr.*, **35** (5), 569–583. xviii, 4, 83, 104
- Piggott, M., G. Gorman, C. Pain, P. Allison, A. Candy, B. Martin, and M. Wells, 2008: A new computational framework for multi-scale ocean modelling based on adapting unstructured meshes. *International Journal for Numerical Methods in Fluids*, **56** (8), 1003–1015. 115
- Platzman, G., G. Curtis, K. S. Hansen, and R. D. Slater, 1981: Normal modes of the world ocean. Part II: description of modes in the period range 8 to 80 hours. *J. Phys. Oceanogr.*, **11**, 579–603. 8
- Plumb, R. A. and R. Ferrari, 2005: Transformed Eulerian-mean theory. Part I: non-quasigeostrophic theory for eddies on a zonal-mean flow. *J. Phys. Oceanogr.*, **35** (2). 55
- Prather, M. J., 1986: Numerical advection by conservation of second-order moments. *J. Geophys. Res.: Atmospheres (1984–2012)*, **91** (D6), 6671–6681. 35
- Price, J. and M. Baringer, 1994: Outflows and deep water production by marginal seas. *Progr. in Oceanogr.*, **33**, 161–200. 2, 4, 7, 73, 83, 87
- Price, J. F. and J. Yang, 1998: Marginal sea overflows for climate simulations. *Ocean Modeling and Parameterization*, Springer, 155–170. 119, 120
- Price, J. F., et al., 1993: Mediterranean outflow mixing and dynamics. *Science*, **259** (5099), 1277–1282. xviii, 104

- Purkey, S. G. and G. C. Johnson, 2010: Warming of global abyssal and deep southern ocean waters between the 1990s and 2000s: contributions to global heat and sea level rise budgets\*. *Journal of Climate*, **23** (23), 6336–6351. 1
- Ramachandran, S., A. Tandon, and A. Mahadevan, 2013: Effect of subgrid-scale mixing on the evolution of forced submesoscale instabilities. *Ocean Modelling*, **66**, 45–63. 13, 17, 55, 56
- Rintoul, S., 1998: On the origin and influence of Adelie Land Bottom Water. *Ocean, Ice, and Atmosphere: Interactions at the Antarctic Continental Margin*, **75**, 151–171. 5
- Sagaut, P., 2000: *Large eddy simulations for incompressible flows*, Vol. 3. Springer Berlin. 16
- San, O., A. Staples, Z. Wang, and T. Iliescu, 2011: Approximate deconvolution large eddy simulation of a barotropic ocean circulation model. *Ocean Modelling*, **40** (2), 120–132. 15
- Saunders, P., 1996: The ux of dense cold overow water southeast of Iceland. *J. Phys. Oceanogr.*, **26**, 85–95. 3
- Schmitz, W., 1995: On the interbasis-scale thermohaline circulation. *Reviews of Geophysics*, **33** (2), 151–173. 1
- Scotti, a. and S. Mitrani, 2008: An approximated method for the solution of elliptic problems in thin domains: Application to nonlinear internal waves. *Ocean Modelling*, **25** (3-4), 144–153. 15, 31
- Shchepetkin, A. F. and J. C. McWilliams, 1998: Quasi-monotone advection schemes based on explicit locally adaptive dissipation. *Monthly Weather Review*, **126** (6), 1541–1580. 13, 20, 30, 64, 65
- Shchepetkin, A. F. and J. C. McWilliams, 2005: The regional oceanic modeling system (ROMS): a split-explicit, free-surface, topography-following-coordinate oceanic model. *Ocean Modelling*, **9** (4), 347–404. 19, 63
- Sherwin, T. J. and W. R. Turrell, 2005: Mixing and advection of a cold water cascade over the Wyvill Thomson Ridge. *Deep Sea Research Part I: Oceanographic Research Papers*, **52** (8), 1392–1413. 3
- Simpson, J. E., 1999: *Gravity currents: In the environment and the laboratory*. Cambridge University Press. 83, 85, 92
- Smith, P. C., 1975: A streamtube model for bottom boundary currents in the ocean. *Deep Sea Research*, **22** (12), 853–873. 119, 120

- Smith, R. A., 1991: Maximization of vortex entropy as an organizing principle in intermittent, decaying, two-dimensional turbulence. *Physical Review A*, **43** (2), 1126–1129. 92
- Song, Y. and D. B. Haidvogel, 1994: A semi-implicit ocean circulation model using a generalized topography-following coordinate system. *Journal of Computational Physics*, **115** (1), 228–244. 19
- Spall, M. A. and J. F. Price, 1998: Mesoscale variability in denmark strait: The pv outflow hypothesis\*. *J. Phys. Oceanogr.*, **28** (8), 1598–1623. 3, 73
- Sundermeyer, M. and J. Ledwell, 2001: Lateral dispersion over the continental shelf: Analysis of dye release experiments. *J. Geophys. Res.*, **106**, 9603–9621. 47, 53
- Tandon, A. and C. Garrett, 1994: Mixed layer restratification due to horizontal density gradients. *J. Phys. Oceanogr.*, **24**, 1419–1424. 47
- Taylor, J. R. and R. Ferrari, 2009: On the equilibration of a symmetrically unstable front via a secondary shear instability. *Journal of Fluid Mechanics*, **622**, 103–113. 15
- Taylor, K. E., R. J. Stouffer, and G. A. Meehl, 2012: An overview of cmip5 and the experiment design. *Bulletin of the American Meteorological Society*, **93** (4), 485–498. 2
- Thomas, L., A. Tandon, and A. Mahadevan, 2008: Submesoscale processes and dynamics. *Ocean Modeling in an Eddying Regime*, edited by M. Hecht and H. Hasume, **Geophysical Monograph** **177**, 17–38. 13
- Thoppil, P., J. Richman, and P. Hogan, 2011: Energetics of a global ocean circulation model compared to observations. *Geophys. Res. Lett.*, **38** (38). 13
- Tseng, Y.-h. and J. H. Ferziger, 2001: Mixing and available potential energy in stratified flows. *Physics of Fluids*, **13** (5), 1281. 28
- Turner, J., 1986: Turbulent entrainment: the development of the entrainment assumption, and its application to geophysical flows. *Journal of Fluid Mechanics*, **173**, 431–471. 120
- Umlauf, L. and H. Burchard, 2005: Second-order turbulence closure models for geophysical boundary layers. a review of recent work. *Cont. Shelf Res.*, **25**, 795–827. 14
- Vallis, G. K., 2006: *Atmospheric and oceanic fluid dynamics: fundamentals and large-scale circulation*. Cambridge University Press. 39, 50

- Visbeck, M. and A. M. Thurnherr, 2009: High-resolution velocity and hydrographic observations of the Drygalski Trough gravity plume. *Deep Sea Research Part II: Topical Studies in Oceanography*, **56** (13-14), 835–842. 7
- Voet, G. and D. Quadfasel, 2010: Entrainment in the Denmark strait overflow plume by meso-scale eddies. *Ocean Science*, **6** (1), 301–310. 3
- Wahlén, A., 2002: Topographic steering of dense currents with application to submarine canyons. *Deep Sea Research Part I: Oceanographic Research Papers*, **49** (2), 305–320. 8
- Wahlén, A., 2004: Downward channeling of dense water in topographic corrugations. *Deep Sea Research Part I: Oceanographic Research Papers*, **51** (4), 577–590. 8
- Wahlén, A., E. Darelius, C. Cenedese, and G. F. Lane-Serff, 2008: Laboratory observations of enhanced entrainment in dense overflows in the presence of submarine canyons and ridges. *Deep-Sea Research*, **55**, 737–750. 8
- Wang, D., J. C. McWilliams, and W. G. Large, 1998: Large-eddy simulation of the diurnal cycle of deep equatorial turbulence. *J. Phys. Oceanogr.*, **28** (1), 129–148. 17
- Wang, Q., S. Danilov, H. H. Hellmer, and J. Schröter, 2010: Overflow dynamics and bottom water formation in the western Ross Sea: Influence of tides. *J. Geophys. Res.*, **115** (C10), 1–16. 7, 8
- Wang, Q., S. Danilov, and J. Schröter, 2009: Bottom water formation in the southern Weddell Sea and the influence of submarine ridges: Idealized numerical simulations. *Ocean Modelling*, **28** (1-3), 50–59. xviii, 7, 8, 62, 76
- Warner, J. C., W. R. Geyer, and J. A. Lerczak, 2005a: Numerical modeling of an estuary: A comprehensive skill assessment. *J. Geophys. Res.*, **110**. 16
- Warner, J. C., C. R. Sherwood, H. G. Arango, and R. P. Signell, 2005b: Performance of four turbulence closure methods implemented using a generic length scale method. *Ocean Modelling*, **8**, 81–113. 14, 27
- Whitworth, T. and A. H. Orsi, 2006: Antarctic Bottom Water production and export by tides in the Ross Sea. *Geophysical Research Letters*, **33** (12). 5, 8
- Wilchinsky, A. V. and D. L. Feltham, 2009: Numerical simulation of the Filchner overflow. *J. Geophys. Res.*, **114** (C12), 1–20. 7
- Wilcox, D. C. et al., 1998: *Turbulence modeling for CFD*, Vol. 2. DCW industries La Canada, CA. 14

- Williams, G. D., S. Aoki, S. S. Jacobs, S. R. Rintoul, T. Tamura, and N. L. Bindoff, 2010: Antarctic Bottom Water from the Adélie and George V Land coast, East Antarctica (140149E). *J. Geophys. Res.*, **115** (C4), C04027. 5
- Winters, K. B., P. N. Lombard, J. J. Riley, and E. A. D'Asaro, 1995: Available potential energy and mixing in density-stratified fluids. *Journal of Fluid Mechanics*, **289**, 115. 28, 59
- Winton, M., R. Hallberg, and A. Gnanadesikan, 1998: Simulation of density-driven frictional downslope flow in z-coordinate ocean models. *J. Phys. Oceanogr.*, **28** (11), 2163–2174. 88
- Wong, A. P. and S. C. Riser, 2013: Modified shelf water on the continental slope north of Mac Robertson Land, East Antarctica. *Geophysical Research Letters*, **40** (23), 6186–6190. 6
- Xu, X., Y. Chang, H. Peters, T. Özgökmen, and E. Chassignet, 2006: Parameterization of gravity current entrainment for ocean circulation models using a high-order 3D nonhydrostatic spectral element model. *Ocean Modelling*, **14** (1-2), 19–44. 17, 58, 120